RICE UNIVERSITY

Multidomain Peptides: Sequence-Nanostructure Relationships and Biological Applications

By

Erica Laraine Bakota

A THESIS SUBMITTED IN PARTIAL FULFILLMENT OF THE REQUIREMENTS FOR THE DEGREE

Doctor of Philosophy

APPROVED, THESIS COMMITTEE:

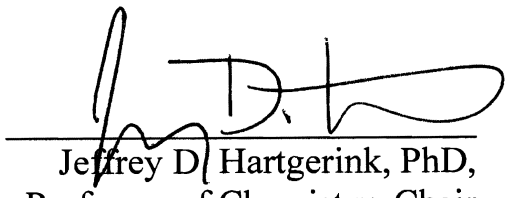

Jeffrey D. Hartgerink, PhD,
Associate Professor of Chemistry, Chair

Lon J. Wilson, PhD,
Professor of Chemistry

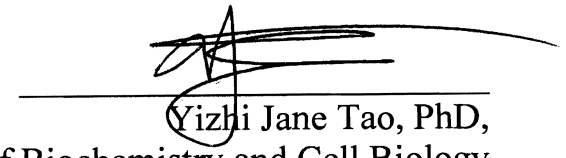

Yizhi Jane Tao, PhD,
Associate Professor of Biochemistry and Cell Biology

Houston, TX
March 2011

Abstract

Peptides are materials that, as a result of their polymeric nature, possess enormous versatility and customizability. Multidomain peptides are a class of peptides that self-assemble to form stable, cytocompatible hydrogels. They have an ABA block motif, in which the A block is composed of charged amino acids, such as lysine, and the B block consists of alternating hydrophilic and hydrophobic amino acids, such as glutamine and leucine. The B block forms a facial amphiphile that drives self-assembly. The charged A blocks simultaneously limit self-assembly and improve solubility. Self-assembly is triggered by charge screening of these charged amino acids, enabling the formation of β-sheet fibers. The development of an extended nanofiber network can result in the formation of a hydrogel.

Systematic modifications to both the A and B blocks were investigated, and it was found that sequence modifications have a large impact on peptide nanostructure and hydrogel rheology. The first modification examined is the substitution of amino acids within the hydrophilic positions of the B block. The second set of modifications investigated was the incorporation of aromatic amino acids in the B block. Finally, the charged block was varied to generate different net charges on the peptides, a change which impacted the ability to use these peptides in cell culture.

Two applications of multidomain peptide nanofibers are explored, the first of which is the delivery of novel therapies *in vivo*. One multidomain peptide is able to form hydrogels that undergo shear-thinning and rapid recovery. This gel can be loaded with cytokines and growth factors that have been secreted by embryonic stem cells, and these molecules can be subsequently released in a therapeutic setting. Another application for

multidomain peptide is their use as biocompatible surfactants. Single-walled carbon nanotubes have been widely investigated for their unique optical and electrical properties, but their solubility in aqueous systems has been a challenge. Multidomain peptides solubilize carbon nanotubes, are less cytotoxic than detergents such as SDBS, and preserve the ability of carbon nanotubes to fluoresce. Some of these peptides are also compatible with cell culture, allowing the delivery of single-walled carbon nanotubes to cells.

Acknowledgements

First and foremost, I would like to thank my advisor Dr. Jeffrey Hartgerink for his guidance over the last several years. Thank you, Jeff, for allowing me the space to learn to think independently. Thank you for your patience while I learned from my mistakes. And thank you for the lessons you've taught me, especially the ones where I didn't even know at the time that you were teaching me.

I extend my warmest thanks to my committee members, Dr. Lon Wilson and Dr. Yizhi Jane Tao. Thank you for your expertise and constructive criticism.

Thank you to the members of the Hartgerink Lab. It meant so much to me to be able to share every laugh, cry, and frustration with you over the last few years, and without you, this journey wouldn't have been nearly as much fun. Thank you for the thoughtful discussions and great companionship.

I would also like to thank my parents, Gary and Adrienne Flor, who stood behind me every step of the way. And last but not least, I am grateful to my husband Eric, who gave me sanity in times when it was nowhere to be found.

Table of Contents

List of Abbreviations

Abbreviation	Description
AFM	atomic force microscopy
BUN	blood urea nitrogen
CD	circular dichroism
DCM	dichloromethane
DiEA	diisopropylethylamine
DMF	dimethylformamide
EDT	ethanedithiol
FMOC	9-fluorenylmethoxycarbonyl
FT-IR	Fourier transform infrared spectroscopy
HBTU	2-(1H-benzotriazol-1-yl)-1,1,3,3-tetramethyluronium hexafluorophosphate
HOBt	N-Hydroxybenzotriazole
HPLC	high pressure liquid chromatography
IR	infrared spectroscopy
LO	lysyl oxidase
LPS	lipopolysaccharide
MBHA	methylbenzhydrylamine
PAO	plasma amine oxidase
SEM	scanning electron microscopy
TEM	transmission electron microscopy
TFA	trifluoroacetic acid
UV-VIS	ultraviolet-visible spectroscopy

Abbreviation	Description
A	alanine
C	cysteine
D	aspartic acid
E	glutamic acid
F	phenylalanine
G	glycine
H	histidine
I	isoleucine
K	lysine
L	leucine
M	methionine
N	asparagine
O	hydroxyproline
P	proline
Q	glutamine
R	arginine
S	serine
T	threonine
V	valine
W	tryptophan
Y	tyrosine

List of Figures

List of Tables

Chapter 1: Introduction

A. Supramolecular Chemistry: Thinking Beyond the Molecule

One of the most rapidly evolving and intriguing areas of chemistry today is the field of supramolecular chemistry. Inspired by the complex yet highly functional structures found naturally in biology, supramolecular chemistry builds on traditional synthetic chemistry in that it can orchestrate individual molecules into large, organized structures via the process of self-assembly. Self-assembly relies on numerous non-covalent interactions originating from the chemistry of the constituent molecules and takes place in the absence of external forces. Because the chemistry of the component molecules alone drives self-assembly, self-assembly processes are subject to equilibrium and thus the reactions taking place are often reversible. This offers a useful feature to self-assembling systems: the possibility of error correction. If one subunit of a larger structure is incorporated in an incorrect or energetically unfavorable manner, this subunit may be replaced in favor of lower energy interactions. In contrast, in a system that forms covalent bonds, the activation energy to correct errors is prohibitively high. This trial-and-error process for supramolecular assemblies allows the construction of extremely complicated structures. This also allows the accurate construction of hierarchical self-assembled materials from the "bottom up." In fact, this "bottom up" approach is at work in most systems found in nature. This brief survey of self-assembling systems will examine some of these systems found in nature, such as DNA and amyloid-β structures. It will then illustrate how we might take advantage of the principles employed in these natural systems to synthesize increasingly complex nanostructures.

A variety of synthetic systems have been constructed using the principles of self-assembly. One well-known type of supramolecular system is the host-guest system[1]. Simple host-guest complexes range from podands and corands and their ligands to the more complex spherands and calixarenes (Figure 1.1). These systems utilize noncovalent interactions to keep the guest molecule in place. Other host-guest complexes, such as carcerands,[1] sterically block the movement of the guest atom or molecule.

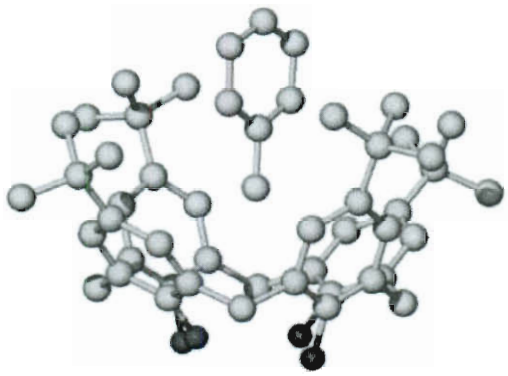

Figure 1.1. X-ray crystal structure of a typical calixarene, p-tert-butylcalix[4]arene-toluene. Adapted from Figure 1.23 in reference 1. The host-guest relationship is easily observed between the two molecules.

In addition to host-guest chemistry, other self-assembling molecules have been investigated, including porphyrins,[2] block copolymers,[3] quantum dots,[4] and metallic nanorods.[5] Vast arrays of even larger nanostructures have been prepared. These range from nanotubes[6, 7] to nanoribbons[8] and nanofibers.[9] Synthetic techniques have even allowed us to construct molecules that mimic biological systems. An array of bio-inspired and biomimetic materials will be discussed here, including collagen-mimetic peptides, alpha helical peptide materials, and beta sheet peptide hydrogels. Chapter 2 details the initial synthesis and characterization of a class of peptides called multidomain peptides, which form beta sheet nanofibers in aqueous solution. Chapter 3 explores the covalent modification of these peptides through the use of enzymes. Two chapters are devoted to

the biological applications of this robust self-assembling system: Chapter 4 shows that multidomain peptides can act as surfactants for carbon nanotubes, allowing carbon nanotube to be safely delivered in a biological setting. Chapter 5 investigates the use of multidomain peptide hydrogels as drug delivery agents both in a cell culture setting as well as in laboratory animals.

B. Self-Assembly of Biological Molecules

Nearly every type of biological molecule utilizes supramolecular chemistry to construct functional structures. Nucleic acid chemistry is one example of such self-assembly at work. Individual strands of DNA interact with each other via hydrogen bonds and π-stacking interactions to form a double helix. Double helices can then fold, in the presence of histones,[10] into organized chromatin structures,[11] and they also interact with enzymes in predictable ways.[12] Nature has even taken advantage of error correction in DNA, a feature that is facilitated by DNA polymerase enzymes. RNA also possesses the ability to self-assemble into molecules called ribozymes,[13] which are capable of catalyzing chemical reactions. Lipids can self-assemble into highly functional structures as well, the most well-known of which is the lipid bilayer found in every cell. Outside the body, lipids and their derivatives can also assemble into other structures such as monolayers[14] and liposomes.[15] But supramolecular chemistry is not limited to just lipids and nucleic acids. Perhaps there is no better showcase of self-assembly than the vast array of functional molecules made from peptides and proteins.

Peptides and proteins are linear polymers constructed from amino acids. The wide variety of amino acids available, both natural and synthetic, provide a nearly infinite number of sequence possibilities. Individual amino acid residues can have drastic effects on the peptide secondary structure, leading in turn to a variety of higher order structures. The interactions taking place between amino acids when these structures are formed may be between peptide backbone atoms or between side chains, between amino acids that are close in sequence or very distant, or even between amino acids in different proteins. Once the secondary and tertiary structures of individual proteins are established, distinct peptides and proteins can self-assemble into functional units. Virus capsids are one such unit, whose function is to encase and protect the viral genetic material. The human immunodeficiency virus (HIV) capsid is composed of 2,000 copies of the protein p24, self-assembled into a cone. Adenoviruses, a family of respiratory viruses, have an icosahedral capsid composed of 20 identical triangular faces, each consisting of dozens of protein molecules.[16,17] Two representations of this viral capsid are shown in Figure 1.2. Enzymes are another functional unit made from peptide and/or protein building blocks. That these molecules can catalyze nearly any chemical transformation required for life is a testament to the incredible flexibility of self-assembly.

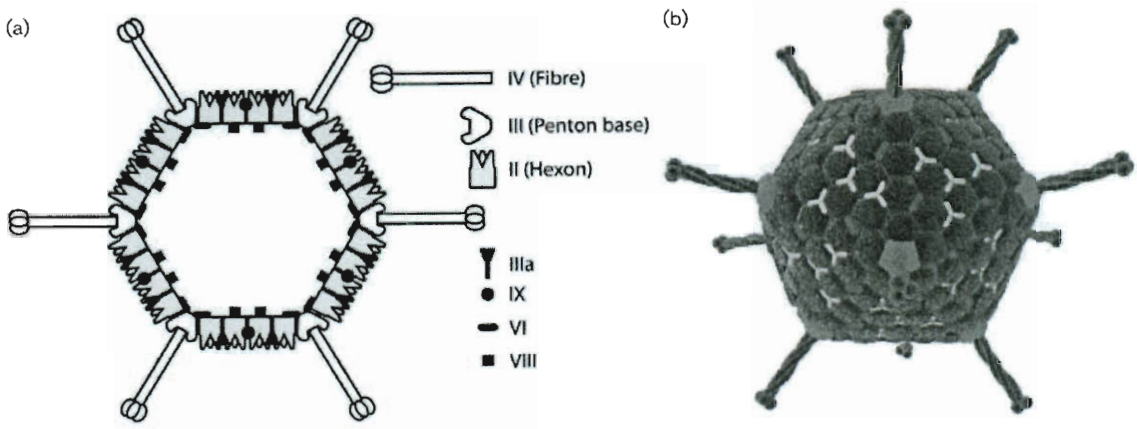

Figure 1.2. a) Diagram of the assembled adenovirus icosahedral capsid. b) Three-dimensional representation of the viral particle, showing the positions of each of the capsid proteins. The hexon, penton base and fibre proteins are shown in dark blue, light blue and green, respectively. The two minor capsid proteins are superimposed. Protein IX is shown in yellow, and protein IIIa is shown in red. Adapted from reference 17.

C. Peptide Self-Assembly

In recent years, chemists have begun to harness the potential for novel self-assembly that peptides and proteins have to offer. Amino acid side chains drive much of the chemistry of peptides and proteins. These side chains vary widely in functionality: they may be charged, hydrophobic, hydrophilic, aromatic, or a combination of these attributes. Charged amino acids can participate in ion-ion or ion-dipole interaction as well as hydrogen bonding. Hydrophobic amino acids have the capability of aggregating in order to reduce the hydrophobic surface area in contact with water. This creates a hydrophobic domain that can be a driving factor in peptide self-assembly. Hydrophilic amino acids may interact with water and may also participate in hydrogen bonding. Finally, aromatic amino acids have the capability to participate in π-π stacking with one another. π-π stacking can be a powerful force for self-assembly and contributes to the assembly of such systems as amyloid-β and the DNA double helix. All of these interactions play a

role in native protein folding, and most are utilized in complex synthetic self-assembled systems. Managing these interactions allows a level of control over peptide secondary structure. Given the variety of functionalities available in amino acid side chains, it is not surprising that we can selectively take advantage of specific interactions between amino acid side chains to create a vast array of nanostructures. A variety of synthetic peptides have been prepared, leading to nanostructures such as peptide nanotubes,[6] collagen-like triple helices,[18, 19] alpha-helical coiled coils,[20] and beta-sheet nanofibers.[21]

1. Cyclic Peptide Nanotubes

Peptide nanotubes can be constructed from the packing of cyclic peptides, small peptides with alternating D- and L-amino acids. This unique type of peptide architecture was inspired by the antibiotic gramicidin A.[22, 23] The alternating D- and L-residues allow all of the side chains to face away from the center of the tube when the molecule is cyclized. Homochiral peptides (all D- or all L-amino acids) do not cyclize due to unfavorable steric interactions between the amino acids that would reside on the interior of the ring. The heterochiral cyclic peptides stack on top of one another to form a hollow tube, driven by the formation of anti-parallel hydrogen bonds between adjacent peptides (Figure 1.3).[6] Extensive stacking leads to the formation of nanotubular structures. Later work by the Ghadiri group showed that the pore size of these tubular structures could be varied.[24] These nanotubes can function as ion channels when inserted into lipid bilayer membranes.[25] Outside of a biological environment, multiple peptide nanotubes can also interact with one another, forming organized microcrystals in another tier of self-

assembly. These types of peptides and their supramolecular structures have been shown to have promising antimicrobial activity.[26-28]

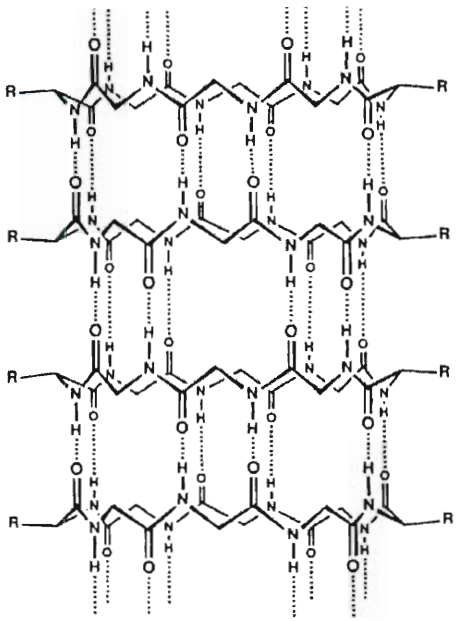

Figure 1.3. Peptides have the capability to self-assemble to form hollow nanotubes held together by hydrogen bonds. Adapted from reference 6.

2. Triple Helices: Collagen and Related Structures

Collagen is an excellent example of a peptide with hierarchical self-assembly. Collagen is the most abundant protein found in the body and a major component of the extracellular matrix. Its secondary structure is a signature polypeptide triple helix, characterized by the repeating sequence X-Y-Gly. Ramachandran was the first to postulate the triple helical structure,[29, 30] a model that was revised by Rich and Crick[31] and later validated by the Brodsky group.[32] In this model, the X position is commonly occupied by proline and the Y position is most frequently occupied by hydroxyproline (abbreviated O), a post-translationally modified amino acid derived from proline.

Hydroxyproline provides a stabilizing effect to the triple helix over proline alone. The mechanism of this stabilization has been widely investigated. Based on work by the Brodsky group, it has been suggested that hydroxyproline participates in extensive hydrogen bonding with water, which stabilizes the helix.[32] The Raines group has suggested that this stabilization arises from stereoelectronic effects: the addition of a hydroxyl moiety to the proline residue imparts an electron-withdrawing effect that drives the conformation of the amino acid backbone into a *trans* rather than a *cis* conformation.[33] Because all residues in the folded triple helix must be *trans*, the addition of electron-withdrawing groups leads to peptide conformations that favor self-assembly. Proline and hydroxyproline are responsible for the twisting helical structure of the polypeptide as a result of their preferred dihedral angles. The third amino acid in the recurring triplet is glycine. The lack of side chain functional groups allow glycine residues to pack closely together at the core of the triple helix, an interaction that would be greatly disrupted by any amino acid substitution in this position of the peptide sequence. The steric interference provided by the amino acid side chain would prevent the close contact necessary to maintain a stable helical structure. Once the triple helix is formed from three individual peptide strands, multiple helices self-assemble into collagen fibrils and these, in turn, assemble into fibers. This organized self-assembly on multiple levels makes collagen-mimetic peptides a fascinating area of research.

Synthetic collagen-like peptides can be prepared as homotrimers, in which all three peptide in the helix are identical, or as heterotrimers, in which there are two or three unique peptides in the triple helix. Heterotrimers are termed AAB if there are two unique types of peptides in the helix and ABC if there are three distinct peptides. When the

collagen X-Y-Gly template is entirely filled with proline, hydroxyproline, and glycine, respectively, the resulting peptide monomers self-assemble into homotrimeric triple helices.[32] While these homotrimers are themselves useful in studying self-assembly, natural collagen is not homotrimeric, but rather heterotrimeric. The preparation of heterotrimeric triple helices has been more challenging. The Hartgerink group has prepared and characterized several heterotrimeric collagen-mimetic peptides, including the ABC-type heterotrimer composed of three peptides: $(PKG)_{10}$, $(DOG)_{10}$, and $(POG)_{10}$.[18, 19] This peptide self-assembles into triple helices (Figure 1.4) that are stable up to 65°C, well above physiological temperature. A second heterotrimer, an AAB-type, can be prepared from a 2:1 mixture of $(EOGPOG)_5$ and $(PRG)_{10}$ and is stable up to 56°C.[34] The assembly of these systems is driven by electrostatics, although other interactions in the self-assembly of collagen are also being investigated. While aromatic residues are extremely rare in natural collagen, aromatic-aromatic interactions have been found to accelerate self-assembly in some collagen systems.[35]

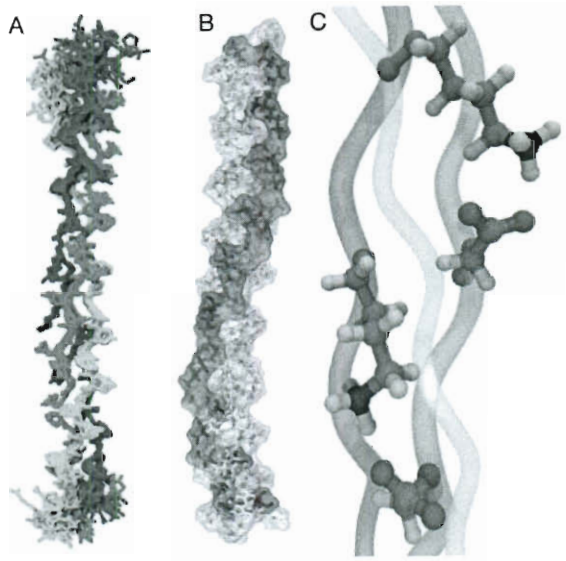

Figure 1.4. NMR structure of $(PKG)_{10}\cdot(DOG)_{10}\cdot(POG)_{10}$. A) Superposition of the 15 lowest energy conformers, where $(PKG)_{10}$ is shown in blue, $(DOG)_{10}$ is shown in red, and $(POG)_{10}$ is shown in green. B) Representation of the lowest energy conformer highlighting the position of charged amino acids. C) Expanded view of two salt bridges observed in B with distinct conformations. Figure from reference 19.

The proline-hydroxyproline-glycine sequence, $(POG)_n$, has also been used for the basis of modified collagen-mimetics that self-assemble into novel nanostructures such as peptide florettes and disks. The Chmielewksi group has prepared microflorettes (Figure 1.5) from triple-helical collagen-mimetics that follow this motif.[36] In these structures, triple helices are assembled from $(POG)_9$ peptides that have been modified at both termini with metal-chelating groups. Upon the addition of metal ions to the system, the chelating groups bind the metal ions, triggering head-to-tail assembly of the attached triple helices. This results in a material that assembles in microflorettes. Another (POG)-type peptide incorporates bypyridyl ligands radiating from the triple-helical core. Upon the addition of Fe(II), the iron is complexed by bipyridine groups, which stabilizes the helices and results in radial self-assembly to form disks that are ~ 10 nm in height.[37]

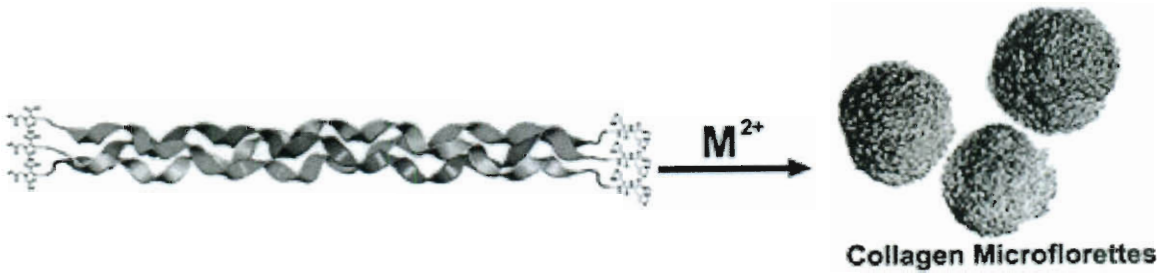

Figure 1.5. Self-assembly of a collagen-minetic peptide based on the $(POG)_n$ motif. This peptide contains nine (POG) repeats in the central region of the peptide and metal-binding ligands at the termini. Figure from 36.

3. Alpha Helical Coiled Coils

Another motif that employs multiple levels of self-assembly is the alpha-helical coiled coil structure. The alpha helix is one of several common secondary structures found in proteins. Alpha helices are characterized by a twisting peptide backbone in which the amine proton of an amino acid in arbitrary position *i* interacts with the carbonyl oxygen of the amino acid in the *i+3* position. This extensive hydrogen bonding between backbone atoms causes all of the amino acid side chains to point outward, away from the helical core. In the coiled coil motif, two distinct peptides, each right-handed alpha helices, wrap around each other to form a left-handed superhelix. This occurs when the hydrophobic amino acids are segregated to one side of the helix and the hydrophilic amino acids are segregated to the opposite side. Assembly is driven by the hydrophobic effect, where the hydrophobic faces of each helix pack together and the hydrophilic faces face outward, interacting with the aqueous environment. A coiled coil may be created if, in a peptide with amino acid sequence $(abcdefg)_n$, hydrophobic amino acids are placed in the a and d positions and hydrophilic amino acids are placed in the e and g positions (Figure 1.6). In naturally occurring coiled coils, amino acids in the e and g positions have

complementary charges and participate in salt bridges.[38] While many of coiled coils have been observed as dimers, larger helical bundles such as trimers, tetramers, pentamers, and hexamers have also been observed.[20]

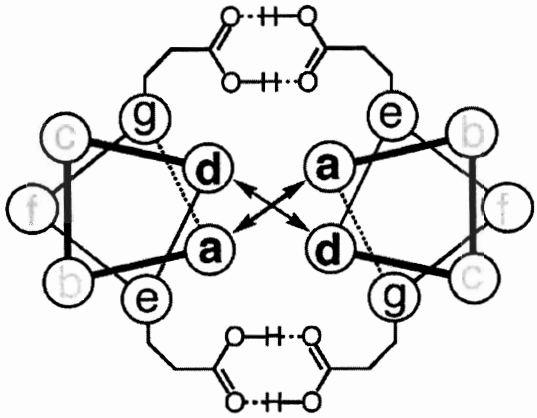

Figure 1.6. Representation of an α-helical dimeric coiled coil. Residues that participate in hydrophobic packing are shown in black. Residues capable of forming salt bridges are shown in red, and hydrophilic residues are shown in green. Figure from reference 38.

Coiled coils were first postulated by Pauling, Corey, and Crick,[39,40] and have since been found extensively in nature, for example, in leucine zippers,[41] tropomyosin,[42] and the gp41 protein of the HIV viral envelope.[43] The gp41 viral protein is a membrane-spanning protein that contains a trimeric coiled coil at its core. The interactions between the helices are points of hydrophobic contact, largely with isoleucine residues, that take place at the a and d positions of the heptads.[44] This core region of gp41 is highly conserved between similar viruses and is thought to be responsible for fusion of the HIV particle with the host cell.[43] As of the 1990's, over 200 natural proteins containing coiled coils had been identified.[45] Several of these structures are shown in Figure 1.7.

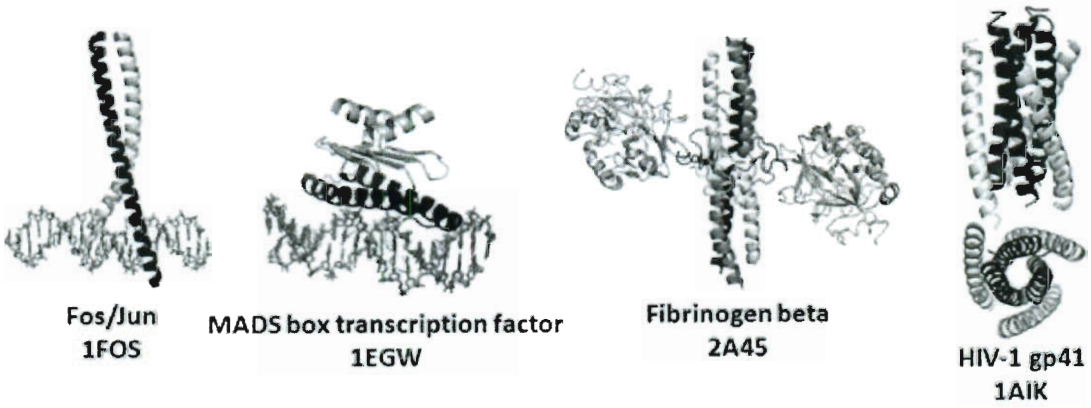

Figure 1.7. Examples of several coiled-coil-containing proteins found in nature. Figure adapted from 20.

Naturally occurring coiled coils often have deviations from the traditional heptad motif, which lead to disruptions in structure.[20] This has led to the creation of synthetic coiled coils using a few basic design principles. For the creation of a coiled coil dimer from a peptide with repeating heptad sequence $(abcdefg)_n$, these principles are as follows: first, isoleucine and leucine are the preferred residues for the a and d positions. Second, lysine and glutamic acid are the preferred residues for the e and g positions and form stable salt bridges with one another when one of each type is used. Third, hydrophobic residues are to be avoided in positions b, c, e, and g.[20] Incorporation of these design features ensures maximum hydrophobic contact along the edges of the two helices, with additional stabilization imparted by salt bridges between lysine and glutamic acid. Synthetic coiled coils have found application as linkers in drug delivery,[46] aids in protein purification,[47] and in biosensors.[48]

4. Beta Sheet Structures

The final secondary structure that is commonly observed in peptide self-assembly is the beta sheet. Beta sheet secondary structure arises not from intertwined peptide strands (as in coiled coils and triple helices), but rather from a more extended orientation of the polypeptide strand. In this structure, the individual atoms of the backbone occupy a pleated pattern, staggered evenly just above and below the long axis of the peptide strand. For this reason, beta sheets are often called beta pleated sheets. This backbone conformation is stabilized by hydrogen bonding between the backbones of adjacent peptide strands. In nature, beta strands are most often found hydrogen-bonded to other beta strands, forming a sheet-like structure. Hydrogen bonding can be parallel or anti-parallel. In a parallel beta sheet, all peptide strands are oriented in the same way. Hydrogen bonding takes place between the carbonyl oxygens in the peptide backbone and the amide protons closest to them in the adjacent peptide backbone, although these atoms are offset slightly from one another. In an antiparallel beta sheet, each beta strand alternates orientation with the previous strand, so that the N-terminus of one peptide is matched with the C-terminus of peptides on either side of it. Hydrogen bonding still takes place between the carbonyl oxygens and amide protons but the atoms are not offset from one another in the plane of hydrogen bonding as they are in a parallel beta sheet.

Peptides can assemble using the beta sheet conformation to produce a number of structures. One structure found frequently in nature is the beta barrel. A beta barrel is simply a beta sheet that is twisted so that the last strand in the beta sheet can hydrogen bond with the backbone of the first. The inter-strand hydrogen bonding is the stabilizing

force for this self-assembly, which results in a cylindrical structure that is commonly found within cell membranes.[49] Beta barrels typically range from as few as 8 beta strands to 22 or more.[50] Beta barrels of differing sizes can act as pores for differing molecules, making this motif extremely useful in biology. This provides a mechanism for creating toxicity. It is estimated that approximately 2-3% of the Gram-negative bacterial genome codes for genes with beta barrel protein products.[49] Another beta-sheet-derived secondary structure motif is the beta hairpin. A hairpin consists of a single polypeptide containing two beta strands (Figure 1.8). The first strand leads to a short loop, which allows the peptide backbone to fold 180° over the course of two to five amino acids, and this loop is connected to the second strand, another beta strand. Thus, a beta hairpin is a two-strand antiparallel beta sheet. The formation of beta hairpins is thought to be crucial in the early steps of protein folding *in vivo*.[51]

Figure 1.8. The peptide VKVKVKTKV^{L}PPTKVKTKVKV-NH_2 folds reversibly into a beta hairpin, which can subsequently self-assemble into larger structures. Adapted from reference 52.

Both beta hairpins and individual beta strands are capable of forming a number of nanostructures in synthetic systems. Many of these structures are high aspect ratio supramolecular assemblies that can be classified as nanotapes, nanoribbons, and nanofibers. While similar in nature, a few subtle features differentiate these structures from one another. It is useful to keep in mind that in beta sheet structures, one half of the amino acid side chains are segregated to one face of the sheet, and the other half of the side chains are segregated to the opposite face of the sheet. Nanotapes are amphiphilic

structures in which one face of the tape is hydrophilic and the other face is hydrophobic. In any one environment, one side of the molecule will show an affinity for a particular surface, similar to a piece of adhesive tape. Because the hydrophobic face would otherwise be exposed in an aqueous solution, nanotapes often fold into helical structures, even though the component peptides still reside in the beta sheet conformation.[53, 54] When two tape-like assemblies associate, they form a nanoribbon with a hydrophobic interior and hydrophilic exterior. These nanoribbons are relatively flat and display a propensity to twist along their long axis.[8, 53] When this twist is absent, these nanostructures are termed nanofibers, which will be discussed in more detail in the next section.

D. Peptide Nanofiber Self-Assembly

Self-assembled peptide nanofibers are an excellent example of one such nanostructure that utilizes interactions between amino acids. A nanofiber may be defined as a long, thin object of high aspect ratio with dimensions on the nanoscale. Nanofibers differ from nanotubes in that nanofibers are not hollow, although intercalation of non-peptide molecules within the fibers is sometimes possible. Peptide nanofibers are useful for a number of reasons. Synthetic fibrous networks are capable of mimicking the extracellular matrix of the body. Peptide nanofibers often form hydrogels, which can be used for drug and cell delivery. Finally, fibrous peptide assemblies can also indicative of disease states, for example, Alzheimer's disease. As a result, many self-assembling peptide nanofiber systems have been prepared and studied. Peptide nanofibers can generally be divided into three types: nanofibers derived from hybrid peptide materials (such as peptide

amphiphiles), nanofibers derived from alpha helices, and nanofibers derived from beta sheets.

1. Peptide Amphiphile Nanofibers

Peptide amphiphiles are another class of self-assembled peptides with novel properties. A peptide amphiphile consists of an oligopeptide block and an alkyl tail (with a 16-carbon chain, for example) that is covalently attached to the peptide portion of the molecule. This creates an amphiphilic molecule that, upon screening of the charges on the molecule at low pH, self-assembles into cylindrical micelles of uniform diameter (Figure 1.9). These cylindrical micelles are approximately 8 nm in diameter and microns in length.[9] This self-assembly also results in the reversible formation of a self-supporting hydrogel. Driven by the hydrophobic effect and the conical shape of the molecule, the lipid moieties pack into the center of the nanofiber, which the peptide moieties remain on the periphery of the fiber, interacting with each other through hydrogen bonding. The hydrogen bonding resembles that of a parallel beta sheet, which imparts stability and rigidity to the nanofibers.[55] This template allows some flexibility of the amino acid selection, and different amino acids may be incorporated into the sequence to suit a variety of purposes. Although not required, the incorporation of cysteine residues near the alkyl tail of the molecule imparts additional robustness to the fibers when these cysteine residues are oxidized to form disulfide bonds.[9, 56] The sequences IKVAV (derived from laminin) and RGD (derived from fibronection) are cell recognition sequences that may be

incorporated closer to the periphery of the assembled fiber.[9, 57] Modified amino acids such as phosphoserine can nucleate crystals on the surface of the nanofiber.

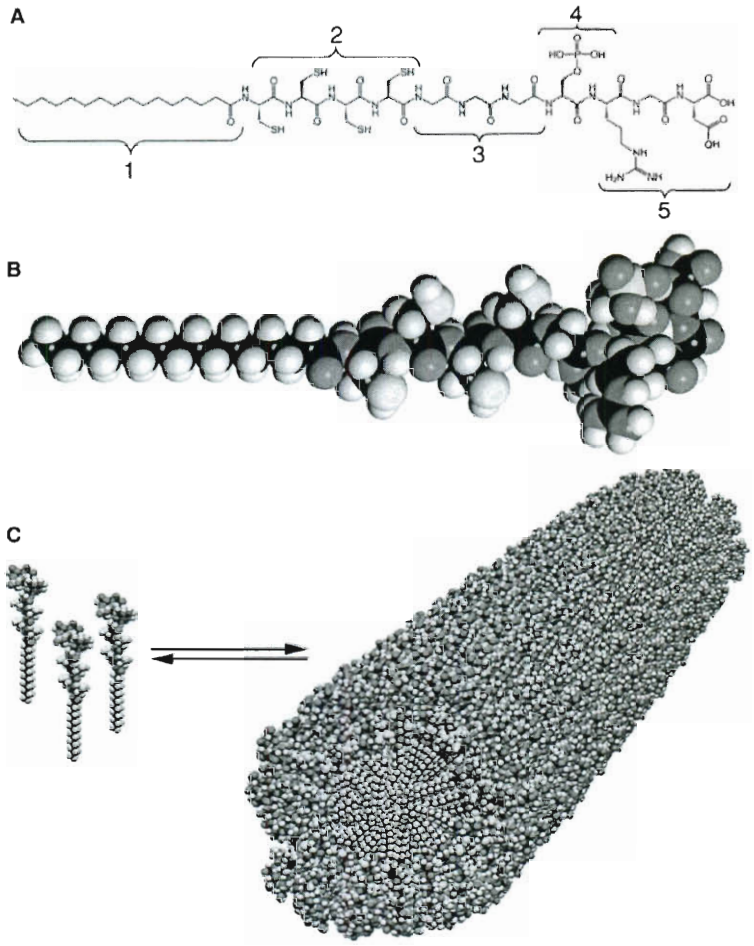

Figure 1.9. A) Structure of a peptide amphiphile, incorporating five key structural features: 1 denotes an alkyl tail that imparts hydrophobicity. 2 denotes four cysteine residues that may be oxidized to form disulfide bonds. 3 is a linker region composed of three glycine residues. 4 denotes a phosphorylated serine residue that is designed to direct biomineralization, and 5 is the cell recognition sequence RGD. B) Model of a peptide amphiphile. C) Schematic of peptide amphiphile self-assembly. Figure from reference 9.

In addition, the mechanical properties of these systems can be tuned by altering the amino acid selection.[55] Peptide amphiphile nanofibers have found application as aids in hydroxyapatite mineralization,[9] central nervous system regeneration,[57] and nucleation of CdS nanocrystals.[58]

2. Alpha Helical Coiled Coil Nanofibers

Peptide nanofibers may also be assembled from coiled coils. There are a few naturally occurring coiled coil systems with extensive self-assembly. Intermediate filaments, for example, are constructed from coiled coil dimers that self-assemble to form tetramers, octamers, and larger structures that eventually result in filament formation.[59] These filaments make a significant contribution to the mechanical properties of the cell. Synthetic systems have brought with them the possibility of nearly infinite self-assembly to form nanofibers. Potekhin and coworkers have prepared a 34-amino acid peptide that was rationally designed to form pentameric coiled-coils.[60] This peptide self-assembles into uniform fibers at acidic pH that are ~2.5 nm in diameter and can be hundreds of nanometers in length (Figure 1.10). Some systems have incorporated design elements to allow fiber elongation as well as lateral assembly.

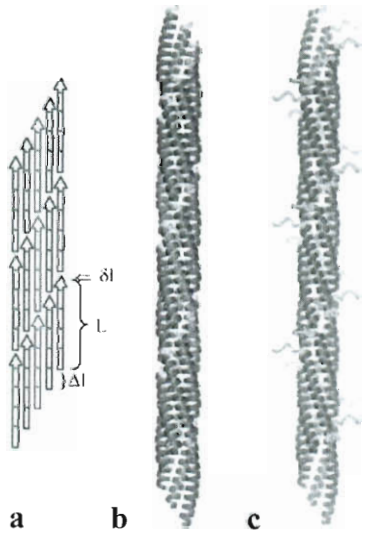

Figure 1.10. a) Two-dimensional representation of a five-stranded fibril. b) Structural model of a five-stranded fibril containing 34-residue peptides. (One strand is shown in blue, N-termini are in yellow). c) Model of the fibril built of peptides with five additional residues (shown in yellow) of non-coiled coil sequence. The structures were modeled and the picture was generated by the Insight II package. Figure adapted from reference 60.

The Woolfson group has prepared coiled coil extended fibers from two 28-residue peptides.[61] In this system, the individual helices in the dimer were offset from one another by two heptad repeats (14 residues) in order to create "sticky ends" that would encourage other staggered dimers to pack with the original dimer in a complementary manner. As this process is repeated with many staggered dimers, the fiber grows longer. Lateral assembly is also observed in this system, with a mean fiber width of 43 nm. The Woolfson group has further developed this possibility for lateral assembly in coiled coil nanofibers, using complementary leucine zipper coiled coils to prepare fibers that are more than 50 nm wide and over 10 μm long.[62]

3. Self-assembled Beta Sheet Peptide Nanofibers

The beta sheet nanofiber is one another subgroup of self-assembled peptide fibers. In nature, this motif can be found in amyloid fibrils, characteristic of Alzheimer's disease. Alzheimer's disease is a progressive disease involving neurodegeneration and dementia, accounting for approximately 50 to 70% of late-onset dementia.[63] Symptoms can be correlated with the formation of amyloid fibrils.[64, 65] There is no cure and treatment options are minimal. Thus, the fibrous networks found in the brain tissue of Alzheimer's patients provide a point of interest for studying the self-assembled beta sheet nanofiber structure. Amyloid fibrils are composed of beta hairpin peptides that self-assemble into protofilaments or protofbrils 3 nm wide, where the peptide backbone is perpendicular to the filament axis. This is termed a "cross-β" structure. While these cross-β assemblies may be formed by a number of peptides, the most common peptide involved in these

structures is amyloid-β, or Aβ. Protofilaments of assembled Aβ subsequently assemble into fibrils 5-10 nm in diameter.[65]

There are two variants of amyloid-β: a 40-amino acid and a 42-amino acid polypeptide, termed Aβ40 and Aβ42, respectively.[66, 67] Both are derived from amyloid precursor protein (APP), a membrane-spanning protein whose function is not known despite extensive study.[65,67] However, it is known that mutations in the gene for APP, as well as mutations in proteins that handle APP processing, can lead to earlier onset of Alzheimer's disease. APP is expressed in all cells and is regularly cleared from cells by enzymatic degradation. APP is cleaved by secretase enzymes to yield individual Aβ fragments, which go on to self-assemble into protofilaments and then fibrils.

Closer examination of Aβ shows that the first 16 residues are disordered, while residues 17-42 participate in the beta hairpin that is characteristic in Aβ protofibrils. This hairpin is composed of two parallel beta sheets derived from amino acids 18-26 (β1) and 31-42 (β2).[68] The structure of residues 17-42 is shown in Figure 1.11.

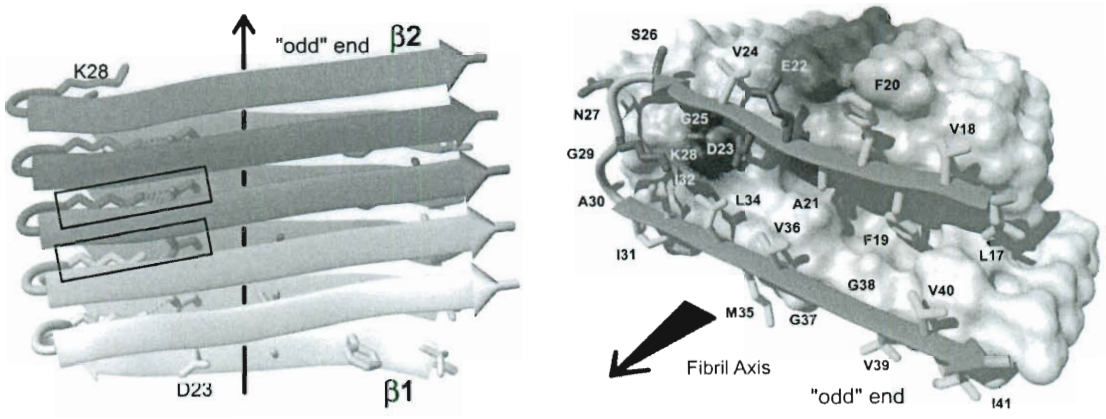

Figure 1.11. The 3D structure of an amyloid fibril. Left: ribbon diagram of the core structure of residues 17–42 illustrating the intermolecular nature of the inter-β-strand interactions. Right: van der Waals contact surface polarity and ribbon diagram of the Aβ protofilament. Adapted from reference 68.

Within these regions, several candidates have been implicated as being responsible for fibril nucleation. Most of these sequences include Aβ residues 16-20, KLVFF. When added to Aβ *in vitro*, this pentapeptide fragment exhibits strong binding to Aβ and is capable of preventing fibril formation.[69, 70] The peptide FFKLVFF is also known to self-assemble in a beta sheet fashion to form amyloid fibers in methanol and trifluoroethanol.[71] Several factors drive the assembly of Aβ in biological systems. First, extensive hydrogen bonding between individual peptide backbones stabilizes the cross-β fiber structure. Second, the hydrophobic effect can drive protofibril self-assembly, as assembled structures shield hydrophobic residues such as leucine, valine, and phenylalanine from water. Finally, it has been suggested that aromatic amino acid residues, specifically phenylalanine, interact with each other in the self-assembled state via π-π stacking interactions, and that this interaction is crucial in fibril nucleation and growth.

All three of these driving forces can be utilized in synthetic systems as well. Synthetic β-sheet peptide nanofibers have been prepared by a variety of groups, including Hartgerink,[21] Pochan,[72] and Zhang.[73] The successful design of these peptides has been dependent on several factors. First, most of these peptides are relatively short in length, containing on average 16-20 amino acids. Second, these peptides employ charged residues to aid in solubility. Third, the sequences of synthetic beta sheet peptides contain alternating hydrophilic and hydrophobic amino acids, which segregate to opposite sides of the beta sheet when the peptide is folded. This creates an amphiphilic molecule that self-assembles in predictable ways. Some beta sheet-forming peptides also employ

aromatic-aromatic interactions, although these are not required for nanofiber self-assembly in synthetic systems.

Zhang pioneered the design of peptides that form beta sheet nanofibers when his group recognized a sequence of alternating hydrophilic and hydrophobic amino acids in a DNA binding protein, zuotin. In 1993 the Zhang group reported that the 16-amino acid peptide [(Ala-Glu-Ala-Glu-Ala-Lys-Ala-Lys)$_2$], termed EAK16, self-assembles in water to form beta sheet nanofibers.[74, 75] In this system, the alternating sequence of charged amino acids (glutamic acid and lysine) with alanine residues creates a hydrophilic face and a hydrophobic face. Assembly takes place when two EAK units first form a sandwiched dimer, with the alanine residues on the interior and the lysine and glutamic acid residues on the exterior. Multiple dimers can then assemble perpendicular to the peptide backbone in both directions to form nanofibers. The glutamic acid and lysine residues on the exterior of the fiber form salt bridges that stabilize self-assembly. Later, EAK16 was modified to replace glutamic acid residues with aspartic acid and lysine residues with arginine, resulting in the peptide [(Arg-Ala-Arg-Ala-Asp-Ala-Asp-Ala)$_2$], or RAD16.[76] Both of these peptides show a distinctive beta sheet signature via circular dichroism and correspondingly form nanofibers. Dried films of RAD16 were also shown to support cell attachment *in vitro* (EAK16, however, did not). This sequence was later optimized to RADA16, [(Arg-Ala-Asp-Ala-Arg-Ala-Asp-Ala)$_2$].[73, 77] RADA16 has been shown to support cell growth and attachment *in vitro* and has been developed commercially under the name Puramatrix. Puramatrix self-assembles into a hydrogel upon contact with cell culture media or salt solutions, and this hydrogel has since been used as a cell scaffold for a variety of applications.[78]

Pochan and Schneider also developed a peptide system that self-assembles into beta sheet nanofibers. In 2002, they reported that MAX1, a 20-amino acid peptide, VKVKVKVKV-^{D}PPT-VKVKVKV-NH_2, folds reversibly into a beta-hairpin conformation upon exposure to basic pH (Figure 1.12).[72] In this system, when the pH is raised to 9, the lysine residues become deprotonated, eliminating the net charge of the peptide. Without ion-ion repulsion to discourage self-assembly, the peptide folds into a beta hairpin. This is encouraged by two factors. First, peptide folding into a hairpin allows all of the hydrophobic valine residues to be in contact with one another at the center of the hairpin. Valine has a particularly high propensity to form beta sheet structures and is thus ideally suited for this system. Second, the proline residues enable the peptide to form the beta turn necessary for hairpin formation. Further self-assembly takes place as β-hairpin units assemble perpendicular to the hairpin axis to create long nanofibers, and this step is stabilized by hydrogen bonding between adjacent peptides. Nanofiber formation is accompanied by the transition to a viscoelastic hydrogel. Acidification of the solution results in the unfolding of the hairpin and the dissolution of extentive nanofiber network. Modifying MAX1 to contain two threonine residues in hydrophobic positions resulted in the synthesis of MAX3. MAX3 folds in response to an increase in temperature, forming a hydrogel at approximately 60°C. The peptide unfolds upon cooling to 5°C, dissolving the nanofibers and triggering a transition from the gel state back to a liquid state.[52] When one lysine in the MAX1 sequence is changed to a glutamic acid residue, thereby reducing the overall charge on the peptide, the hydrogelation kinetics can be modified. As a result, this peptide, MAX8, forms a hydrogel much faster than does MAX1.[79] Hydrogels formed from beta hairpins such as

MAX1 and MAX8 experience shear thinning (one form of yielding to applied stress) and thus can be easily pushed through a syringe for biomedical applications. The nanofiber network of both peptides recovers after the shear is removed, allowing the system to resume a semi-solid state.[80] This beta hairpin motif has been modified to include "strand-swapping" as a method of self-assembly, a process in which one peptide forms two complementary structures which then dimerize and subsequently form nanofibers.[81] Other peptides featuring the general MAX1 and MAX8 motifs have been adapted to direct biomineralization in the presence of alkaline phosphatase.[82]

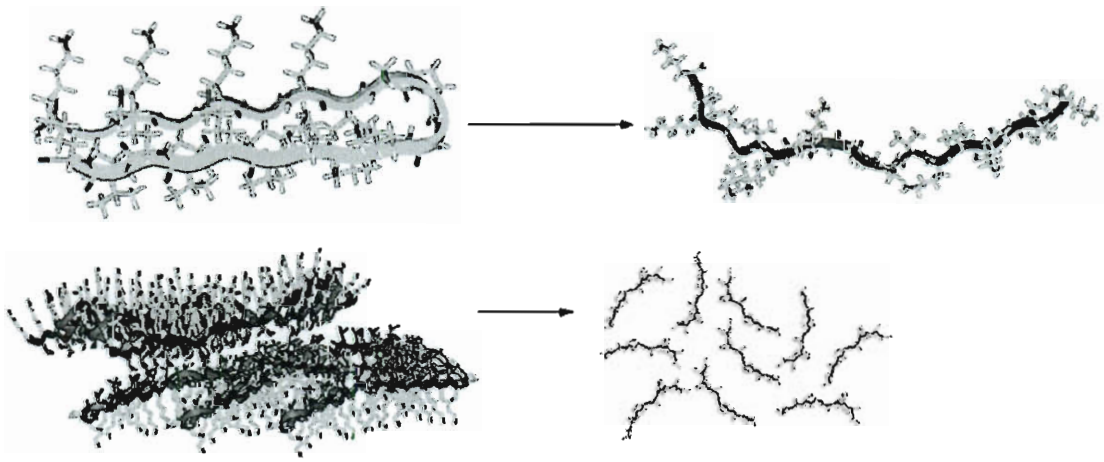

Figure 1.12. Model of the proposed beta hairpin structure of peptide MAX1. MAX1 shows reversible self-assembly to form hydrogels. Reproduced from reference 72.

Collier and colleagues have prepared an interesting variation on self-assembling beta sheet peptides. Their work on the peptide QQKFQFQFEQQ, or Q11, incorporates glutamine both as a hydrophilic and hydrophobic amino acid. The aromatic amino acid phenylalanine occupies the remaining hydrophobic amino acid positions in the beta sheet design, leading to significant aromatic-aromatic interactions in the nanofiber core. The hydrophilic positions utilize both lysine and glutamic acid. This peptide and several variations have been shown to self-assemble into beta sheets, as determined by circular

dichroism, and form hydrogels in the presence of salt.[83, 84] While the peptide sequence of Q11 itself deviates from the prototypical beta sheet template, work by the Collier group has demonstrated the truly modular nature of self-assembling peptides. They have shown that cell recognition sequences such as RGDS and IKVAV can be incorporated at the termini of the peptide without compromising either the fiber morphology or the rheological properties. In this way, they have designed extracellular matrix mimics that incorporate multiple cell-binding ligands.[85] Peptides based on Q11 have not only been investigated as extracellular matrix mimics,[84] but also as immune adjuvants.[86]

Similar peptides, based on the repeating (FKFE) unit, have also been used to construct beta sheet peptide nanofibers. While distinctly different from the Q11 sequence, $(FKFE)_n$ utilizes many of the same amino acids and forms similar nanostructures. Peptides based on this motif are derived from Zhang's EAK16 and were first pioneered by the Zhang, Kamm, and Lauffenburger groups at MIT.[87] They showed that $(FKFE)_3$ forms hydrogels at neutral pH, near the isoelectric point of the peptide.[87] This sequence was further developed by Nilsson and colleagues into a peptide that is responsive to either oxidative or reductive conditions. In this peptide, $C(FKFE)_2CG$, the cysteine residues on the termini of the peptide can be oxidized to form a disulfide bond between them, resulting in the folding of the peptide into a cyclic conformation. Upon reduction of the disulfide bond, the peptide unfolds into an extended conformation, which allows it to self-assemble into nanofibers and form hydrogels.[88] Peptides using the $(FKFE)_n$ motif rely on the same principles that govern self-assembly as many of the peptides previously discussed, although these peptides have the additional feature of utilizing aromatic-aromatic interactions in the self-assembled state. However, it is unclear how much the

interactions at the center of the nanofiber are dominated by the hydrophobic effect versus π-π stacking. To answer this question, the Nilsson group constructed a series of peptides based on the $(FKFE)_2$ structure and examined the relative contributions of hydrophobic and aromatic-aromatic interactions to peptide self-assembly.[89] In this series, phenylalanine residues were systematically replaced with alanine, valine, leucine and cyclohexylalanine (a synthetic amino acid that is sterically similar to phenylalanine but lacks aromatic character). It was found that in this series of peptides, the hydrophobic effect dominates over aromatic interactions, and that phenylalanine is not required for self-assembly into nanofibers. However, it was also observed that the peptide containing phenylalanine, $(FKFE)_2$, displayed interesting concentration and solvent-mediated polymorphism, a feature that was not observed with any other amino acid.

Finally, the Hartgerink group has developed a series of beta-sheet forming peptides called multidomain peptides (Figure 1.13). Multidomain peptides (MDPs) have two distinct regions: a central block consisting of a hydrophilic face and a hydrophobic face, and a peripheral block on each end of the peptide. The central block is composed of alternating hydrophilic and hydrophobic amino acids, which when in an extended beta sheet conformation, form the facial amphiphile that drives self-assembly. The peripheral blocks are composed of charged amino acids and limit self-assembly while simultaneously improving solubility. Self-assembly in aqueous solution is triggered by charge screening of these peripheral amino acids. Once the charge on these amino acids is neutralized, the peptides no longer repel one another and assemble into dimers, tetramers, and so on. The center of the oligomer contains the hydrophobic residues, shielded from the aqueous solvent, while the outer face interacts with water through its

hydrophilic residues. Multiple oligomers assemble along an axis perpendicular to the peptide to form extended β-sheet.[21]

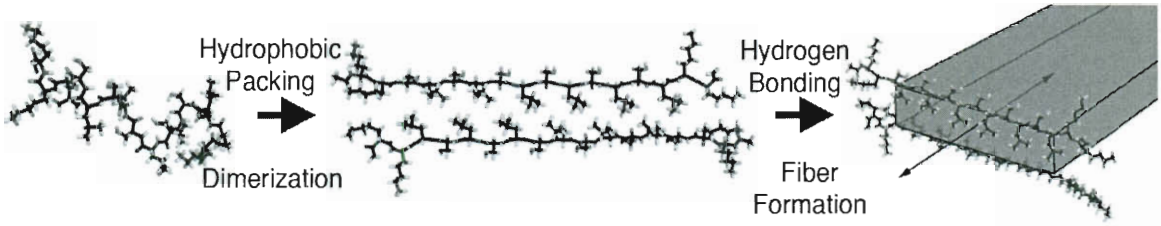

Figure 1.13. Schematic of self-assembly of multidomain peptides. Hydrophobic packing directs the formation of dimers, which then self-assemble to form fibers. Taken from reference 90.

Peptides assemble antiparallel to one another, and hydrogen bonds are formed between adjacent peptides down the length of the nanofibers. Depending on the extent of assembly, results in the formation of a hydrogel.[21] Multidomain peptide hydrogels also undergo both shear-thinning and rapid recovery after removal of the shear stress, providing the possibility that they can be utilized for injectable therapies. It was found that the specific amino acid sequence has a large impact on the strength of the gel, and that changes to the sequence result in predictable changes in the hydrogel properties.[90] Changes in sequence can also have a significant impact on fiber morphology (unpublished work). Multidomain peptide hydrogels have been developed for such applications as cell scaffolds[91] and drug release agents.[92]

E. Conclusions

Self-assembly is a process that is at work in many chemical and biological systems, both natural and synthetic. In nature, the effects of self-assembly may be observed in nucleic acid structures, lipid bilayers, and protein structures such as viral capsids, enzymes, and amyloid fibrils. These protein structures may incorporate a variety of peptide folding motifs, such as collagen-like triple helices, alpha helices, or beta sheets. We can harness the same noncovalent interactions that drive the formation of natural protein structures to construct novel synthetic systems. Indeed, synthetic systems featuring each one of these types of secondary structure have been created. One motif that is particularly relevant to this work is that of the beta sheet nanofiber. These nanofibers bear resemblance to natural amyloid-β fibrils and their study can lead to a greater understanding of amyloid-β fibril formation, as well as more immediate applications as surfactants and drug delivery agents.

References

(1) Steed, J. W.; Atwood, J. L. *Supramolecular Chemistry, Second Edition*; John Wiley & Sons, Ltd.: West Sussex, England, 2009

(2) Drain, C. M.; Lehn, J. M. *J. Chem. Soc. Chem. Comm.* **1994**, 2313-2315.

(3) Jenekhe, S. A.; Chen, X. L. *Science* **1999**, *283*, 372-375.

(4) Shen, Y. J.; Lee, Y. L. *Nanotechnology* **2008**, *19*, ARTN 045602.

(5) Khanal, B. P.; Zubarev, E. R. *Angew. Chem., Int. Ed.* **2007**, *46*, 2195-2198.

(6) Ghadiri, M. R.; Granja, J. R.; Milligan, R. A.; McRee, D. E.; Khazanovich, N. *Nature* **1993**, *366*, 324-327.

(7) Gupta, M.; Bagaria, A.; Mishra, A.; Mathur, P.; Basu, A.; Ramakumar, S.; Chauhan, V. S. *Adv. Mater.* **2007**, *19*, 858-861.

(8) Marini, D. M.; Hwang, W.; Lauffenburger, D. A.; Zhang, S. G.; Kamm, R. D. *Nano Lett.* **2002**, *2*, 295-299.

(9) Hartgerink, J. D.; Beniash, E.; Stupp, S. I. *Science* **2001**, *294*, 1684-1688.

(10) Luger, K.; Mader, A. W.; Richmond, R. K.; Sargent, D. F.; Richmond, T. J. *Nature* **1997**, *389*, 251-260.

(11) Kornberg, R. D. *Annu. Rev. Biochem.* **1977**, *46*, 931-954.

(12) Bell, S. P.; Dutta, A. *Annu. Rev. Biochem.* **2002**, *71*, 333-374.

(13) Cate, J. H.; Gooding, A. R.; Podell, E.; Zhou, K. H.; Golden, B. L.; Kundrot, C. E.; Cech, T. R.; Doudna, J. A. *Science* **1996**, *273*, 1678-1685.

(14) Chung, Y. C.; Chiu, Y. H.; Wu, Y. W.; Tao, Y. T. *Biomaterials* **2005**, *26*, 2313-2324.

(15) Zelphati, O.; Szoka, F. C. *Proc. Natl. Acad. Sci. U. S. A.* **1996**, *93*, 11493-11498.

(16) Campbell, N. A.; Reece, J. B. *Biology, Sixth Edition*; Pearson Education: San Francisco, CA, 2002; pp 329.

(17) Vellinga, J.; Van der Heijdt, S.; Hoeben, R. C. *J. Gen. Virol.* **2005**, *86*, 1581-1588.

(18) Gauba, V.; Hartgerink, J. D. *J. Am. Chem. Soc.* **2007**, *129*, 15034-15041.

(19) Fallas, J. A.; Gauba, V.; Hartgerink, J. D. *J. Biol. Chem.* **2009**, *284*, 26851-26859.

(20) Apostolovic, B.; Danial, M.; Klok, H. A. *Chem. Soc. Rev.* **2010**, *39*, 3541-3575.

(21) Dong, H.; Paramonov, S. E.; Aulisa, L.; Bakota, E. L.; Hartgerink, J. D. *J. Am. Chem. Soc.* **2007**, *129*, 12468-12472.

(22) Ketchem, R. R.; Hu, W.; Cross, T. A. *Science* **1993**, *261*, 1457-1460.

(23) Hancock, R. E. W.; Chapple, D. S. *Antimicrob. Agents Chemother.* **1999**, *43*, 1317-1323.

(24) Khazanovich, N.; Granja, J. R.; McRee, D. E.; Milligan, R. A.; Ghadiri, M. R. *J. Am. Chem. Soc.* **1994**, *116*, 6011-6012.

(25) Ghadiri, M. R.; Granja, J. R.; Buehler, L. K. *Nature* **1994**, *369*, 301-304.

(26) Dartois, V.; Sanchez-Quesada, J.; Cabezas, E.; Chi, E.; Dubbelde, C.; Dunn, C.; Granja, J.; Gritzen, C.; Weinberger, D.; Ghadiri, M. R.; Parr, T. R. *Antimicrob. Agents Chemother.* **2005**, *49*, 3302-3310.

(27) Motiei, L.; Rahimipour, S.; Thayer, D. A.; Wong, C. H.; Ghadiri, M. R. *Chem. Commun.* **2009**, 3693-3695.

(28) Fernandez-Lopez, S.; Kim, H. S.; Choi, E. C.; Delgado, M.; Granja, J. R.; Khasanov, A.; Kraehenbuehl, K.; Long, G.; Weinberger, D. A.; Wilcoxen, K. M.; Ghadiri, M. R. *Nature* **2001**, *412*, 452-455.

(29) Ramachandran, G. N.; Kartha, G. *Nature* **1954**, *174*, 269-270.

(30) Ramachandran, G. N.; Kartha, G. *Nature* **1955**, *176*, 593-595.

(31) Rich, A.; Crick, F. H. C. *Nature* **1955**, *176*, 915-916.

(32) Bella, J.; Eaton, M.; Brodsky, B.; Berman, H. M. *Science* **1994**, *266*, 75-81.

(33) Bretscher, L. E.; Jenkins, C. L.; Taylor, K. M.; DeRider, M. L.; Raines, R. T. *J. Am. Chem. Soc.* **2001**, *123*, 777-778.

(34) Russell, L. E.; Fallas, J. A.; Hartgerink, J. D. *J. Am. Chem. Soc.* **2010**, *132*, 3242-3243.

(35) Kar, K.; Ibrar, S.; Nanda, V.; Getz, T. M.; Kunapuli, S. P.; Brodsky, B. *Biochemistry* **2009**, *48*, 7959-7968.

(36) Pires, M. M.; Chmielewski, J. *J. Am. Chem. Soc.* **2009**, *131*, 2706-2712.

(37) Przybyla, D. E.; Chmielewski, J. *J. Am. Chem. Soc.* **2010**, *132*, 7866-7867.

(38) Dong, H.; Hartgerink, J. D. *Biomacromolcules* **2006**, *7*, 691–695.

(39) Pauling, L.; Corey, R. B. *Nature* **1953**, *171*, 59-61.

(40) Crick, F. H. C. *Acta Crystallogr.* **1953**, *6*, 689-697.

(41) Oshea, E. K.; Rutkowski, R.; Kim, P. S. *Science* **1989**, *243*, 538-542.

(42) Lupas, A. *Trends Biochem. Sci.* **1996**, *21*, 375-382.

(43) Chan, D. C.; Fass, D.; Berger, J. M.; Kim, P. S. *Cell* **1997**, *89*, 263-273.

(44) Tan, K. M.; Liu, J. H.; Wang, J. H.; Shen, S.; Lu, M. *Proc. Natl. Acad. Sci. U. S. A.* **1997**, *94*, 12303-12308.

(45) Lupas, A.; VanDyke, M.; Stock, J. *Science* **1991**, *252*, 1162-1164.

(46) Hodges, R. S. *Biochem. Cell Biol.* **1996**, *74*, 133-154.

(47) Tripet, B.; Yu, L.; Bautista, D. L.; Wong, W. Y.; Irvin, R. T.; Hodges, R. S. *Protein Eng.* **1996**, *9*, 1029-1042.

(48) Cachia, P. J.; Kao, D. J.; Hodges, R. S. *J. Mol. Recognit.* **2004**, *17*, 540-557.

(49) Wimley, W. C. *Curr. Opin. Struc. Biol.* **2003**, *13*, 404-411.

(50) Sansom, M. S. P.; Kerr, I. D. *Biophys. J.* **1995**, *69*, 1334-1343.

(51) Blanco, F. J.; Rivas, G.; Serrano, L. *Nat. Struct. Biol.* **1994**, *1*, 584-590.

(52) Pochan, D. J.; Schneider, J. P.; Kretsinger, J.; Ozbas, B.; Rajagopal, K.; Haines, L. *J. Am. Chem. Soc.* **2003**, *125*, 11802-11803.

(53) Aggeli, A.; Nyrkova, I. A.; Bell, M.; Harding, R.; Carrick, L.; McLeish, T. C. B.; Semenov, A. N.; Boden, N. *Proc. Natl. Acad. Sci. U. S. A.* **2001**, *98*, 11857-11862.

(54) Aggeli, A.; Bell, M.; Boden, N.; Keen, J. N.; Knowles, P. F.; McLeish, T. C. B.; Pitkeathly, M.; Radford, S. E. *Nature* **1997**, *386*, 259-262.

(55) Pashuck, E. T.; Cui, H. G.; Stupp, S. I. *J. Am. Chem. Soc.* **2010**, *132*, 6041-6046.

(56) Hartgerink, J. D.; Beniash, E.; Stupp, S. I. *Proc. Natl. Acad. Sci. U. S. A.* **2002**, *99*, 5133-5138.

(57) Webber, M. J.; Kessler, J. A.; Stupp, S. I. *J. Intern. Med.* **2010**, *267*, 71-88.

(58) Sone, E. D.; Stupp, S. I. *J. Am. Chem. Soc.* **2004**, *126*, 12756-12757.

(59) Herrmann, H.; Aebi, U. *Curr. Opin. Struc. Biol.* **1998**, *8*, 177-185.

(60) Potekhin, S. A.; Melnik, T. N.; Popov, V.; Lanina, N. F.; Vazina, A. A.; Rigler, P.; Verdini, A. S.; Corradin, G.; Kajava, A. V. *Chem. Biol.* **2001**, *8*, 1025-1032.

(61) Pandya, M. J.; Spooner, G. M.; Sunde, M.; Thorpe, J. R.; Rodger, A.; Woolfson, D. N. *Biochemistry* **2000**, *39*, 8728-8734.

(62) Papapostolou, D.; Smith, A. M.; Atkins, E. D. T.; Oliver, S. J.; Ryadnov, M. G.; Serpell, L. C.; Woolfson, D. N. *Proc. Natl. Acad. Sci. U. S. A.* **2007**, *104*, 10853-10858.

(63) Hardy, J. *Trends Neurosci.* **1997**, *20*, 154-159.

(64) Pike, C. J.; Burdick, D.; Walencewicz, A. J.; Glabe, C. G.; Cotman, C. W. *J Neurosci.* **1993**, *13*, 1676-1687.

(65) Hamley, I. W. *Angew. Chem. Int. Ed.* **2007**, *46*, 8128-8147.

(66) Masters, C. L.; Simms, G.; Weinman, N. A.; Multhaup, G.; McDonald, B. L.; Beyreuther, K. *Proc. Natl. Acad. Sci. U. S. A.* **1985**, *82*, 4245-4249.

(67) Kang, J.; Lemaire, H. G.; Unterbeck, A.; Salbaum, J. M.; Masters, C. L.; Grzeschik, K. H.; Multhaup, G.; Beyreuther, K.; Mullerhill, B. *Nature* **1987**, *325*, 733-736.

(68) Luhrs, T.; Ritter, C.; Adrian, M.; Riek-Loher, D.; Bohrmann, B.; Doeli, H.; Schubert, D.; Riek, R. *Proc. Natl. Acad. Sci. U. S. A.* **2005**, *102*, 17342-17347.

(69) Tjernberg, L. O.; Naslund, J.; Lindqvist, F.; Johansson, J.; Karlstrom, A. R.; Thyberg, J.; Terenius, L.; Nordstedt, C. *J. Biol. Chem.* **1996**, *271*, 8545-8548.

(70) Tjernberg, L. O.; Lilliehook, C.; Callaway, D. J. E.; Naslund, J.; Hahne, S.; Thyberg, J.; Terenius, L.; Nordstedt, C. *J. Biol. Chem.* **1997**, *272*, 12601-12605.

(71) Krysmann, M. J.; Castelletto, V.; Hamley, I. W. *Soft Matter* **2007**, *3*, 1401-1406.

(72) Schneider, J. P.; Pochan, D. J.; Ozbas, B.; Rajagopal, K.; Pakstis, L.; Kretsinger, J. *J. Am. Chem. Soc.* **2002**, *124*, 15030-15037.

(73) Holmes, T. C.; de, L., S; Su, X.; Liu, G. S.; Rich, A.; Zhang, S. G. *Proc. Natl. Acad. Sci. U. S. A.* **2000**, *97*, 6728-6733.

(74) Zhang, S. G.; Holmes, T.; Lockshin, C.; Rich, A. *Proc. Natl. Acad. Sci. U. S. A.* **1993**, *90*, 3334-3338.

(75) Zhang, S. G.; Lockshin, C.; Cook, R.; Rich, A. *Biopolymers* **1994**, *34*, 663-672.

(76) Zhang, S. G.; Holmes, T. C.; DiPersio, C. M.; Hynes, R. O.; Su, X.; Rich, A. *Biomaterials* **1995**, *16*, 1385-1393.

(77) Yokoi, H.; Kinoshita, T.; Zhang, S. G. *Proc. Natl. Acad. Sci. U. S. A.* **2005**, *102*, 8414-8419.

(78) Misawa, H.; Kobayashi, N.; Soto-Gutierrez, A.; Chen, Y.; Yoshida, A.; Rivas-Carrillo, J. D.; Navarro-Alvarez, N.; Tanaka, K.; Miki, A.; Takei, J.; Ueda, T.; Tanaka, M.; Endo, H.; Tanaka, N.; Ozaki, T. *Cell Transplant* **2006**, *15*, 903-910.

(79) Haines-Butterick, L.; Rajagopal, K.; Branco, M.; Salick, D.; Rughani, R.; Pilarz, M.; Lamm, M. S.; Pochan, D. J.; Schneider, J. P. *Proc. Natl. Acad. Sci. U. S. A.* **2007**, *104*, 7791-7796.

(80) Yan, C. Q.; Altunbas, A.; Yucel, T.; Nagarkar, R. P.; Schneider, J. P.; Pochan, D. J. *Soft Matter* **2010**, *6*, 5143-5156.

(81) Nagarkar, R. P.; Hule, R. A.; Pochan, D. J.; Schneider, J. P. *J. Am. Chem. Soc.* **2008**, *130*, 4466-4474.

(82) Gungormus, M.; Branco, M.; Fong, H.; Schneider, J. P.; Tamerler, C.; Sarikaya, M. *Biomaterials* **2010**, *31*, 7266-7274.

(83) Collier, J. H.; Messersmith, P. B. *Bioconjugate Chem.* **2003**, *14*, 748-755.

(84) Jung, J. P.; Nagaraj, A. K.; Fox, E. K.; Rudra, J. S.; Devgun, J. M.; Collier, J. H. *Biomaterials* **2009**, *30*, 2400-2410.

(85) Collier, J. H. *Soft Matter* **2008**, *4*, 2310-2315.

(86) Rudra, J. S.; Tian, Y. F.; Jung, J. P.; Collier, J. H. *Proc. Natl. Acad. Sci. U. S. A.* **2010**, *107*, 622-627.

(87) Caplan, M. R.; Moore, P. N.; Zhang, S. G.; Kamm, R. D.; Lauffenburger, D. A. *Biomacromolecules* **2000**, *1*, 627-631.

(88) Bowerman, C. J.; Nilsson, B. L. *J. Am. Chem. Soc.* **2010**, *132*, 9526-9527.

(89) Bowerman, C. J.; Ryan, D. M.; Nissan, D. A.; Nilsson, B. L. *Mol. BioSyst.* **2009**, *5*, 1058-1069.

(90) Aulisa, L.; Dong, H.; Hartgerink, J. D. *Biomacromolecules* **2009**, *10*, 2694-2698.

(91) Galler, K. M.; Aulisa, L.; Regan, K. R.; D'Souza, R. N.; Hartgerink, J. D. *J. Am. Chem. Soc.* **2010**, *132*, 3217-3223.

(92) Wang, Y.; Bakota, E. L.; Chang, B. H. J.; Entman, M.; Hartgerink, J. D.; Danesh, F. *J. Am. Soc. Nephrol.* DOI:10.1681/ASN.2010040403

Chapter 2: Sequence-Nanostructure Relationships in Multidomain Peptides

In recent years, self-assembling peptide hydrogels have shown promise as a growing class of synthetic biomaterials and have been investigated in a wide variety of applications, including cell scaffolds[1-4] and drug delivery agents.[5-7] The Hartgerink lab has rationally designed a series of multidomain peptides based on the concept of molecular frustration. In a frustrated system, different portions of a single molecule have tendencies that oppose one another. Multidomain peptides (MDPs) have an ABA block motif in which the central B block is composed of a hydrophilic face and a hydrophobic face to give the peptide its amphiphilic nature, while the peripheral A blocks are composed of charged amino acids. The role of the charged A block is to increase solubility and control self-assembly. The A and B blocks discourage and encourage self-assembly, respectively, creating a frustrated situation in which self-assembly is controlled by the environmental conditions. In the presence of salts, self-assembly of multidomain peptides in aqueous solution results in extended β-sheet nanofibers, a structure that is stabilized by hydrogen bonding between adjacent peptide backbones along the length of the fiber. Assembly of nanofibers is sometimes accompanied by the formation of a hydrogel.[8] Their truly modular nature, which allows many design features to be incorporated, gives multidomain peptides an advantage over some of the other beta sheet-forming structures previously discussed. Taking advantage of this modularity, the Hartgerink lab has been able to isolate the effects of individual amino acids on the resulting nanostructures. Nanofiber formation of multidomain peptides is a highly conserved characteristic for this design motif and is correlated with a beta sheet

secondary structure. However, nanofiber morphology, as well as rheological properties of the peptide hydrogels, can be highly sensitive to specific amino acid selection.[9]

A. Sequence Tuning of Multidomain Peptides*

First generation multidomain peptides were synthesized with a repeating glutamine-leucine (QL) motif in the central B block of the peptide. Glutamine is a moderately hydrophilic amino acid featuring an amide group in the side chain. This amide group interacts with the solvent while the leucine residues engage in hydrophobic packing in the center of the nanofiber. Our lab initially prepared a series $K_2(QL)_mK_2$ where m ranged from 2 to 6, and a second series $K_n(QL)_6K_n$ where n ranged from 0 to 4 (Figure 2.1). The secondary structure of the peptides was examined by circular dichroism (CD), and morphology was examined by vitreous ice cryo-TEM.

---

* This section is based on: He Dong, Sergey E. Paramonov, Lorenzo Aulisa, Erica L. Bakota, and Jeffrey D. Hartgerink. Self-Assembly of Multidomain Peptides: Balancing Molecular Frustration Controls Conformation and Nanostructure. *J. Am. Chem. Soc.*, **2007,** 129, 12468-12472.

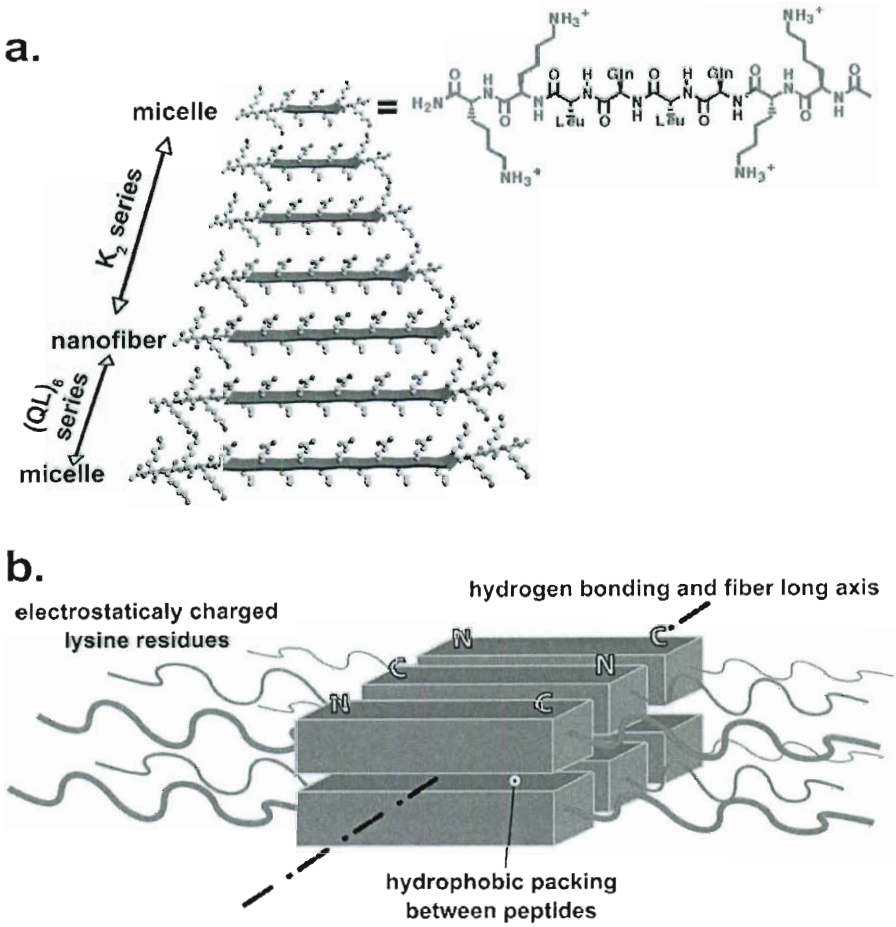

Figure 2.1. a) Primary structures of the K_2 and $(QL)_6$ series of peptides showing the relative domain sizes. b) Proposed model of nanofiber self-assembly indicating hydrophobic packing region (blue), axis of hydrogen bonding (black), and repulsive positive charges (red).

1. $K_2(QL)_mK_2$ series

It was found that for the $K_2(QL)_mK_2$ series, all of the peptides were soluble in water at pH 7. Self-assembly of these peptides was triggered by charge screening with added salts, such as phosphate buffer. Screening of the positively charged lysine residues can also be achieved by pH adjustment, although initial characterization of these systems was carried out at pH 7. The peptides $K_2(QL)_2K_2$, $K_2(QL)_3K_2$, and $K_2(QL)_4K_2$ showed a random coil conformation by CD, and this was accompanied by amorphous aggregates observed via

cryo-TEM (Figure 2.2). No nanofibers were observed. This indicates that although these peptides contain a short block of alternating hydrophilic and hydrophobic amino acids, the influence of this central block was not sufficient to overcome the charge repulsion provided by the four lysine residues flanking the central region. As more (QL) repeats were added, however, the size of the B block became sufficient to direct self-assembly into organized nanostructures. $K_2(QL)_5K_2$ shows a weak beta sheet secondary structure by circular dichroism, and the cryo-TEM of this peptide shows both small aggregates and short nanofibers with a diameter of 5 ± 1 nm. The presence of five leucines is just able to balance the electrostatic repulsion of lysine, but the population is not uniform, containing significant fractions of both amorphous and fibrous morphologies. The appearance of nanofibers is believed to be due to peptide's secondary structural transition into organized β-sheet aggregates. $K_2(QL)_6K_2$ shows a distinct beta sheet signature via CD and clear, individual nanofibers of uniform diameter (6 ± 1 nm), controlled length (120 ± 30 nm), and no amorphous aggregates by cryo-TEM. These fibers appear to be finite in length, however, due to the competing forces towards assembly and disassembly. With four lysine residues and six (QL) repeats, electrostatic repulsion is just balanced out by the tendency for hydrophobic packing and backbone hydrogen bonding, resulting in distinct nanostructures.

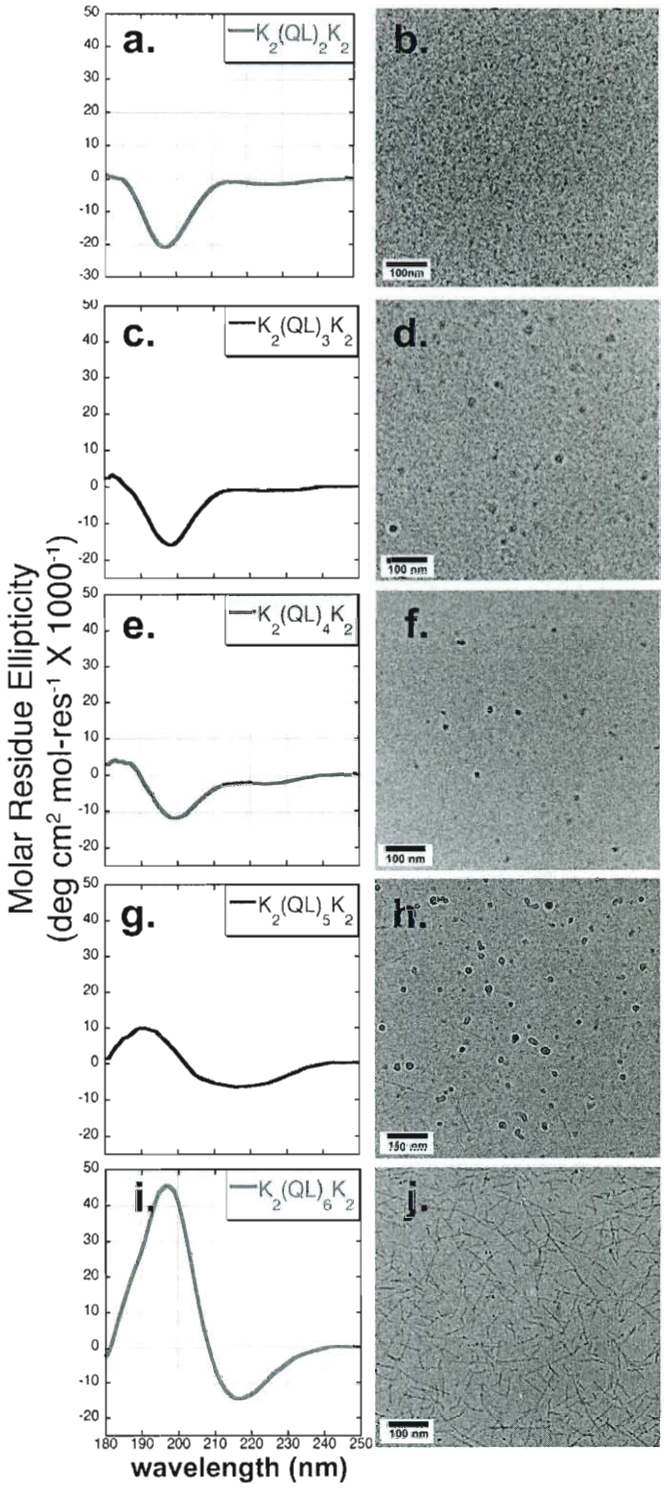

Figure 2.2. CD spectra and corresponding cryo-TEM images of the K_2 series of peptides at neutral pH. a), b) CD and TEM of $K_2(QL)_2K_2$, c), d) CD and TEM of $K_2(QL)_3K_2$, e), f) CD and TEM of $K_2(QL)_4K_2$, g), h) CD and TEM of $K_2(QL)_5K_2$, i), j) CD and TEM of $K_2(QL)_6K_2$.

2. $K_n(QL)_6K_n$ series

In this series, the number of charged residues on either side (n) was varied from 0 to 4. When n=0, the resulting peptide $(QL)_6$ is completely insoluble in water at any pH (it is, however, soluble in neat TFA). Dry TEM of $(QL)_6$ shows dense networks of aggregated fibers. FT-IR shows a strong beta sheet structure, indicating that hydrophobic packing is indeed taking place, but without any charged residues to render the nanofibers soluble, any nanofibers formed are simply precipitating out of solution. Likewise, $K(QL)_6K$ is insoluble in water, regardless of pH. However, when the total number of lysine residues is increased to four (n=2), distinct, soluble nanofibers are formed (Figure 2.3). Raising the n to 3 results in much shorter nanofibers and the presence of amorphous aggregates, suggesting that the assembly and disassembly forces are once again out of balance, slightly favoring the disassembled state. Adding a fourth lysine residue on each side of the peptide (n=4) results in the absence of fibers altogether. At n=4, the CD spectrum begins to resemble a weak alpha helix rather than a beta sheet.

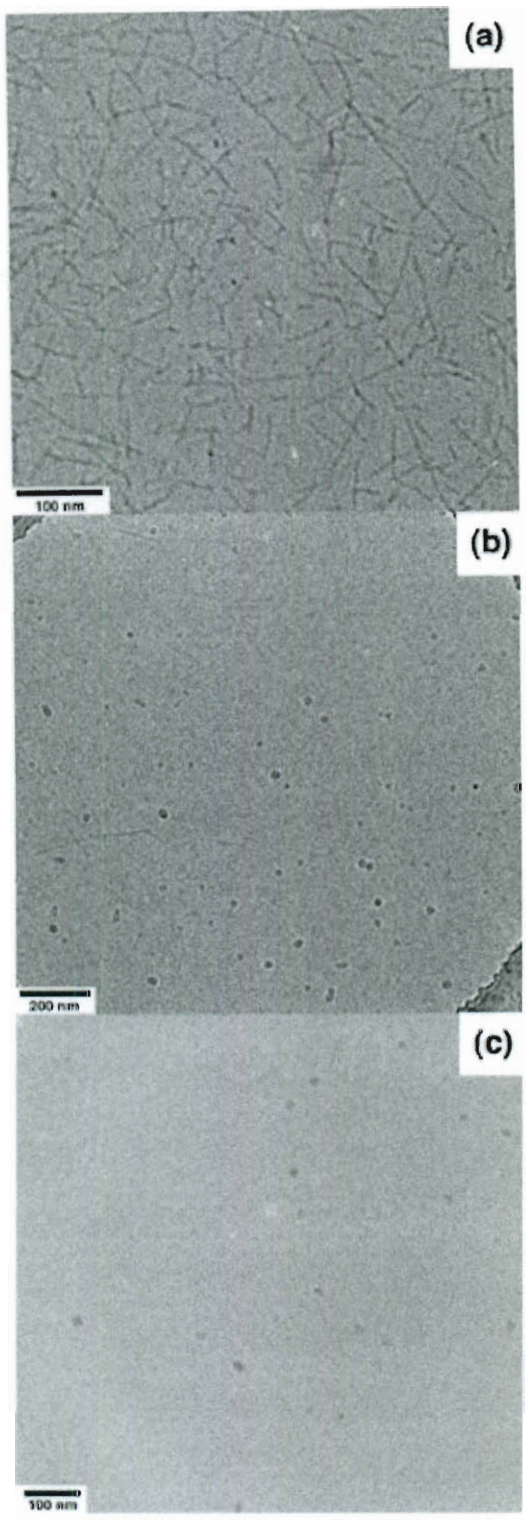

Figure 2.3. Cryo-TEM images of a) $K_2(QL)_6K_2$, b) $K_3(QL)_6K_3$, c) $K_4(QL)_6K_4$ at 1wt %, 10mM Tris, pH 7.4.

3. A Prototype is born

Of the ten peptides studied, only $K_2(QL)_6K_2$ was able to consistently produce nanofibers with predictable dimensions and morphology. Six (QL) repeats seems to be the ideal number for balancing hydrophobic packing and hydrogen bonding with the repulsive nature of the charged lysines.

To further investigate the structure of $K_2(QL)_6K_2$ nanofibers, oriented FT-IR studies were performed (Figure 2.4). This allowed us to determine the orientation of hydrogen bonding with respect to the fiber long axis (parallel vs. antiparallel). FT-IR shows a strong antiparallel component, particularly in the grazing angle mode where this band is enhanced, at 1692 cm^{-1}. This confirmed the model of self-assembly predicting antiparallel β-sheet orientation with the axis of hydrogen bonding parallel to the nanofiber and the peptide backbone oriented perpendicular to the fiber axis.

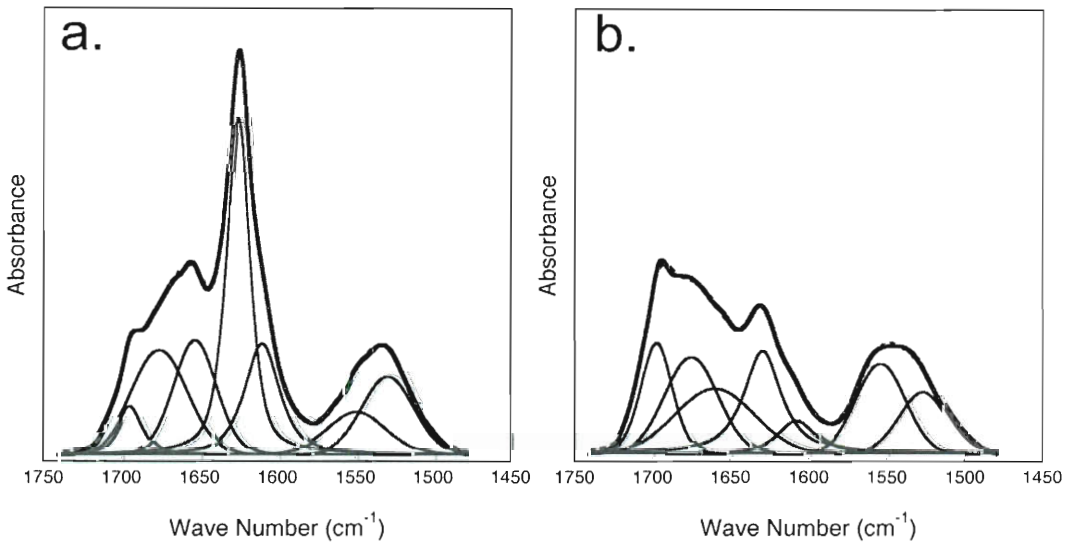

Figure 2.4. FT-IR of the amide I and amide II region of $K_2(QL)_6K_2$: a) sample examined after spin coating onto a CaF_2 window with the IR beam normal to the window (and thus the fiber long axis) surface; b) sample spin coated onto gold mirror and examined by grazing angle (80°) IR. Spectra were baseline corrected and deconvoluted, shown in gray.

If charge repulsion is the primary force preventing aggregation of these fibers, increasing ion concentration or pH should increase the fiber length. To test this, samples of $K_2(QL)_6K_2$ were prepared in 10 mM Tris pH 7.4 with 150 mM NaCl. Cryo-TEM reveals fibers with length increased to 150 ± 45 nm but these samples remain soluble and do not gel. Increasing the NaCl concentration to 1 M resulted in a highly viscous solution and dramatically increased fiber length ("infinite" length) as observed by TEM. Exceeding the pK_a of lysine at a pH of 12 effectively eliminates all charge on the peptide, and the peptide rapidly aggregates into a white suspension that eventually precipitates. Cryo-TEM of the sonicated dispersions of the high pH precipitate (Figure 2.5.c) reveals a dense matrix of infinite length fibers. Cryo-TEM also revealed fiber diameters of 6 nm, although fiber heights could not be accurately observed by this method.

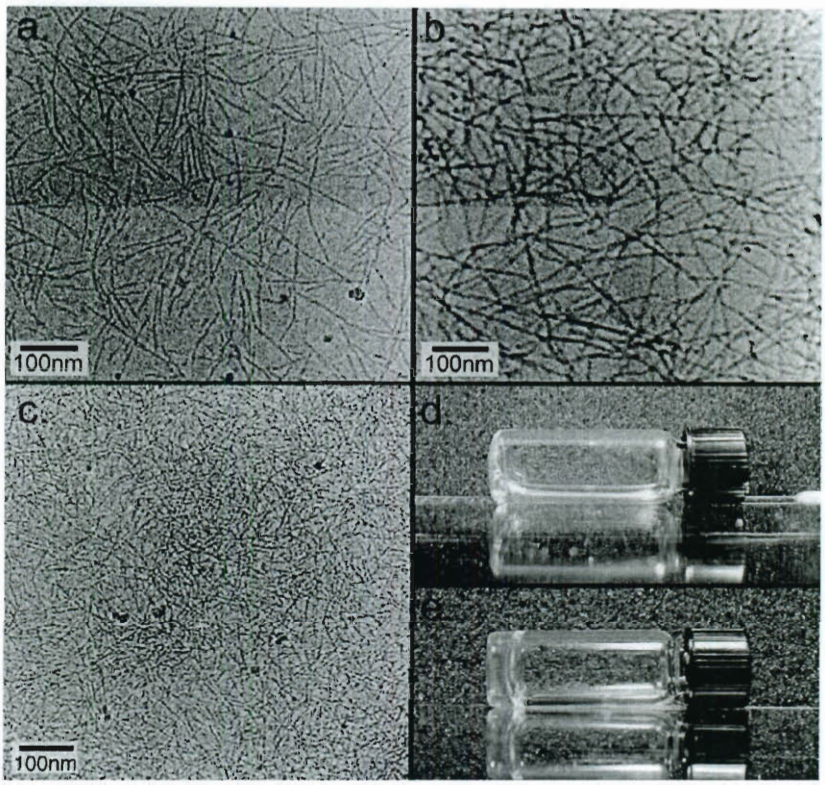

Figure 2.5. a) $K_2(QL)_6K_2$ at 1 wt % in the presence of 150 mM NaCl and 10 mM Tris. b) $K_2(QL)_6K_2$ at 1 wt % in the presence of 1 M NaCl and 10 mM Tris. c) Cryo-TEM image of peptide $K_2(QL)_6K_2$ at 1 wt % concentration and at pH 12. The formation of dense network of long fibers can be seen. d) $K_2(QL)_6K_2$ at 1 wt % in 10 mM Tris at pH 7. e) $K_2(QL)_6K_2$ at 1 wt % in 150 mM NaCl and 10 mM PO_4.

This peptide was further characterized using atomic force microscopy (AFM), which showed fiber heights of approximately 2 nm (Figures 2.6 and 2.7). A molecular model was constructed, which predicts fiber diameters of 5.4 nm and fiber heights of 1.98 nm. This model assumes a polyproline type II conformation for the charged lysine residues and an extended beta sheet conformation for (QL) repeating units. The experimental data appear to be in good agreement with the constructed model, indicating that self-assembly is proceeding in this system as expected. This peptide was later characterized by scanning electron microscopy, which confirmed the presence of a dense fibrous network under charge-screening conditions.

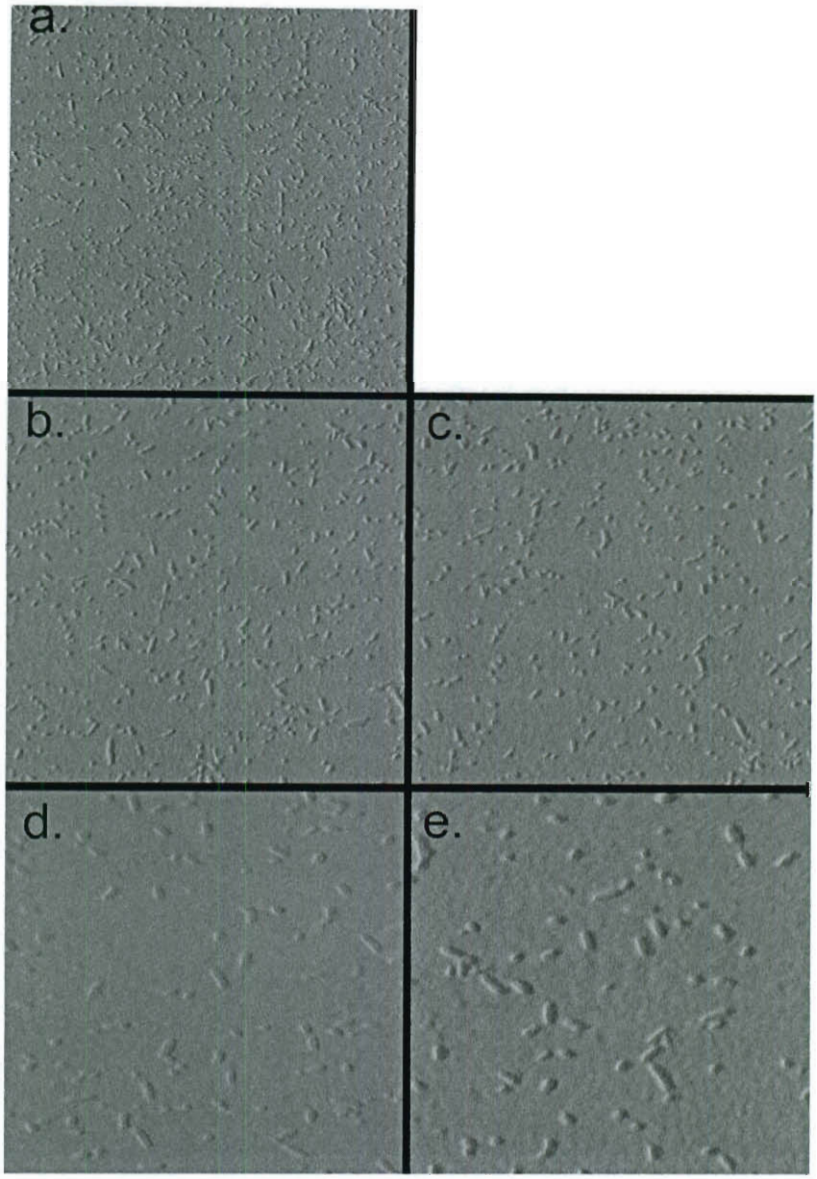

Figure 2.6. Amplitude Tapping Mode AFM images of $K_2(QL)_6K_2$ fibers deposited onto cleaved mica from a 0.01% by weight solution. a) depicts a 3 μm x 3 μm image. b) and c) depict 2 μm x 2 μm images, while d) and e) depict 1 μm x 1 μm images.

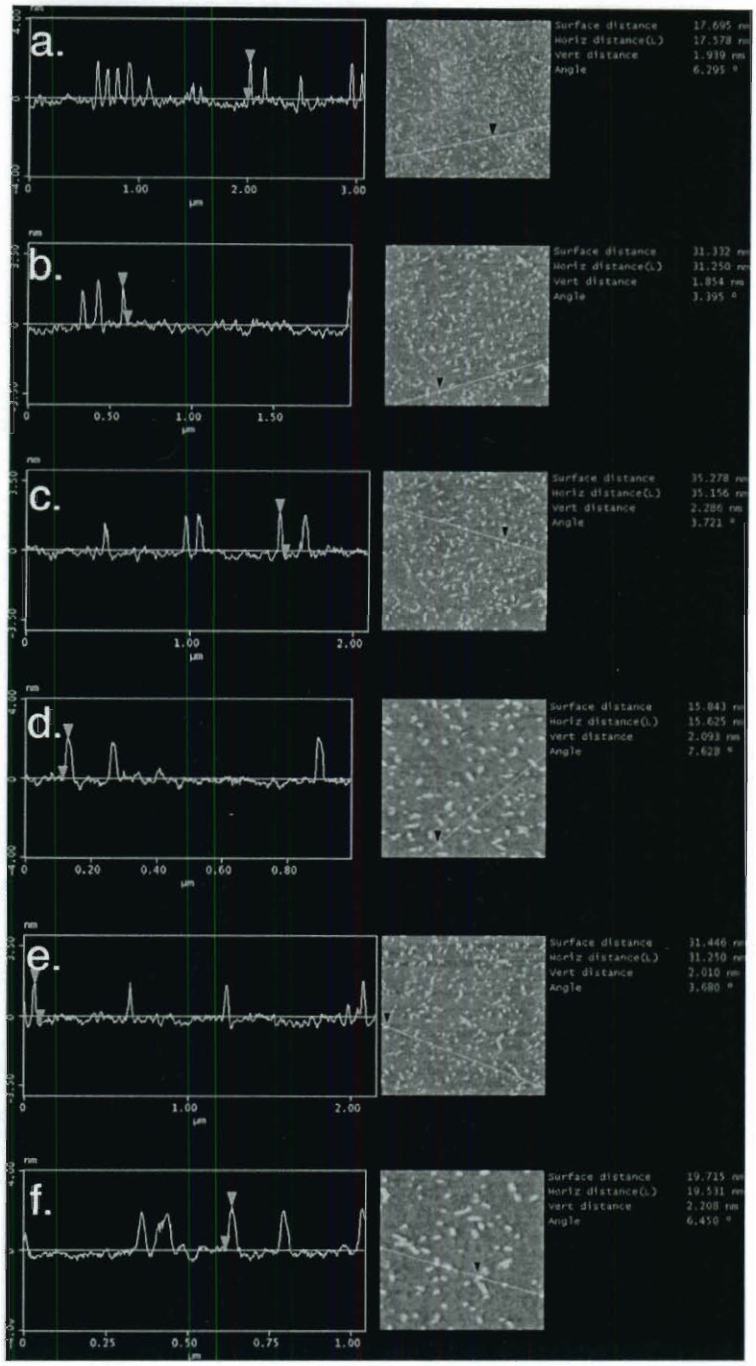

Figure 2.7. Height analysis of $K_2(QL)_6K_2$ fibers deposited onto cleaved mica from a 0.01% by weight solution. Fibers showed heights varying from 1.85 nm to 2.29 nm, which is consistent the predicted height of 1.98 nm. Amplitude image in figure 2.6.a corresponds to height image 2.7.a. Amplitude image in figure 2.6.b corresponds to height image 2.7.b and c. Amplitude image in figure 2.6.c corresponds to height image 2.7.e. Amplitude image in figure 2.6.d corresponds to height image 2.7.d. Amplitude image in figure 2.6.e corresponds to height image 2.7.f.

When the charges on lysine residues are screened by multivalent ions such as phosphate, a clear hydrogel is formed. Phosphate ions serve to physically crosslink the lysine residues, as multiple lysines can undergo charge screening by a single phosphate ion. These hydrogels are weak upon formation and appear to strength over time, reaching an elastic modulus of 95 Pascals (Figure 2.8) when the peptide is screened in a phosphate buffer. This observation was investigated by cryo-TEM, and it was found that over time, the fibers appeared to undergo a lengthening process (Figure 2.9). During this aging, the maximum fiber lengths do not change. However, the average lengths increased, owing to the disappearance of shorter fibers.

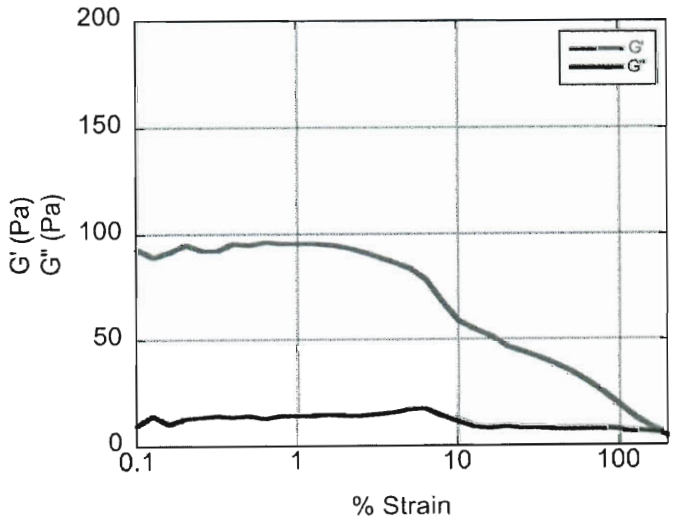

Figure 2.8. Strain sweep of a 1 wt% PO_4^- gel of $K_2(QL)_6K_2$. The elastic modulus (G') is shown in red and the loss modulus (G") is shown in blue.

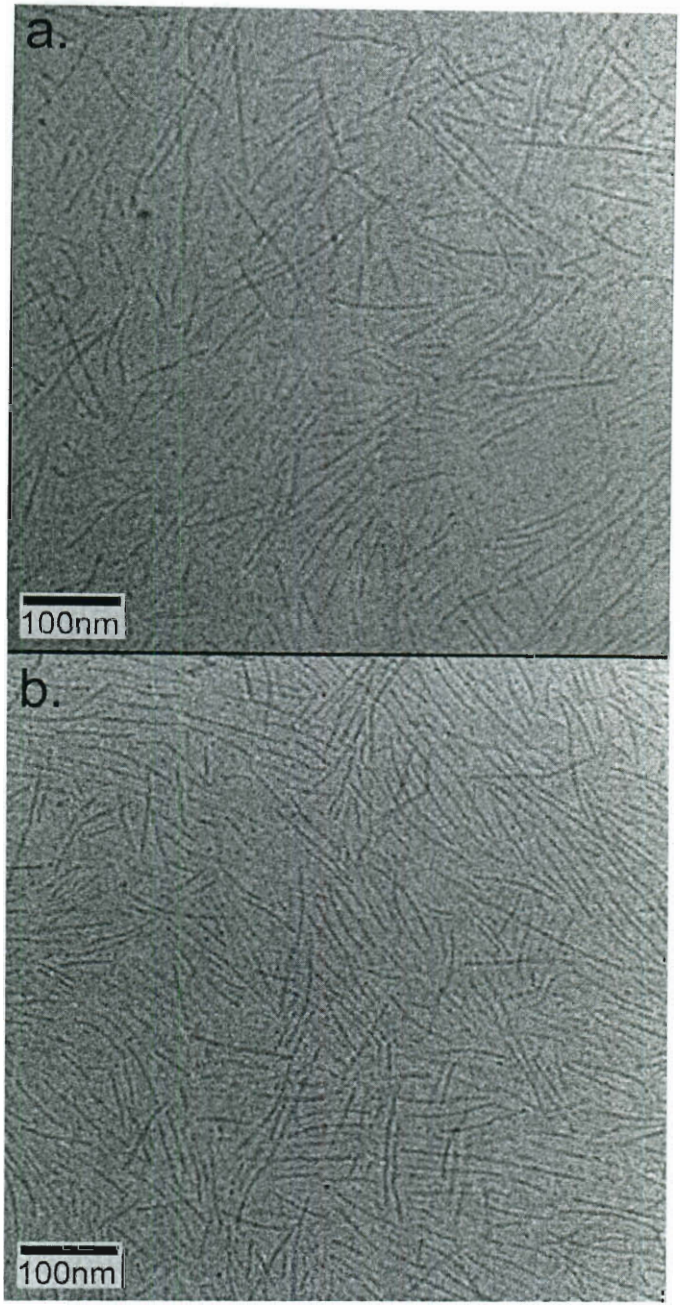

Figure 2.9. Aged samples of $K_2(QL)_6K_2$: a) 0.5% by weight b) 1% by weight. The image in panel a was prepared from a 1% by weight solution that was diluted 1:1 with 10 mM Tris buffer immediately before cryo-TEM sample preparation.

Analysis by dynamic light scattering (DLS) supports this finding. This "maturation" has been observed in other nanofiber systems as well[10] and indicates that the initially formed nanofiber structure is not the global thermodynamic minimum and

that the system is still moving toward equilibrium, which is composed of larger or bundled fibers.

B. Hydrophilic amino acid modification

Alteration of the hydrophilic amino acid in the central block provides the opportunity to manipulate the delicate balance of molecular forces governing the self-assembly of multidomain peptides. The most conservative substitution, a glutamine to asparagine substitution, results in the peptide $K_2(NL)_6K_2$, which forms nanofibers with similar morphology to $K_2(QL)_6K_2$ (Figure 2.10). Both glutamine and asparagine contain amide groups in their side chains and differ only by a single methylene group. Therefore, it is not surprising that self-assembly of the two systems proceeds in a similar manner.

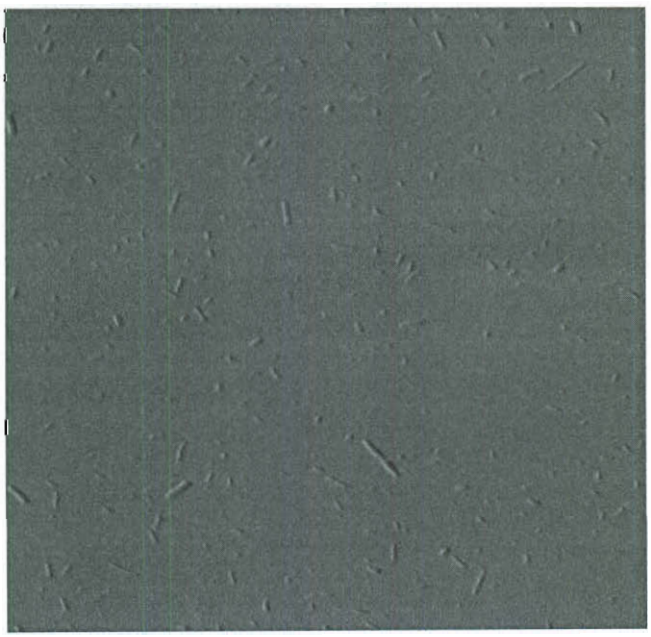

Figure 2.10. $K_2(NL)_6K_2$ forms short nanofibers as observed by AFM. Image shown is 2 μm x 2 μm.

Substitution of glutamine residues with another neutral alternative, serine, results in a different network of hydrogen bonding between peptide strands and between the nanofibers and the aqueous solvent.[9] $K_2(SL)_6K_2$ undergoes a greater extent of peptide self-assembly than $K_2(QL)_6K_2$ under identical conditions. $K_2(SL)_6K_2$ is clearly a beta sheet as seen by circular dichroism, with a clear maximum at 198 nm and minimum at 217 nm. FT-IR also indicates a beta sheet conformation (Figure 2.11).

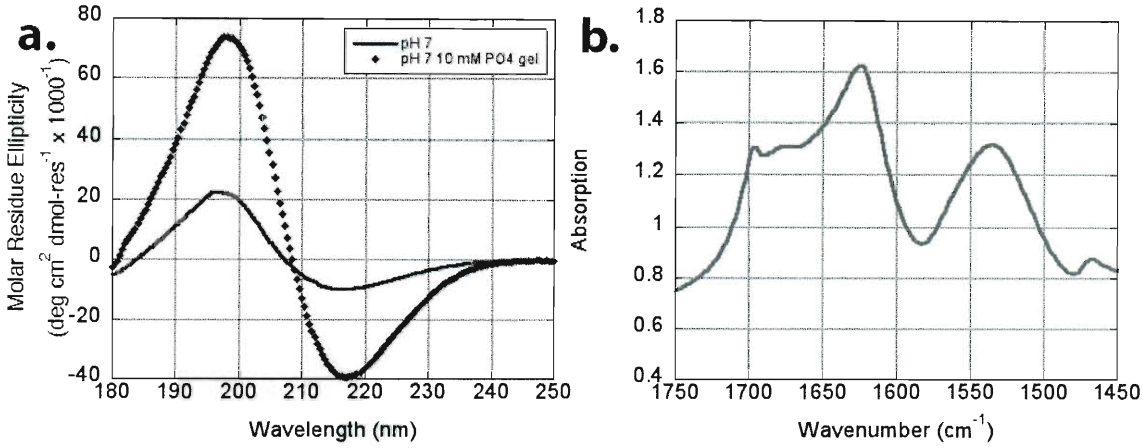

Figure 2.11. a) CD of $K_2(SL)_6K_2$. The green line indicates a 1 wt% pH 7 solution and the blue diamonds indicate a 1 wt% PO_4^- gel. b) FT-IR of $K_2(SL)_6K_2$.

Fiber lengths are also longer as observed by cryo-TEM. The fiber heights, however, appear to be smaller than in its glutamine counterpart, approximately 1.6 nm. This is reasonable, considering that the serine side chain is significantly smaller than the glutamine side chain. Perhaps the most striking differences between the two peptides, however, are not in the fiber morphology but in the rheological characteristics of the hydrogels. $K_2(SL)_6K_2$ forms a robust hydrogel nearly immediately upon contact with phosphate ions, while the $K_2(QL)_6K_2$ gel forms over the course of hours or even days. Likewise, the aging phenomenon observed in $K_2(QL)_6K_2$ is not noticeable in $K_2(SL)_6K_2$.

These observations indicate that the introduction of serine (and the resulting changes to the hydrogen bonding network) changes the kinetics of fiber formation. $K_2(SL)_6K_2$ forms a robust gel in both phosphate alone and in phosphate-buffered saline (PBS) with a G' of approximately 395 Pa in 10 mM phosphate (Figure 2.12).

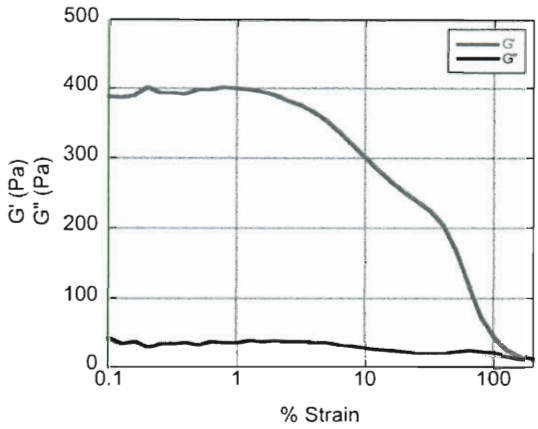

Figure 2.12. Strain sweep of a 1 wt% PO_4^- gel of $K_2(SL)_6K_2$. The elastic modulus (G') is shown in red and the loss modulus (G") is shown in blue.

The impressive rheological properties of $K_2(SL)_6K_2$, namely the high G' and ability to recover after shearing events, have made it an attractive system for biological applications, including drug and growth factor release.

The next logical modification is to replace serine residues with threonine residues, an amino acid that is similar to serine but features an additional methyl group. $K_2(TL)_6K_2$ shows a distinctive beta sheet structure in circular dichroism. However, in the absence of salts, nanofibers are not observed by AFM. Under typical gelation conditions (10 mM phosphate buffer), this peptide shows a G' of approximately 635 Pa. This indicates that the quality of hydrogen bonding between hydrophilic amino acids and between these residues and the solvent is crucial to the rheological properties of the gel.

C. Hydrophobic amino acid modification

It has been shown that the selection of hydrophilic residues within the central block of the peptide can have an enormous impact on the self-assembly processes at work. It was then investigated whether hydrophobic amino acid modification might also impact the self-assembly of multidomain peptides. In fact, the hydrophobic domain of the peptide offers the opportunity to introduce a new noncovalent interaction when aromatic amino acids are employed: π-π stacking. π-π stacking can occur when two aromatic amino acids reside in close proximity to one another, as might happen during hydrophobic packing in the center of a nanofiber. Therefore, the specific effects of aromatic amino acids on multidomain peptide self-assembly are of particular interest.

Synthetic peptides containing aromatic amino acids have been previously shown to have novel self-assembly properties.[11-15] The contribution of phenylalanine residues in particular is of interest because phenylalanine residues are prevalent in amyloid β, a protein that plays a crucial role in the development of Alzheimer's disease. Symptoms of Alzheimer's disease are correlated with soluble fibrils assembled from amyloid β.[16] In these structures, the individual beta sheet peptides (amyloid β or Aβ) assemble so that the peptide backbones are perpendicular to the fiber axis,[17] much like in our system. It has been determined that a short region of the amyloid β protein is essential for the nucleation of self-assembled amyloid β fibrils. This region includes residues Aβ 16-20, KLVFF. When added to Aβ *in vitro*, KLVFF exhibits strong binding to Aβ and is capable of preventing fibril formation.[18,19] The peptide FFKLVFF is also known to self-assemble in a beta sheet fashion to form amyloid fibers in methanol and

trifluoroethanol.[20] While the presence of phenylalanine in amyloid β appears to be crucial to fibril nucleation,[21] its exact contribution is still being investigated. Efforts to synthetically recreate amyloid β-like fibrils have lended support to the importance of phenylalanine in the fibril formation process.[13, 14, 22] Aromatic amino acids have been shown to encourage fibril nucleation in other natural systems as well, such as in type I collagen.[23] Elucidating the specific effects of aromatic amino acids on self-assembly in a more analogous system, a multidomain peptide system, may have important implications for the nucleation of amyloid β self-assembly as well. However, one problem that remains to be solved is whether the changes in self-assembly in systems incorporating aromatic amino acids are due to the aromaticity, hydrophobicity, or steric influence of these amino acids.

Here we examine the substitution of leucine residues of multidomain peptides with the aromatic residues phenylalanine, tyrosine, and tryptophan residues. Each substitution affects a noticeable impact on the morphology and rheology of peptide hydrogels formed by these peptides. The number and type of charged residues was kept constant to examine the effect of the hydrophobic amino acid alone.

1. Secondary Structure

The effect of the hydrophobic amino acid on the circular dichroism of these peptides is significant. While $K_2(QL)_6K_2$ shows a typical beta-sheet conformation via circular dichroism (CD), substitution of aromatic amino acids introduces new features into the CD spectra of these peptides (Figure 2.13). Each peptide was observed in both the gel

and non-gelled state, since the nature or extent of self-assembly may change in the presence of ions. Hydrogels were formed by dissolving lyophilized peptide at 2 wt% in ultrapure water and adding an equal volume of 20 mM phosphate buffer at pH 7. Solutions were mixed by careful pipetting, which resulted in a 1 wt% gel. Non-gelled peptides were dissolved at 1 wt% in ultrapure water and adjusted to pH 7. CD and IR spectra did not differ significantly between the non-gelled and gel states. $K_2(QF)_6K_2$ shows a distinct minimum in its CD spectrum at 200 nm, and the characteristic maximum has shifted from 200 nm to 191 nm. The minimum characteristic of beta sheets is still present but has shifted slightly to 214 nm. This minimum around 200-205 nm has been reported previously and is a result of aromatic-aromatic interactions.[13, 14, 24] However, the intensity of this minimum may introduce artifacts in that it may cause other maxima or minima to appear red- or blue-shifted even through a structural transition has not taken place. Other Phe-containing peptides have been shown to have anomalous CD spectra as well.[25] In fact, peptides displaying such unusual CD features are determined through other techniques to still have β-sheet characteristics.[13, 24] In order to ascertain the extent to which the phenylalanine residues actually disrupt the β-sheet structure, the peptide $K_2(QFQL)_3K_2$ was constructed. Designed to be an intermediate between $K_2(QL)_6K_2$ and $K_2(QF)_6K_2$, this peptide shows a clear β-sheet conformation via CD, with a maximum at 201 nm and a minimum at 220 nm, indicating that the simple presence of an aromatic amino acid in the sequence is insufficient to destroy β-sheet structure in this system. Thus, a structural transition has not taken place with the introduction of phenylalanine. In fact, when the hydrophobic amino acid is changed to a tyrosine or tryptophan, we see a return of a more typical β-sheet spectrum, and this minimum at 200 nm is not present,

although the peak shape of the maximum between 190 and 200 nm is clearly altered. Infrared (IR) spectroscopy of all peptides suggests β-sheet secondary structure. Therefore, aromatic amino acids in the central block of multidomain peptides make a significant contribution to their CD spectra but do not preclude β-sheet formation. It is suspected that the minimum at 200 nm distorts the spectrum but that the deviation from a beta sheet secondary structure may be minimal.

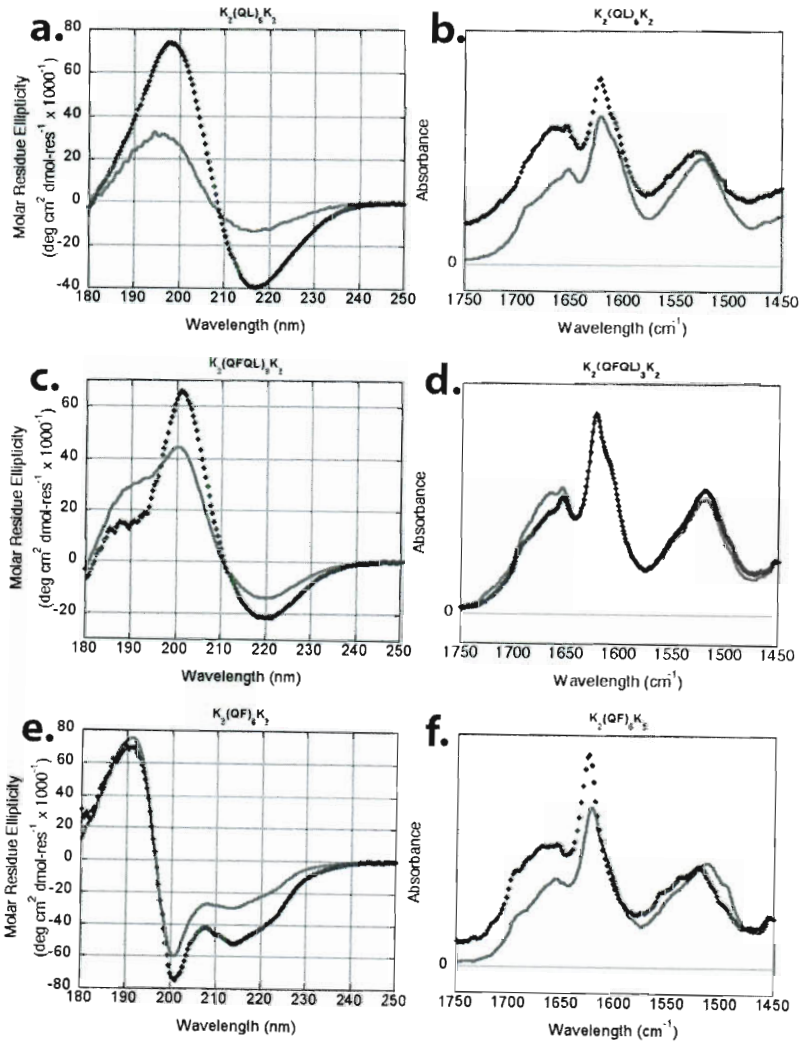

Figure 2.13. CD spectra and corresponding FT-IR of peptides incorporating varying amounts of phenylalanine. a, b) CD and IR of $K_2(QL)_6K_2$, c,d) CD and IR of $K_2(QFQL)_3K_2$, and e,f) CD and IR of $K_2(QF)_6K_2$. Red lines (—) indicate the solution state. Blue diamonds (◆) indicate the PO_4^- (a,c,e) or PBS (b,d,f) induced gelation state.

The tryptophan and tyrosine analogs of these peptides, $K_2(QW)_6K_2$ and $K_2(QY)_6K_2$, show a more typical beta sheet CD spectrum (Figure 2.14). Collectively, it can be concluded that multidomain peptides with the sequence $K_2(QX)_6K_2$, where X is an aromatic amino acid, have a predominantly beta sheet secondary structure. While peak shapes of these multidomain peptide spectra may be distorted, all peptides examined here except $K_2(QF)_6K_2$ display maxima and minima at the expected values for a beta sheet.

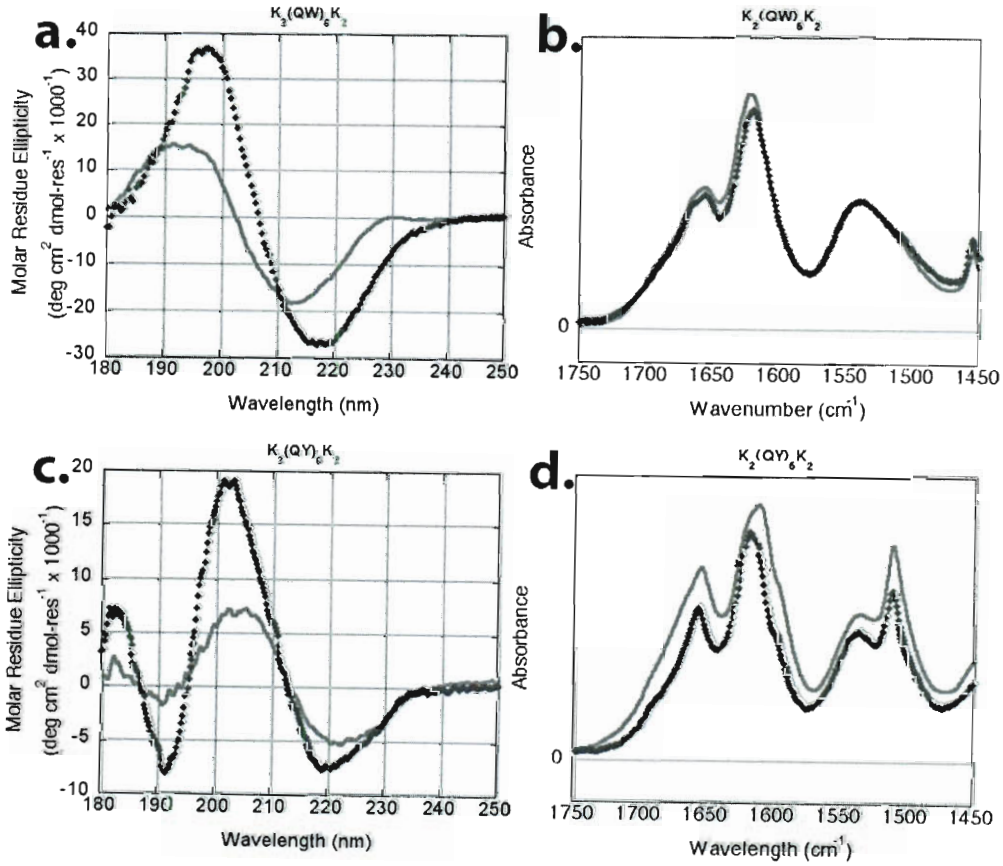

Figure 2.14. CD spectra and corresponding FT-IR of peptides incorporating tyrosine and tryptophan. a, b) CD and IR of $K_2(QW)_6K_2$, c,d) CD and IR of 5. Red lines (—) indicate the solution state. Blue diamonds (◆) indicate the PO_4^- (a,c) or PBS (b,d) induced gelation state.

Previous studies of multidomain peptides found the peptide strands within the nanofibers to be oriented antiparallel to one another. Grazing angle IR experiments were performed in order to determine the preferred orientation of hydrogen bonding within the nanofiber.[26] In this set of experiments, an IR spectrum of the peptide sample on a CaF_2 window is taken, with the beam perpendicular to the sample. This is compared to a second sample, which is dried onto a gold mirror that is placed nearly parallel to the beam. Because the IR beam is oriented differently relative to the sample in both cases, the two sets of spectra can reveal information related to directional interactions within the peptide nanostructure.[26, 27] A peak at 1695 cm^{-1} in the grazing angle spectrum is characteristic of an antiparallel beta sheet. This peak is present in grazing angle spectra for $K_2(QL)_6K_2$, $K_2(QFQL)_3K_2$, and $K_2(QF)_6K_2$ (Figure 2.15). However, no obvious peak is visible for peptides $K_2(QW)_6K_2$ or $K_2(QY)_6K_2$. Therefore, it is possible that $K_2(QW)_6K_2$ and $K_2(QY)_6K_2$ adopt a parallel beta sheet conformation, while $K_2(QL)_6K_2$, $K_2(QFQL)_3K_2$, and $K_2(QF)_6K_2$ reside preferentially in an antiparallel orientation. Modeling simulations are currently being undertaken to investigate the preferred packing nature of each of these peptides.

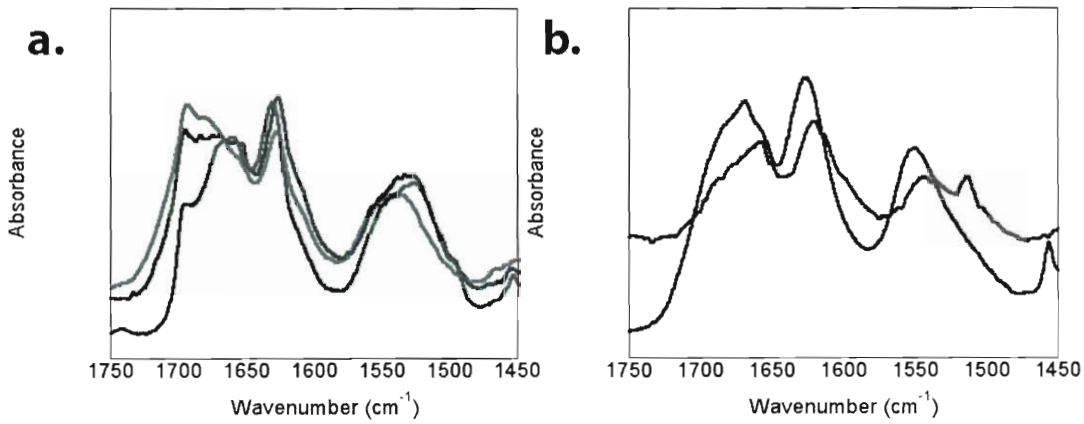

Figure 2.15. Grazing angle IR spectra of a) $K_2(QL)6K_2$ (red), $K_2(QFQL)_3K_2$ (blue), and $K_2(QF)_6K_2$ (green). Note the presence of a distinctive peak between 1690 and 1700 cm^{-1}. b) $K_2(QW)_6K_2$ (blue) and $K_2(QY)_6K_2$ (green).

2. Nanofiber morphology

Fiber network morphology was examined for all peptides in both the gelled and non-gelled states. Gelation conditions were achieved by the addition of charge-screening salts. For a peptide with positively charged lysine residues on the termini, a negatively charged multivalent salt, such as phosphate, is required. Use of a multivalent rather than a monovalent salt allows phosphate ions to physically cross-link peptides to one another, leading to gel formation. For the non-gelled state, AFM and vitreous ice cryo-transmission electrom microscopy (cryo-TEM) were used to visualize nanofiber morphology (Figure 2.16). For the gelled state, cryo-TEM and SEM were employed for this purpose (Figure 2.17). $K_2(QL)_6K_2$ self-assembles into linear nanofibers that are 6 nm in width, 2 nm in height, and several hundred nanometers in length, as determined by cryo-TEM and AFM. SEM confirms the presence of a nanofiber network in the gelled state. The introduction of three phenylalanine residues, as in $K_2(QFQL)_3K_2$, results in

conservation of nanofiber formation. Nanofibers of this peptide appear linear and unbranched by cryo-TEM and AFM. SEM on a critical point dried gel reveals a spongy nanofiber network. However, the presence of six phenylalanine residues, $K_2(QF)_6K_2$, results in very fragile fibers that are only briefly visible during imaging via electron microscopy. Spherical aggregates are visible via cryo-TEM in the non-gel state, along with some isolated short fibers. AFM supports this observation, showing the presence of spherical aggregates in the non-gel state. Fibers in the absence of ions were obtainable using these two methods. However, cryo-TEM of the peptide gel did show nanofibers. SEM of this peptide proved difficult, with fiber samples rapidly decaying under the electron beam, but fiber morphology in these gels was still observed. Interestingly, concentration dependent polymorphism of a similar phenylalanine-containing peptide has been reported previously,[13] which is in agreement with our observations. $K_2(QW)_6K_2$ and $K_2(QY)_6K_2$ exhibit less fragility than the phenylalanine analog but have very different morphologies: $K_2(QW)_6K_2$ results in linear fibers via both cryo-TEM and AFM, while $K_2(QY)_6K_2$ shows fiber branching by both methods.

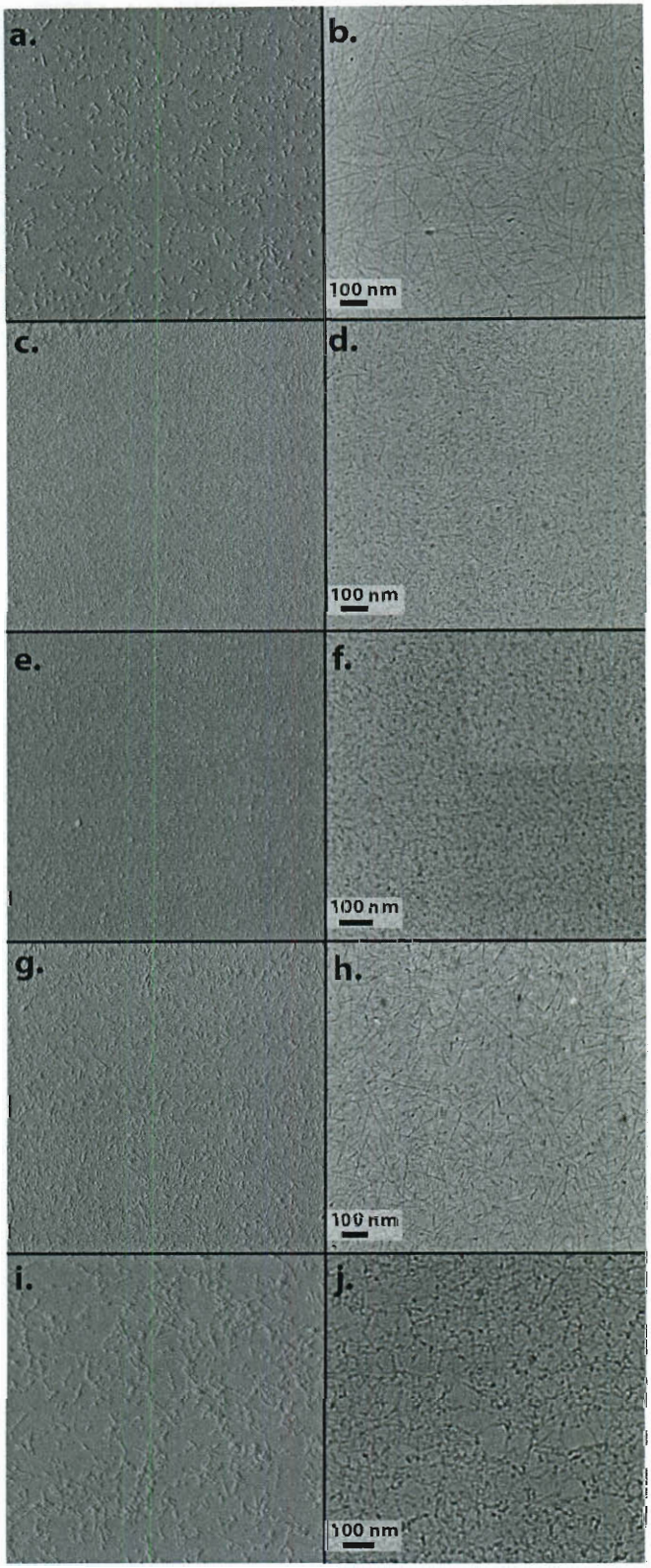

Figure 2.16. AFM and cryo-TEM of peptides in the non-gelled state. a, b) $K_2(QL)_6K_2$, c, d) $K_2(QFQL)_3K_2$, e, f) $K_2(QF)_6K_2$, g, h) $K_2(QW)_6K_2$, i, j) $K_2(QY)_6K_2$.

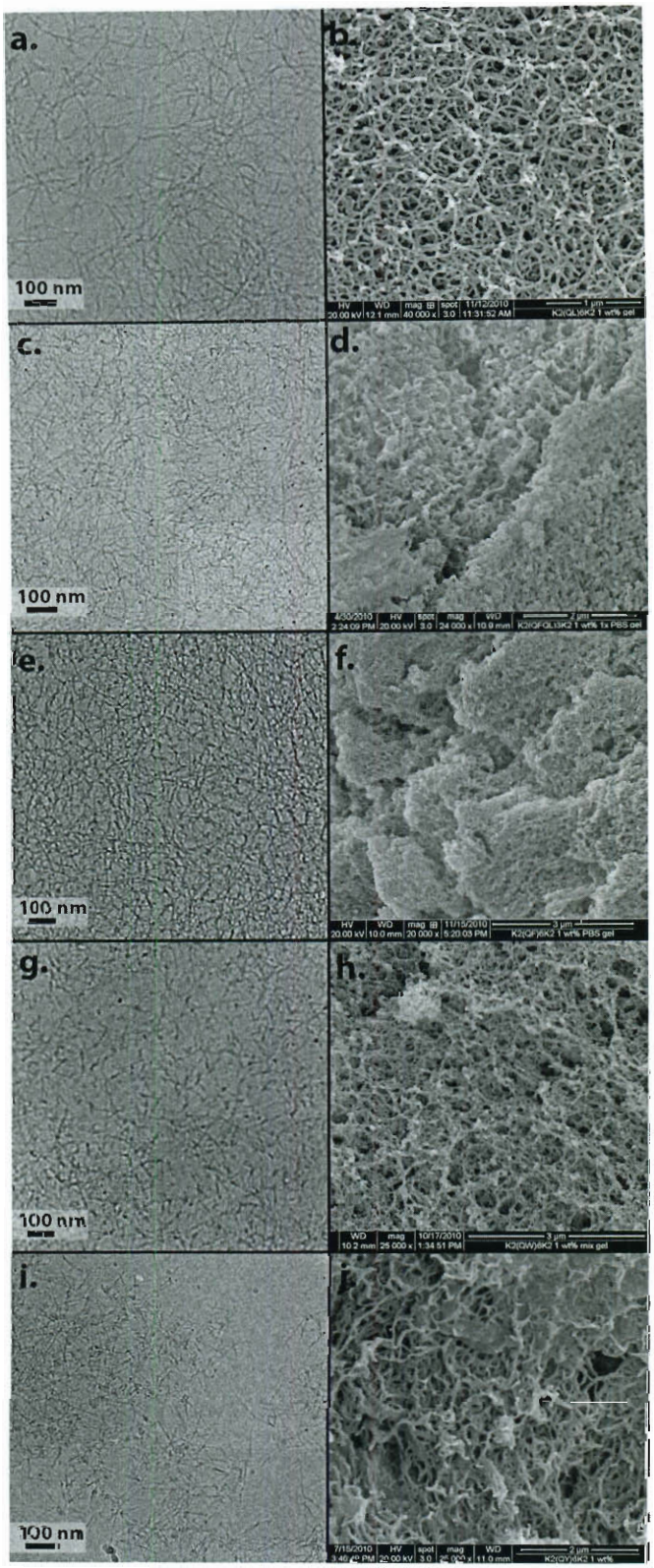

Figure 2.17. Cryo-TEM and SEM of peptides in the gelled state (PBS). a, b) $K_2(QL)_6K_2$, c, d) $K_2(QFQL)_3K_2$, e, f) $K_2(QF)_6K_2$, g, h) $K_2(QW)_6K_2$, i, j) $K_2(QY)_6K_2$.

3. Rheology

Hydrogels of each peptide were prepared by dissolving the peptide at 2 wt% in ultrapure water at pH 7. To this solution was added an identical volume of 2x phosphate buffered saline (PBS) at pH 7. The solution was pipetted up and down several times before the vial was capped and vortexed for several seconds. The gels were stored in airtight vials until rheometry was performed. Gels were examined by a strain sweep at a constant frequency of 1 rad/sec (Figure 2.18), as well as a shear recovery experiment. In the recovery experiment, gels were held at a low degree of strain for 10 minutes, then sheared at 100% strain for 1 minute, and subsequently returned to the low strain condition for an additional 20 minutes. Of the aromatic amino acid-containing peptides, $K_2(QF)_6K_2$ showed the highest elastic modulus (G') values. $K_2(QFQL)_3K_2$ and $K_2(QW)_6K_2$ also form rigid hydrogels. Interestingly, $K_2(QY)_6K_2$ only forms a weak, unstable gel that phase separates with time. This gel is opaque rather than transparent, even immediately following gel formation. It is thought that the hydroxyl group present on the tyrosine residues may disrupt the largely hydrophobic environment in the interior of the nanofibers. This is supported by the fact that $K_2(QY)_6K_2$ is the least soluble of the peptides tested (though it is soluble at 1 wt% at pH 7). It is interesting that while the presence of nanofibers is often correlated with hydrogel formation in many peptide systems, this correlation is not clear for multidomain peptides, as $K_2(QF)_6K_2$ forms a gel but shows poor fiber formation, while $K_2(QY)_6K_2$ consistently forms fibers but does not form a strong gel. The reason for the lack of gel formation in $K_2(QY)_6K_2$ is unclear.

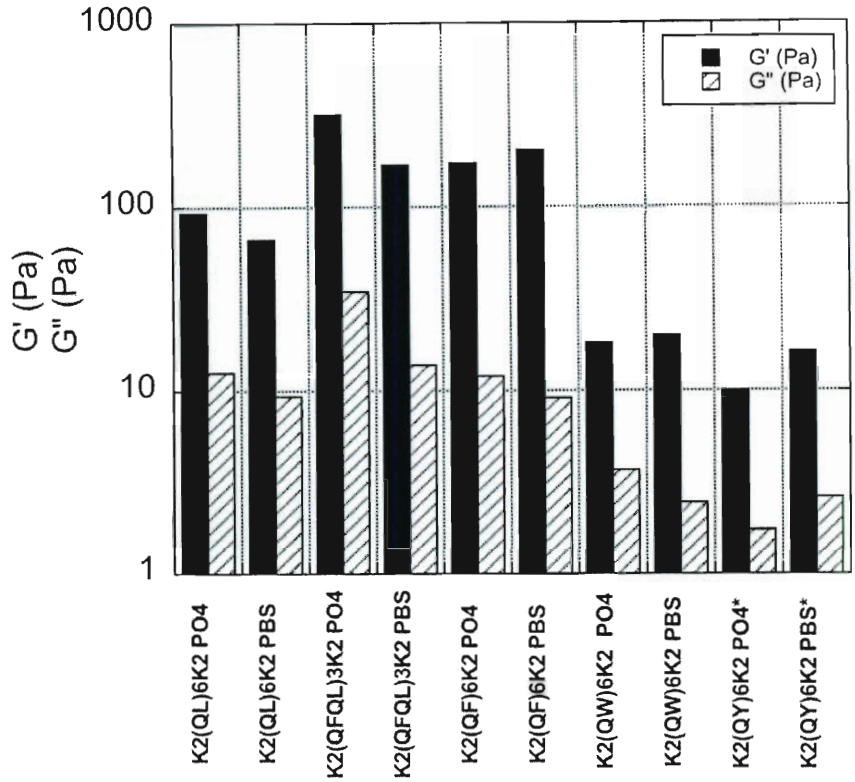

Figure 2.18. Strain sweep of $K_2(QX)_6K_2$ phosphate and PBS gels. Phosphate gels were made using 10 mM phosphate buffer at pH 7.4, and PBS gels were made using PBS at pH 7. Asterisks indicate a peptide hydrogel that is not time-persistent.

4. Aromatic Character Impacts Self-Assembly

Bowerman and colleagues determined that it is largely hydrophobicity, and not aromaticity, that drives the self-assembly of beta sheet forming peptides into amyloid-like nanofibers[13]. However, the modular nature of multidomain peptides allows us to explore the aromatic contribution to self-assembly by keeping all other blocks of the peptide constant. When the charged and hydrophilic residues are held constant, substitution of aromatic amino acids for hydrophobic leucine residues has a huge impact on fiber

morphology and rheology. Hydrophobicity alone cannot account for these differences,[28] as leucine and phenylalanine have similar hydropathy indices but produce vastly different fiber morphologies. Similarly, tyrosine and tryptophan have similar hydropathy indices but different fiber morphologies. However, several trends are noticeable. A multidomain peptide with exclusively leucines in the hydrophobic positions forms uniform, linear fibers. As the number of phenylalanines introduced increases, the less linear (and more disordered) the fibers become. $K_2(QFQL)_3K_2$ demonstrates a consistently linear fiber network as observed by cryo-TEM. Thus, the presence of phenylalanine is not sufficient to control fiber morphology. However, $K_2(QF)_6K_2$ forms a highly branched network under gelation conditions and only spherical aggregates in the solution state. This represents a large deviation from the gelation behavior and fiber morphology of $K_2(QL)_6K_2$ and $K_2(QFQL)_3K_2$. This highly disordered fiber network is also characteristic of gels constructed from $K_2(QY)_6K_2$. This would suggest that as the aromatic character of the fiber interior increases, the less ordered and more branched the nanofiber network becomes. There is one caveat, however: $K_2(QW)_6K_2$ forms extremely linear fibers in the solution state and somewhat linear fibers under gelation conditions. It has been shown previously that tryptophan-tryptophan interactions within a beta hairpin structure promote stable nanostructures and that the tryptophan residues within these nanostructures reside in an edge-to-face conformation.[29] Either the additional steric bulk or the increased aromatic character of tryptophan as compared to the other amino acids has changed the preferred packing of peptides within the fibers, resulting in stable, linear fibers. However, this renders $K_2(QW)_6K_2$ different from all other exclusively aromatic multidomain peptide analogs, and the reasons for this are still under investigation.

D. Conclusions

The assembly of multidomain peptides into organized fibers can be attributed primarily to three types of interactions. First, hydrophobic packing of leucine side chains is the primary thermodynamic driving force for assembly in water, but does not provide control over shape or structure. Second, backbone β-sheet hydrogen bonding also contributes to the stability of the assembly but is more important in directing the anisotropy of the structure. Third, these forces are opposed by electrostatic repulsion between lysine side chains. As one changes the ratio between the number of hydrophobic residues and charged residues one may shift the equilibrium toward either self-assembly or disassembly. Therefore, fabrication of nanofibers with controlled-length becomes possible when the driving force of the self-assembly of (QL) subunits and opposing charge repulsion forces are balanced. On the basis of these results, when the number of lysine residues on each terminus is 2, the presence of 5 or more (QL) repeats results in controlled self-assembly to form nanofibers.

Modification of both the hydrophilic and hydrophobic amino acids is possible and has been investigated. Substitution of glutamine with asparagine or serine preserves the ability of the peptides to form fibers. Peptides containing serine as the hydrophilic amino acid also formed excellent hydrogels with an elastic modulus approximately four times higher than that for the glutamine analog hydrogel. This is an indication of a change in the magnitude or type of hydrogen bonding taking place along the length of the fibers.

Substitution of the hydrophobic leucine residue with aromatic amino acids leads to interesting changes if nanofiber morphology and gel rheology. The introduction of

phenylalanine is correlated with artifacts in the CD spectra, although it is thought that peptide folding does not deviate significantly from a beta sheet conformation. While the presence of phenylalanine does not preclude beta sheet formation, phenylalanine multidomain peptide analogs possess unexpected nanofibers morphologies that may be a result of an altered self-assembly process. Furthermore, while previous studies have shown that hydrophobicity is the driving factor in the formation of nanofibers with a hydrophobic core,[13] there seems to be no correlation between the hydrophobicity of the aromatic amino acid side chain and nanofiber morphology. The lack of consistent trends within this family of aromatic multidomain peptides suggests that another factor, such as the steric demands imposed by bulky amino acids such as phenylalanine and tryptophan, is also exerting influence over the self-assembly process and the resulting fiber morphologies.

E. Experimental

Peptide Synthesis and Purification. The syntheses of the peptides were carried out on an Advanced Chem Tech Apex 396 peptide synthesizer using general procedures for Fmoc solid phase chemistry with HBTU, HoBt and DIEA as coupling reagents based on a 0.15 mmol scale. A Rink Amide was used to generate an amide group on the C-terminus of the peptide. After completion of the peptide synthesis, the N-termini of peptides were acetylated in the presence of excess acetic anhydride and 0.9 mmol of DIEA in DCM. Peptides containing QL repeats were then cleaved and deprotected with a mixture of TFA/ triisopropanolsilane /water/anisole (18: 0.7 : 0.7 : 0.7 by volume) for 3-4

hours. Peptides containing SL repeats were cleaved with a mixture of TFA/triisopropylsilane/water/anisole/EDT (18: 0.5 : 0.5 : 0.5 : 0.5 by volume) for 3-4 hours. After rotary evaporation, the residual TFA solution was triturated with cold diethyl ether and dried under vacuum for 24 hours before further purification.

Mass spectrometry. A mass spectrum of the crude peptide product was obtained following each synthesis. This was performed on a Bruker Autoflex mass spectrometer in positive ion mode. Spectra were processed using FlexAnalysis software.

Peptide Purification. Purification was done on a Varian PrepStar220 HPLC using a preparative reverse phase C-18 column with a linear water/acetonitrile gradient (each containing 0.05% TFA) at a flow rate of 14 mL/min. The UV absorption of the eluents was monitored at 230nm. In the event of a single product in the crude product (as observed by mass spectrometry), purification was achieved by dissolving the peptide at 10 mg/mL in ultrapure water, followed by pH adjustment with NaOH to achieve a pH of 7. The peptide solution was then dialyzed through a SpectraPor dialysis membrane for 48-72 hours. During this time the water was changed ~ 2 times per day. The solution containing the peptide was frozen and then lyophilized to collect the pure peptide.

Circular Dichroism Measurements. CD spectra were recorded on a Jasco-J810 spectropolarimeter using quartz cells with path lengths varying from 0.01 cm to 0.001 cm. Spectra were collected at 25°C from 250 nm to 180 nm with a 0.2 nm interval at a rate of 50 nm/min. Millidegrees of rotation were converted to mean residual ellipticity.

FTIR measurements. Aliquots of peptide sample were pipetted onto a CaF_2 window or gold mirror and dried under nitrogen. Grazing angle FT-IR spectra were recorded with a 80Spec specular reflectance accessory (PIKETechnologies). Both samples were then examined using a Jasco FTIR 660plus. Collected spectra were linear baseline corrected.

By changing the orientation of the incoming IR beam with respect to the peptide nanofibers, one can achieve enhancement / attenuation of one mode over the other, which allows us to discern the orientation of peptide backbone and the intermolecular hydrogen bonding with respect to the nanofiber network.[26] In the case of the grazing angle IR experiment, where the IR incoming beam is nearly parallel to the substrate surface the amide I (primarily a stretching of C=O) and NH stretching modes were attenuated relative to the amide II mode (in plane NH bending and CN stretching). In contrast, when the IR beam is perpendicular to the fibers as is the case when they are deposited on the CaF_2 window, the amide I band and NH stretching modes are enhanced relative to the amide II. This indicates that the hydrogen bonding is parallel to the nanofiber axis with peptide backbone running perpendicular to the fiber axis, which is described as a "cross-beta sheet" conformation. Also, the enhancement of amide I peak at 1692 cm-1 in grazing angle IR versus transmission IR clearly demonstrates the anti-parallel orientation of beta sheets.

Vitreous Ice Cryo-TEM. Vitreous ice cryo-TEM samples were prepared according to the general procedure published by Milligan *et. al*,[30] using a controlled environment vitrification system (Vitrobot, FEI). 3-6 μL of sample were pipetted onto a holey carbon

grid (Quantifoil R1.2/1.3) and gently blotted for 2 seconds resulting in a thin film on the surface of a carbon grid. The sample then was plunged into liquid ethane to vitrify the remaining water. The sample obtained was transferred on the cryoholder (Gatan 626DH) using a Gatan workstation and observed on the JEM 2010 microscope at –176 °C, equipped with CCD camera (Gatan 2x2K).

Atomic Force Microscopy. 10 μL of a 0.01 wt% solution of peptide at pH = 7 were dropped onto freshly cleaved mica while spinning on a Headway Research, Inc. Photo-resist spinner. The sample was spun for 10 minutes and then rinsed with deionized water for 1-2 seconds. The sample was spun for an additional 10 minutes and then stored at room temperature prior to imaging. AFM images were collected in air, at ambient temperature, on a Digital Instruments Nanoscope IIIa in tapping mode.

Rheometry. A TA Instruments AR-G2 rheometer was used to perform measurements on all peptides. A parallel plate geometry with 8 mm diameter and 250 μm gap was used for all experiments. The gels were placed carefully in the headspace with a spatula, and the geometry was then lowered to the preset gap. Oscillatory strain sweeps were performed at 25°C at a fixed angular velocity of 1 rad/s. Oscillatory frequency sweeps were performed at 25°C using a fixed strain of 0.5%.

References

(1) Hule, R. A.; Nagarkar, R. P.; Altunbas, A.; Ramay, H. R.; Branco, M. C.; Schneider, J. P.; Pochan, D. J. *Faraday Discuss.* **2008**, *139*, 251-264.

(2) Zhang, S. *Nature Biotechnology* **2003**, *21*, 1171-1178.

(3) Ellis-Behnke, R. G.; Liang, Y. X.; You, S. W.; Tay, D. K.; Zhang, S.; So, K. F.; Schneider, G. E. *Proc. Natl. Acad. Sci. U. S. A.* **2006**, *103*, 7530.

(4) Jung, J. P.; Jones, J. L.; Cronier, S. A.; Collier, J. H. *Biomaterials* **2008**, *29*, 2143-2151.

(5) Branco, M. C.; Schneider, J. P. *Acta Biomater.* **2009**, *5*, 817-831.

(6) Branco, M. C.; Pochan, D. J.; Wagner, N. J.; Schneider, J. P. *Biomaterials* **2009**, *30*, 1339-1347.

(7) Naigai, Y.; Unsworth, L. D.; Koutsopoulos, S.; Zhang, S. *J. Controlled Release* **2006**, *115*, 18-25.

(8) Dong, H.; Paramonov, S. E.; Aulisa, L.; Bakota, E. L.; Hartgerink, J. D. *J. Am. Chem. Soc.* **2007**, *129*, 12468-12472.

(9) Aulisa, L.; Dong, H.; Hartgerink, J. D. *Biomacromolecules* **2009**, *10*, 2694-2698.

(10) Pandya, M. J.; Spooner, G. M.; Sunde, M.; Thorpe, J. R.; Rodger, A.; Woolfson, D. N. *Biochemistry* **2000**, *39*, 8728-8734.

(11) Gupta, M.; Bagaria, A.; Mishra, A.; Mathur, P.; Basu, A.; Ramakumar, S.; Chauhan, V. S. *Adv. Mater.* **2007**, *19*, 858-861.

(12) Caplan, M. R.; Moore, P. N.; Zhang, S. G.; Kamm, R. D.; Lauffenburger, D. A. *Biomacromolecules* **2000**, *1*, 627-631.

(13) Bowerman, C. J.; Ryan, D. M.; Nissan, D. A.; Nilsson, B. L. *Mol. BioSyst.* **2009**, *5*, 1058-1069.

(14) Bowerman, C. J.; Nilsson, B. L. *J. Am. Chem. Soc.* **2010**, *132*, 9526-9527.

(15) Ma, M. L.; Kuang, Y.; Gao, Y.; Zhang, Y.; Gao, P.; Xu, B. *J. Am. Chem. Soc.* **2010**, *132*, 2719-2728.

(16) Pike, C. J.; Burdick, D.; Walencewicz, A. J.; Glabe, C. G.; Cotman, C. W. *J Neurosci.* **1993**, *13*, 1676-1687.

(17) Hamley, I. W. *Angew. Chem. Int. Ed.* **2007**, *46*, 8128-8147.

(18) Tjernberg, L. O.; Naslund, J.; Lindqvist, F.; Johansson, J.; Karlstrom, A. R.; Thyberg, J.; Terenius, L.; Nordstedt, C. *J. Biol. Chem.* **1996**, *271*, 8545-8548.

(19) Tjernberg, L. O.; Lilliehook, C.; Callaway, D. J. E.; Naslund, J.; Hahne, S.; Thyberg, J.; Terenius, L.; Nordstedt, C. *J. Biol. Chem.* **1997**, *272*, 12601-12605.

(20) Krysmann, M. J.; Castelletto, V.; Hamley, I. W. *Soft Matter* **2007**, *3*, 1401-1406.

(21) Makin, O. S.; Atkins, E.; Sikorski, P.; Johansson, J.; Serpell, L. C. *Proc. Natl. Acad. Sci. U. S. A.* **2005**, *102*, 315-320.

(22) Marini, D. M.; Hwang, W.; Lauffenburger, D. A.; Zhang, S. G.; Kamm, R. D. *Nano Lett.* **2002**, *2*, 295-299.

(23) Kar, K.; Ibrar, S.; Nanda, V.; Getz, T. M.; Kunapuli, S. P.; Brodsky, B. *Biochemistry* **2009**, *48*, 7959-7968.

(24) Wang, K.; Keasling, J. D.; Muller, S. J. *Int. J. Biol. Macromol.* **2005**, *36*, 232-240.

(25) Padmanabhan, S.; Marqusee, S.; Ridgeway, T.; Laue, T. M.; Baldwin, R. L. *Nature* **1990**, *344*, 268-270.

(26) Paramonov, S. E.; Jun, H. W.; Hartgerink, J. D. *J. Am. Chem. Soc.* **2006**, *128*, 7291-7298.

(27) Kim, H. S.; Hartgerink, J. D.; Ghadiri, M. R. *J. Am. Chem. Soc.* **1998**, *120*, 4417-4424.

(28) Kyte, J.; Doolittle, R. F. *J. Mol. Biol.* **1982**, *157*, 105-132.

(29) Wu, L.; McElheny, D.; Huang, R.; Keiderling, T. A. *Biochemistry* **2009**, *48*, 10362-10371.

(30) Milligan, R. A.; Flicker, P. F. *J. Cell Biol.* **1987**, *105*, 29-39.

Chapter 3: Covalent Modification of Multidomain Peptides

The rheological properties of any matrix, natural or synthetic, play a key role in determining the ease of handling of the material and, in some cases, the response of the cells in contact with the gel.[1-3] We have shown that careful amino acid selection can lead to different hydrogel properties in peptides. However, improvements in gel strength can be achieved not only through amino acid sequence modification, but also through covalent modifications of a multidomain peptide hydrogel network. These covalent modifications may be chemically or enzymatically derived. The most obvious choice for covalent chemical modification of peptides is the incorporation of cysteine residues, which may be cross-linked to form disulfide bonds under oxidizing conditions (Figure 3.1). While cysteine oxidation allowed the tuning of the storage modulus (G') from 100 to over 5000 Pa,[4] cysteine has proven particularly difficult to handle, as its oxidation state is challenging to control. Thus, an alternate method of oxidation was desired.

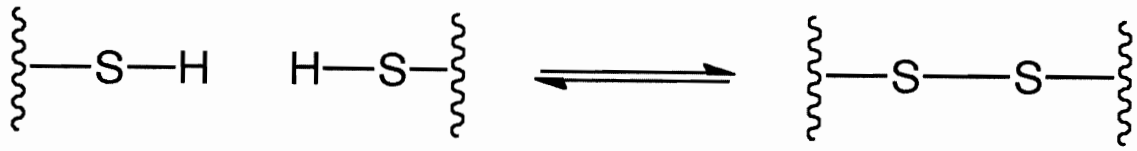

Figure 3.1. The oxidation of cysteine side chains to form a disulfide bond. Only the terminal –SH groups of the cysteines are shown.

A. Enzymatic Cross-linking*

The possibility of enzymatic cross-linking of residues within a peptide hydrogel solves many of the difficulties in handling introduced by cysteine, while simultaneously providing an option with a potential for high biocompatibility. In nature, components of extracellular matrix, such as collagen and elastin, are cross-linked by lysyl oxidase (LO), which oxidizes the primary amine of lysine to an aldehyde. This aldehyde can spontaneously react with another amine to form a Schiff base (Figure 3.2) or undergo an aldol condensation with another aldehyde.[5,6] Here we show that $K_2(SL)_6K_2$, which contains four lysine residues, is able to be cross-linked by either lysyl oxidase (naturally found in serum-supplemented medium) or plasma amine oxidase (PAO, a similar and commercially available enzyme which also functions by oxidation of primary amines). In either case, cross-linking results in a dramatically increased storage modulus over time.

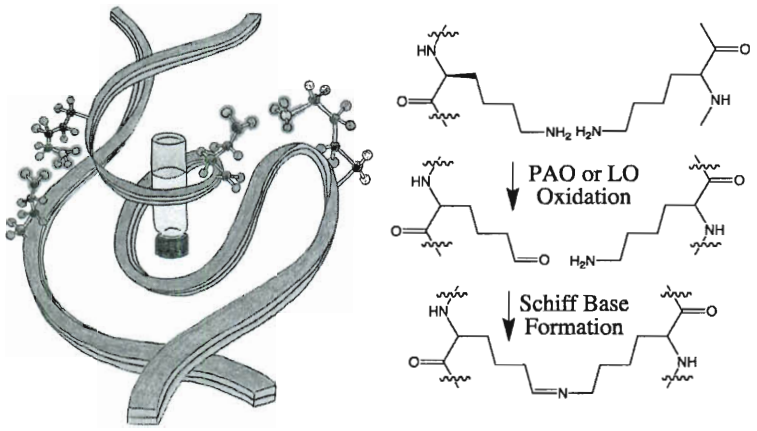

Figure 3.2. Proposed scheme of chemical cross-linking induced by lysyl oxidase or plasma amine oxidase.

---

* This section is based on: Erica L. Bakota, Lorenzo Aulisa, Kerstin M. Galler, and Jeffrey D. Hartgerink. Enzymatic Cross-Linking of a Nanofibrous Peptide Hydrogel. *Biomacromolecules*, **2011**, 12 (1), 82–87.

That $K_2(SL)_6K_2$ could be oxidatively cross-linked was a serendipitous discovery. As the biocompatibility of various MDP hydrogels was investigated, it became apparent that gels composed of $K_2(SL)_6K_2$ that were incubated with dental stem cells,[7] experienced a significant increase in storage modulus (G') over time. This study revealed that the G' increased over fourteen days of cell growth to ~6000 Pa (Figure 3.4a, blue bars). Histological sections of the cell / hydrogel composite indicated substantial production of natural extracellular matrix (data not shown). Based on these findings, we hypothesized that the newly synthesized ECM was responsible for the increase in mechanical properties, a phenomenon that had also been reported in the literature for similar systems.[8,9] In contrast, parallel experiments run with $E_2(SL)_6E_2$, which differs from $K_2(SL)_6K_2$ in that it uses the negatively charged amino acid glutamate in the peripheral region to control self-assembly rather than the positively charged amino acid lysine, were found to *decrease* in G' over time. In an attempt to understand the difference between these peptides further, a control experiment was run under identical conditions but without cells using $K_2(SL)_6K_2$. Surprisingly, gels prepared from $K_2(SL)_6K_2$ showed a similar increase in G' over time despite the absence of cells (Figure 3.4a, red bars). Clearly, production of extracellular matrix was not the cause of the G' increase. To identify the cause of this effect, $K_2(SL)_6K_2$ was incubated under several different conditions including: phosphate buffered saline (PBS), cell medium, cell medium enriched with Fetal Bovine Serum (FBS) and FBS alone (Figures 3.3a and b). In the absence of FBS, $K_2(SL)_6K_2$ did not display an increase in G'. However in the presence of FBS, G' increased dramatically. These experiments demonstrated that a component of the serum, and not production of ECM (or any other cellular component) was responsible for

the increase in G'. Unfortunately, fetal bovine serum contains a wide array of components and has been surprisingly poorly characterized. Additionally, the increase in G' did not take place with $E_2(SL)_6E_2$. Because the increase in G' was seen in only one multidomain peptide, and because FBS alone does not form hydrogels, it can be determined that it is the combination of a serum component *and* a multidomain peptide that together contribute to an increase in elastic modulus. Because the difference between the two peptides is the presence (or absence) of lysine, it can also be concluded that lysine is a required component of the peptide.

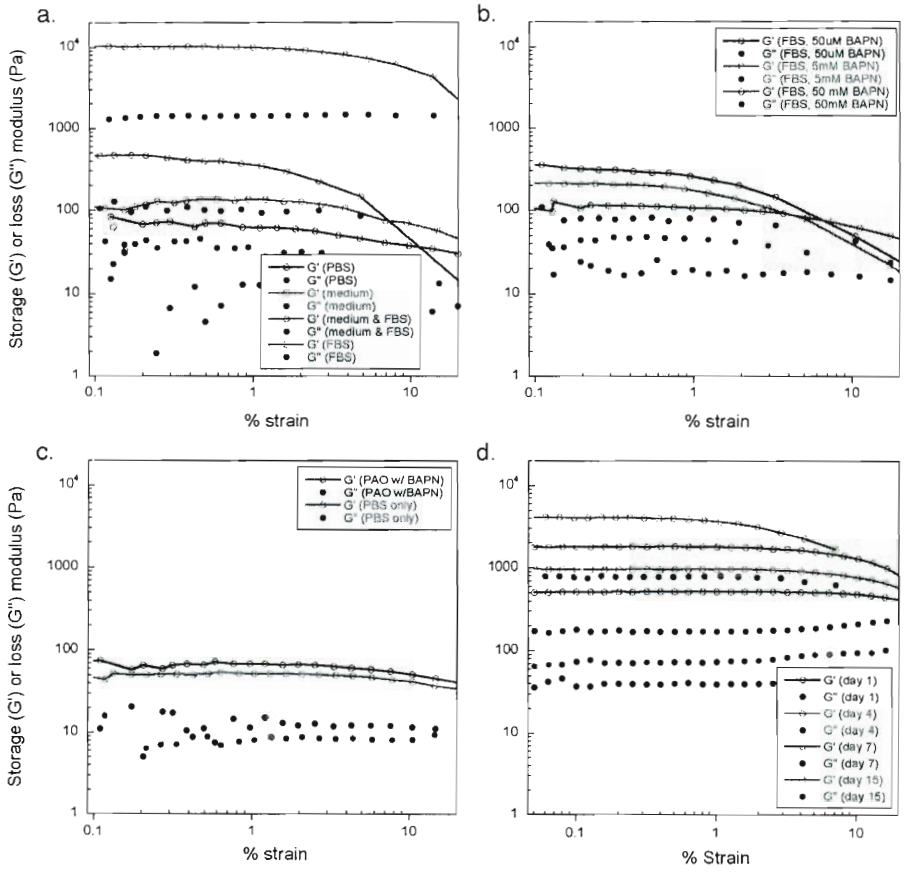

Figure 3.3. Strain sweeps of $K_2(SL)_6K_2$ under various medium compositions. a) no inhibitor after 10 days of treatment except FBS which is after 14 days treatment. b) after 10 days of treatment with FBS and indicated concentrations of βAPN. c) after 10 days of treatment with PBS only and after 10 days of treatment with PAO and βAPN. d) after 1, 4, 7 and 15 days treatment with PAO.

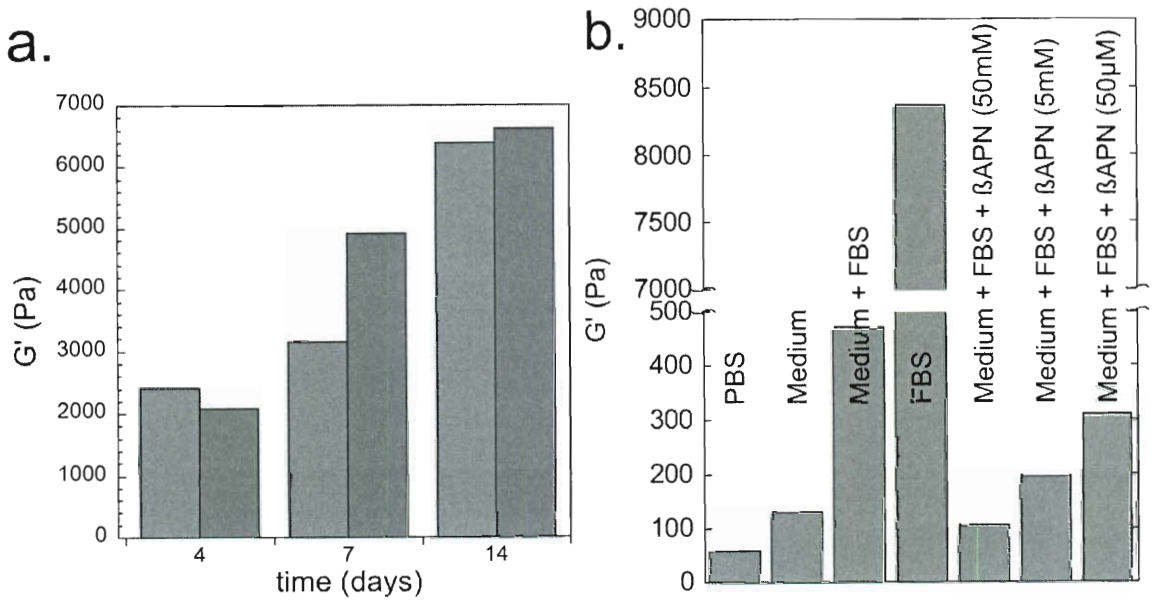

Figure 3.4. a) Storage modulus of $K_2(SL)_6K_2$ over 14 days with dental stem cells in presence of medium enriched with 10% FBS (blue) or medium enriched with 10% FBS with no cells (red). In all cases, one half the supernatant was refreshed every two days. b) $K_2(SL)_6K_2$ incubated under indicated conditions for 10 days without refreshing the supernatant.

In nature, lysyl oxidase is used to cross-link components of the extracellular matrix. Lysyl oxidase oxidizes the amine side chain of lysine to an aldehyde, which can then either react with an amine to form a Schiff base, or it can undergo an aldol condensation with another aldehyde, both of which result in the formation of a covalent cross-link between two previously separate residues (Figure 3.2).[5,6] Lysyl oxidase is also found in serum-supplemented cell culture media.[10] One way to determine if this oxidative cross-linking was taking place in our system is to inhibit lysyl oxidase, thereby preventing oxidative cross-linking, while simultaneously monitoring G'. For these experiments, an irreversible inhibitor of LO was chosen: β-aminopropionitrile (βAPN).[11] $K_2(SL)_6K_2$ was made into a gel using cell culture medium and FBS to which no inhibitor was added (control). Three additional gels were made utilizing medium and 10% FBS to which

different concentrations of βAPN were added as inhibitors and G' was monitored for 10 days. As shown in Figure 4.4b, 50mM βAPN results in a G' comparable to that of medium with no FBS. Lower concentrations of βAPN result in inhibition to a lesser degree. This strongly suggests that lysyl oxidase is the key component responsible for the change in rheological properties.

If oxidative cross-linking is indeed taking place, this process should be reproducible by the exogenous addition of enzyme in the absence of serum or cells. Thus, experiments were repeated without any fetal bovine serum or cell culture medium of any kind. As lysyl oxidase is not commercially available, plasma amine oxidase (PAO), an enzyme with a similar mechanism of action, was used.[12,13] Both lysyl oxidase and plasma amine oxidase fall into the same class of enzymes, the copper-containing amine oxidases (CuAOs). This class of enzyme is known to be involved in the development and maturation of the extracellular matrix and more specifically, collagen and elastin.[14] Hydrogels of $K_2(SL)_6K_2$ were treated with PAO (but no serum) and the G' monitored over 15 days. As was observed with serum treated gels, the G' increased dramatically over time. As with serum treated gels, addition of βAPN, which also inhibits PAO, resulted in the same lack of increase in the storage modulus indicating that cross-linking did not take place (Figure 3.5). Rheology has historically been used to estimate the degree of cross-linking in polymer systems where G is directly proportional to the degree of cross-linking. The clear increase in G' in the presence of active enzyme can be attributed to progressively higher degrees of cross-linking while the lack of increase in the presence of an enzyme inhibitor or in systems lacking the amino acid lysine indicates that no cross-linking is taking place.[14,15]

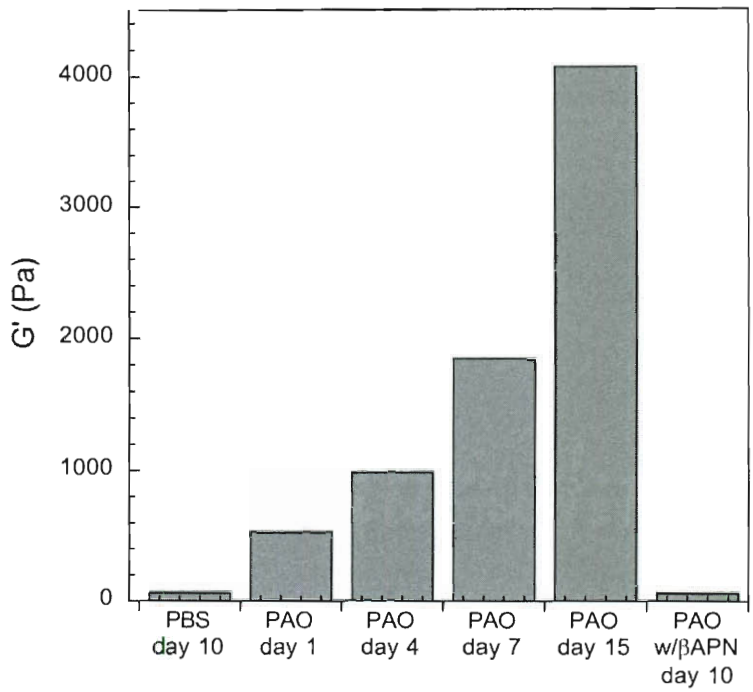

Figure 3.5. Storage modulus (G') without PAO, with PAO and with PAO plus βAPN as an inhibitor. The values of G' were chosen at an angular velocity of 0.5 rad/sec in the linear viscoelastic region.

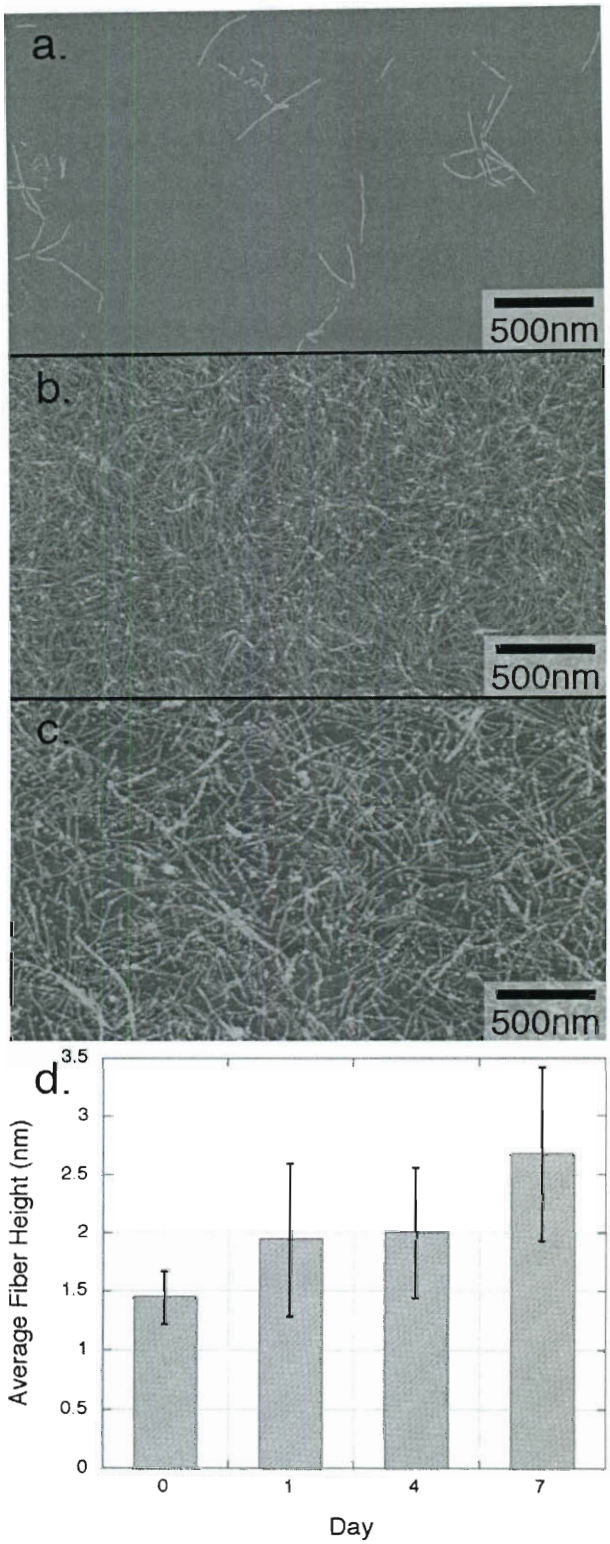

Figure 3.6. AFM of $K_2(SL)_6K_2$ nanofibers a) before gelation, b) after gelation but before treatment with PAO, c) after four days of treatment with PAO. d) Average height of fibers as measured by AFM.

AFM of $K_2(SL)_6K_2$ shows small, discrete self-assembled fibers prior to addition of phosphate buffer (Figure 3.6a). In the presence of phosphate these small fibers undergo further self-assembly in which they are physically cross-linked by the presence of phosphate (Figure 3.6b). Treatment with PAO results in the covalent capture of the gel network (Figure 3.6c). The introduction of covalent bonds between individual peptides results in some forced aggregation of peptide fibers that appears as fiber thickening. The general fibrous nature of the gel network, however, is preserved after treatment with the enzyme suggesting that the nanostructure is relatively unchanged. However, an increase in fiber height is observed over time, from approximately 1.6 nm at time zero to 2.7 nm after seven days of treatment with PAO (Figure 3.6d). This suggests fiber bundling occurs during oxidative cross-linking. The general fibrous nature of the gel network, however, is preserved after treatment with the enzyme suggesting that the nanostructure is relatively unchanged.

B. Conclusions

The results of this study have two important consequences. First, nanofibers formed from multidomain peptides that contain lysine will be oxidatively cross-linked in standard mammalian cell culture conditions (supplemented with FBS) this can have a desirable impact on the handling of the hydrogel as it becomes more robust with time rather than less robust. Additionally, studies that attribute improvements in mechanical properties of hydrogels to the production of ECM should first be careful to rule out covalent cross-linking of the matrix used. This covalent cross-linking in standard cell

culture conditions is possible without added enzymes, as lysyl oxidase is found in serum-supplemented media. Second, this study is a proof-of-principle that lysine oxidation using exogenous addition of plasma amine oxidase can be harnessed to cross-link self-assembled nanofibers. Enzymatic cross-linking via aldehyde formation and subsequent condensation represents a mild and simple method for increasing the mechanical strength of peptide hydrogels in applications for which the robustness of the gel is essential. This method should be suitable for a broad array of peptide hydrogels containing a high density of lysine such as those currently under study by many different groups.[16-19]

C. Experimental

Peptide Synthesis. Peptides were synthesized as previously described with the following changes: A Rink Amide MBHA low loading resin was used to generate a terminal amide. All amino acids and other reagents were dissolved in a mixture of 50% MDF (dimethylformamide) and 50% DMSO (dimethylsulfoxide). Amino acid coupling cycles were 60 min in length with the following proportions of reagents: 4 equivalents of amino acid, 4 equivalents of HATU (*O*- (7-azabenzotriazole-1-yl)-*N*,*N*,*N*,*N*'-tetramethyluronium hexafluorophosphate), and 6 equivalents of diisopropylethylamine for each equivalent of reactive site on the solid support. Fmoc (flourenylmethoxycarbonyl) was removed with two 7 min treatments of 20% piperidine, 2% DBU (1,8-diazabicyclo[5.4.0]-undec-7-ene), 39% DMF, and 39% DMSO by volume.

Preparation of Gels. Gels of $K_2(SL)_6K_2$ were prepared by dissolving lyophilized

powder in deionized water, followed by adjustment of the pH to approximately 7 by addition of NaOH. Deionized water was added to make a viscous solution with a concentration of 2% by weight. To this solution 2× PBS (phosphate buffered saline) was added in equal volume to make a final solution of peptide at 1% by weight, pH 7.4. The solution was vortexed thoroughly to ensure full mixing. The resulting gel was centrifuged to eliminate bubbles. Gels of $E_2(SL)_6E_2$ were prepared by dissolving lyophilized powder in deionized water followed by adjustment of the pH to approximately 7. Deionized water was added to make a viscous solution with final concentration of 2% by weight. To this solution, 4 mol equiv of aqueous $MgCl_2$ was added in equal volume to make a final solution of peptide at 1% by weight. The solution was vortexed thoroughly to ensure full mixing. The resulting gel was centrifuged to eliminate bubbles.

Time Course Oxidation. A total of 100 μL of MDP gel was pipetted into individual wells of a 96-well plate. To the top of these gels was added 200 μL of test solution. The test solution compositions included (1) PBS (phosphate buffered saline: 10 mM phosphate, 150 mM NaCl, pH 7.4), (2) medium (R-MEM, 50 μg/mL L-ascorbic acid 2-phosphate, 100 U/mL penicillin, and 100 μg/ mL streptomycin), (3) 10% FBS in medium (R-MEM supplemented with 10% fetal bovine serum, 50 μg/mL L-ascorbic acid 2-phosphate, 100 U/mL penicillin, and 100 μg/mL streptomycin), (4) 10% FBS in medium (as above) supplemented with 0.05, 5, or 50 mM APN as inhibitor, (5) 10% FBS in medium (as above) with SHED (mesenchymal stem cells from human exfoliated deciduous teeth) cells, and (6) 100% FBS. In addition, there were two conditions that contained no FBS or cell culture medium of any kind: (7) 3 nM plasma amine oxidase in

PBS and (8) 3 nM plasma amine oxidase in PBS supplemented with 50 mM βAPN as inhibitor. The plate was incubated at 37 °C for the requisite amount of time. One-half of the supernatant was refreshed every second day. Gels were carefully transferred to the rheometer at the desired time point with a spatula, taking care not to damage the gel during handling. Gels were not pipetted because the shear-thinning induced by this method would produce a measurable decrease in the elastic modulus of the gel.

Rheometry. A TA Instruments AR-G2 rheometer with a parallel plate geometry (8 mm diameter and 250 μm gap) was used for all experiments. The gels were placed carefully in the headspace with a spatula, and the geometry was then lowered to the preset gap. Oscillatory strain sweeps were performed at 25°C at a fixed angular velocity of 0.5 rad/s. Oscillatory stress sweeps were performed using a fixed angular velocity of 0.5 rad/s. Oscillatory frequency sweeps were performed using a fixed strain of 0.5%.

Atomic Force Microscopy (AFM). A total of 8 μL of $K_2(SL)_6K_2$ in PBS buffer at pH 7.4 (with or without added PAO) were dropped onto freshly cleaved mica while spinning at medium speed on a Headway Research, Inc. photoresist spinner. The sample was rinsed with deionized water for 4-5 s and then spun for an additional 10 min. The sample was then placed in a desiccator until imaging. AFM images were collected in air as described previously. All AFM images were flattened using Nanoscope software and height profiles were generated from the flattened images. From these profiles, for each time point measured (0, 1, 4, and 7 days treatment with PAO and without PAO), 20 fiber heights were averaged and a standard deviation was generated.

References

(1) Georges, P. C.; Levental, I.; De Jesus Rojas, W.; Tyler Miller, R.; Janmey, P. A. *Biophys. Rev. Lett.* **2006**, *1*, 401-410.

(2) Nie, T.; Akins, R. E., Jr.; Kiick, K. L. *Acta Biomater.* **2009**, *5*, 865-875.

(3) Nemir, S.; West, J. *Ann. Biomed. Eng.* **2010**, *38*, 2-20.

(4) Aulisa, L.; Dong, H.; Hartgerink, J. D. *Biomacromolecules* **2009**, *10*, 2694-2698.

(5) O'Connell, K. M.; Langley, D. B.; Shepard, E. M.; Duff, A. P.; Jeon, H. B.; Sun, G.; Freeman, H. C.; Guss, J. M.; Sayre, L. M.; Dooley, D. M. *Biochemistry* **2004**, *43*, 10965-10978.

(6) Herwald, S. E.; Greenaway, F. T.; Lopez, K. M. *Protein Expression Purif.* **2010**, *74*, 116-121.

(7) Galler, K. M.; Aulisa, L.; Regan, K. R.; D'Souza, R. N.; Hartgerink, J. D. *J. Am. Chem. Soc.* **2010**, *132*, 3217-3223.

(8) Concaro, S.; Nicklasson, E.; Ellowsson, L.; Lindahl, A.; Brittberg, M.; Gatenholm, P. *J. Tissue Eng. Regen. M.* **2008**, *2*, 14-21.

(9) Drury, J. L.; Boontheekul, T.; Mooney, D. J. *J. Biomech. Eng.* **2005**, *127*, 220-228.

(10) Ahsan, T.; Harwood, F.; McGowan, K. B.; Amiel, D.; Sah, R. L. *Osteoarthr. Cartilage.* **2005**, *13*, 709-715.

(11) Wilmarth, K. R.; Froines, J. R. *J. Toxicol. Environ. Health* **1992**, *37*, 411-423.

(12) Suva, R. H.; Abeles, R. H. *Biochemistry* **1978**, *17*, 3538–3545.

(13) Shah, M. A.; Scaman, C. H.; Palcic, M. M.; Kagan, H. M. *J. Biol. Chem.* **1993**, *268*, 11573-11579.

(14) Dickinson, E.; Yamamoto, Y. *J. Agric. Food Chem.* **1996**, *44*, 1371–1377.

(15) Carraher, C. *Introduction to Polymer Chemistry*; Taylor & Francis, **2010**.

(16) Aggeli, A.; Bell, M.; Carrick, L. M.; Fishwick, C. W. G.; Harding, R.; Mawer, P. J.; Radford, S. E.; Strong, A. E.; Boden, N. *J. Am. Chem. Soc.* **2003**, *125*, 9619-9628.

(17) Hong, Y.; Legge, R. L.; Zhang, S.; Chen, P. *Biomacromolecules* **2003**, *4*, 1433-1442.

(18) Mata, A.; Hsu, L.; Capito, R.; Aparicio, C.; Henrikson, K.; Stupp, S. I. *Soft Matter* **2009**, *5*, 1228-1236.

(19) Pakstis, L. M.; Ozbas, B.; Hales, K. D.; Nowak, A. P.; Deming, T. J.; Pochan, D. *Biomacromolecules* **2004**, *5*, 312-318.

Chapter 4: Multidomain Peptides as Drug Delivery Vehicles·

Self-assembling peptide nanofiber hydrogels are a promising class of synthetic biomaterials that have been investigated for a wide variety of biomedical applications, including cell scaffolds[1-6] and drug delivery agents.[7-9] The powerful biomedical applications of peptide hydrogels derive from the ease with which new and diverse peptide sequences can be prepared, the nanostructure obtained through their self-assembly,[10] the presentation of chemical information on their surface, and the rheological properties[11-14] of the resulting hydrogel materials. Additionally, these self-assembling peptide nanofiber hydrogels can be designed to bind proteins, cells or to degrade in a predictable fashion with respect to time and location.[15, 16] Successful delivery of therapeutic molecules is dependent on being able to achieve controlled release of these molecules from the peptide hydrogel. Controlled release from peptide hydrogels has been demonstrated with small molecules,[9, 17] and with proteins, for example growth factors.[15, 18, 19] Other hydrogel systems have also been demonstrated to deliver growth factors such as vascular endothelial growth factor (VEGF) to tissues.[20] It has also been shown that delivery of PDGF by self-assembling nanofibers decreases infarct size and improves cardiac function after myocardial infarction.[21] Likewise, tethering of insulin-like growth factor (IGF-1) to self- assembling peptide nanofibers increases survival of neonatal rat

---

· This section is based on two publications:
Yin Wang, Erica Bakota, Benny H. J. Chang, Mark Entman, Jeffrey D. Hartgerink, and Farhad R. Danesh. Peptide Nanofibers Preconditioned with Stem Cell Secretome Are Renoprotective. *J. Am. Soc. Nephrol.*, **2011**, DOI:10.1681/ASN.2010040403.

Erica L. Bakota, Yin Wang, Farhad Danesh, and Jeffrey D. Hartgerink. Injectable Multidomain Peptide Nanofiber Hydrogel as a Delivery Agent for Stem Cell Secretome. *Biomacromolecules*, **2011**, accepted for publication.

cardiomyocytes after myocardial infarction.[22] Peptide hydrogels have also been investigated as an injectable means of delivering stem cells.[23]

A. Embryonic Stem Cells as Therapeutic Agents

Stem cells are known to have beneficial effects on tissues and are being widely investigated as potential therapies. Stem cells hold great promise for the kidney, and multiple studies have suggested that stem cells and specifically mesenchymal stem cells may contribute to the recovery of kidneys after acute kidney injury (AKI).[24-34] However, the mechanism by which stem cells are exerting beneficial effects on the kidney is unclear. The rate of stem cell engraftment in many cases appears too low to explain the significant renal improvement after acute kidney injury. Improvements in the clinical outcome may not necessarily result from direct contact of the diseased tissue with stem cells but rather from another mechanism instead. An alternative hypothesis has been recently advanced, suggesting that the beneficial effects of stem cells in the kidney may not depend on their capacity to reconstitute the denuded cells directly, but rather on their paracrine/endocrine ability to release cytokines, chemokines, and growth factors.[35-38]

Any material with the ability to harness this secretome would carry enormous therapeutic potential, and peptide materials are well-suited for this purpose. In fact, this concept has already been demonstrated with peptide-based materials, in which peptide amphiphile nanofibers were able to absorb and release paracrine factors derived from stem cells and release them in a therapeutic setting.[19]

In the current study, we describe the development of a novel self-assembled peptide nanofiber-based preparation, which effectively delivers paracrine/endocrine factors secreted from mouse embryonic stem cells (ESCs) both *in vitro* and *in vivo*. We hypothesized that the use of nanofibers preconditioned with ESCs might enhance kidney tissue repair by providing an acellular delivery platform for bioactive molecules released from ESCs. We argue that this novel approach could harness the beneficial effects of stem cells in the repair and remodeling of damaged organs, while circumventing many limitations associated with the use of ESCs *in vivo*, including issues with limited cell engraftment, cell viability, immune tolerance, and formation of teratomas.

B. Self-Assembling Multidomain Peptide Nanofibers

Although nanofibers can be prepared in a number of different ways, self-assembly an exceptionally powerful method because it affords excellent control over chemical composition, size in all dimensions, and the dynamic nature of the assembled fiber. Recently we introduced a new class of self-assembling peptide nanofibers called multidomain peptides (MDPs).[10] Designed in this study is a new multidomain peptide, $E_2(SL)_6E_2$GRGDS (Figure 4.1), which incorporates the negatively charged glutamic acid in the charged block and utilizes six pairs of alternating serine, leucine to create the amphiphilic central block. Additionally this peptide includes the well-known cell adhesion sequence RGD.[39, 40] While nanofibers always form in water, gelation is triggered by a number of different methods that result in the neutralization or screening of the negative charges on the glutamic acid residues. A similar method of self-assembly has

been used in other similar peptide systems.[41] While these salts are not required, they dramatically enhance the speed of gelation. In this study, $MgCl_2$ is used due to its compatibility with cell culture conditions.

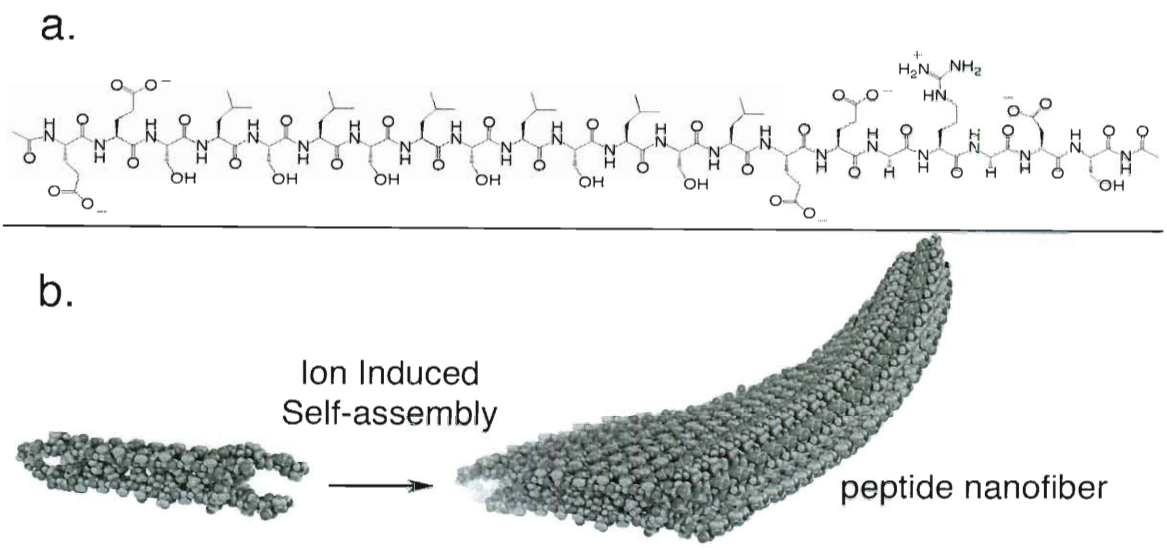

Figure 4.1. Self-assembly of $E_2(SL)_6E_2$GRGDS into nanofibers. (a) Chemical structure of $E_2(SL)_6E_2$GRGDS. (b) Scheme depicting assembly of the peptide dimer repeating unit, a "hydrophobic sandwich" that assembles into a nanofiber.

$E_2(SL)_6E_2$GRGDS was prepared via solid phase peptide synthesis and the product was verified using MALDI-TOF mass spectrometry. After dialysis against deionized water, this peptide was characterized using circular dichroism (CD) and infrared (IR) spectroscopy. CD spectra indicate a β-sheet secondary structure, with minima at 217 nm and maxima at 197 nm (Figure 4.2a). Gelation with Mg^{2+} reinforced this signal, inducing an increase in the maximum at 197 nm with a simultaneous decrease at 217 nm. The IR spectra indicate the presence of an anti-parallel β-sheet structure with an amide $I_{\parallel}$ band at 1616 cm^{-1} and amide $I_{\perp}$ at 1690 cm^{-1} (Figure 4.2b). IR spectra prior to gelation show identical features to the hydrogel (data not shown).

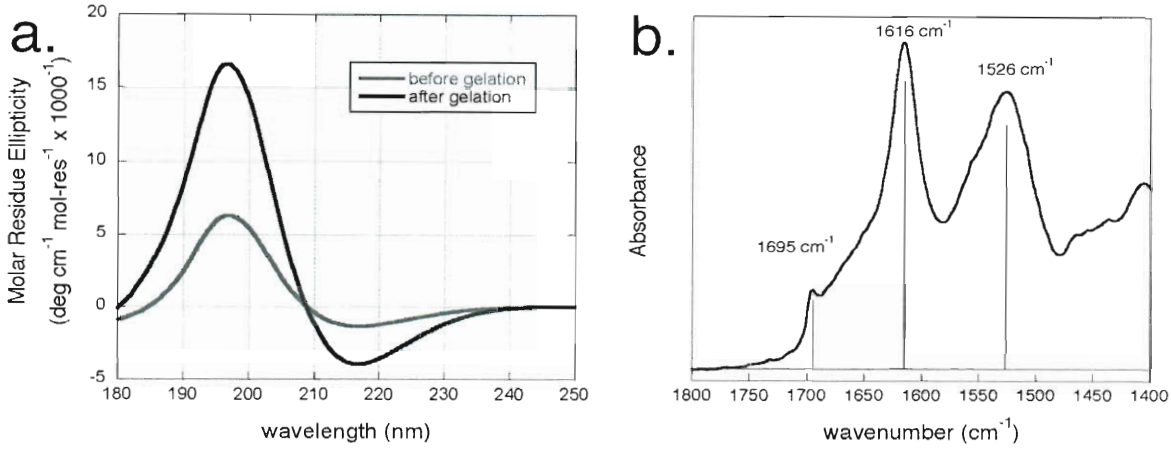

Figure 4.2. a) Circular dichroism (CD) measurements of $E_2(SL)_6E_2$GRGDS before and after gelation with Mg^{2+}. b) Infrared (IR) spectroscopy of $E_2(SL)_6E_2$GRGDS after gelation.

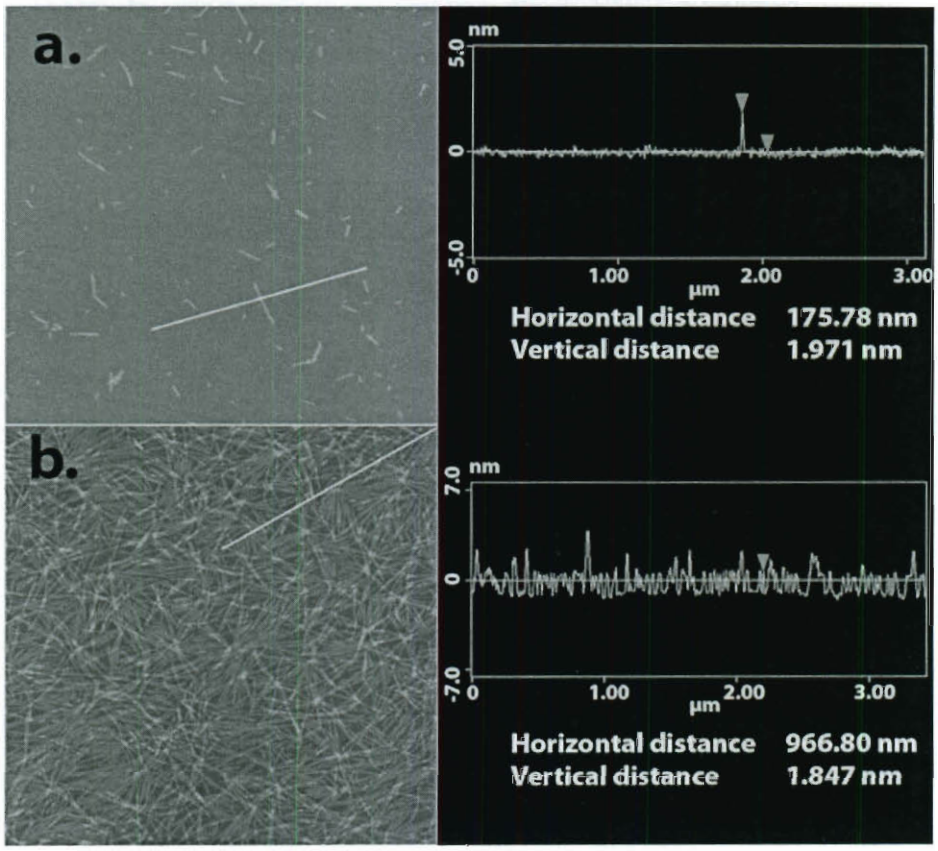

Figure 4.3. Atomic force microscopy (AFM) of $E_2(SL)_6E_2$GRGDS a) before gelation and b) after gelation with Mg^{2+}. White lines in left images indicate the axis of height profiles shown at right. Red triangles denote the points between which the height differential was measured. Images are 3 x 3 µm.

Atomic force microscopy (AFM, Figure 4.3) and vitreous ice cryo-transmission electron microscopy (TEM, Figure 4.4a and 4.4b) confirmed the presence of an extended nanofiber network. These peptide nanofibers result in the formation of a hydrogel in the presence of cell culture media that has been supplemented with Mg^{2+} (Figure 4.4c). It has been well-established that ion screening of charged amino acids plays a huge role in the formation of self-assembled peptide nanofibers.[41] This hydrogel can be visualized by critical point-drying, followed by SEM, which reveals a sponge-like internal structure (Figure 4.4d).

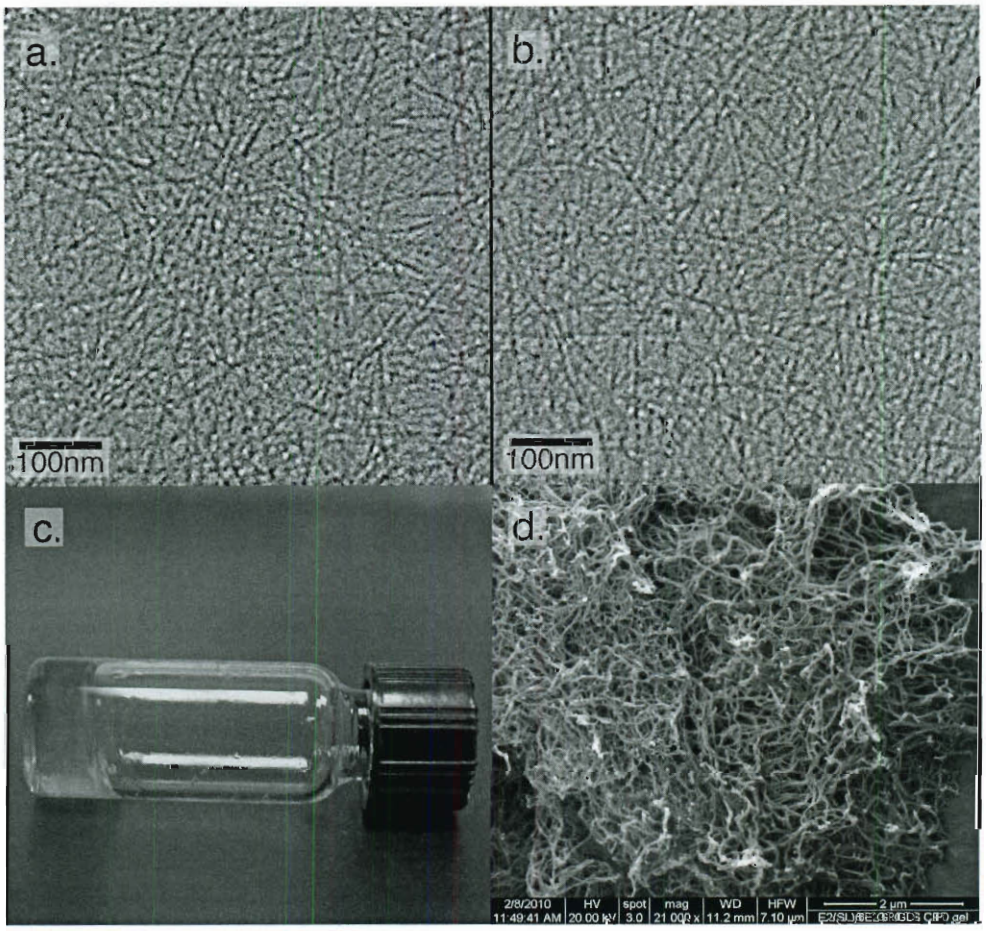

Figure 4.4. a & b) Vitreous ice cryo-TEM of $E_2(SL)_6E_2$GRGDS nanofibers, c) a hydrogel of nanofibers formed in cell culture medium, d) SEM of the resulting peptide hydrogel.

C. *In vitro* studies·

Previous multidomain peptides have demonstrated cytocompatibility,[16] making them appealing for use in biomedical applications such as a drug delivery vehicle *in vitro* and *in vivo*. The ability of the $E_2(SL)_6E_2$GRGDS hydrogel to deliver cytokines to endothelial cells *in vitro* was examined to determine if preconditioned peptide hydrogels could reverse artificially induced cell injury.

1. Effect of Preconditioned Nanofibers on LPS-Induced Cell Hyperpermeability

Lipopolysaccharide (LPS) is a toxin produced by bacteria that is known to have detrimental effects on tissues. The low-dose intraperitoneal (ip) injection of LPS is an established model of endotoxemia as described in several recent studies.[42-45] The underlying molecular mechanisms leading to LPS-induced kidney injury are complex and incompletely understood. However, it is clear that endothelial cell hyperpermeability and cell apoptosis are key mechanisms involved in the pathogenesis of LPS-induced disease.[45-48] Because growth factors and cytokines are also known to affect cell permeability and apoptosis, it was thought that peptide hydrogels loaded with these compounds may have an effect of diseased or injured cells. Thus, the effect of preconditioned nanofibers on these key features of LPS-induced AKI was assessed in a laboratory model.

· Hyperpermeability and apoptosis experiments were performed by Yin Wang, Baylor College of Medicine.

We initially examined the effect of preconditioned nanofibers on LPS-induced endothelial cell hyperpermeability under *in vitro* conditions by determining the permeability of ^{125}I-BSA across confluent endothelial cell monolayers.[49] Our initial strategy was to employ two experimental preparations of nanofibers: (1) encapsulated nanofibers in which ESCs were embedded in designer peptide nanofibers for 1 hour (Figure 4.5a) or (2) preconditioned nanofibers that were prepared by exposing nanofibers to secretome from ESCs in a transwell coculture system for 24 hours (Figure 4.5b). To investigate the effect of preconditioned nanofibers on endothelial cell permeability, we employed a transwell system containing confluent kidney microvascular endothelial cells in the upper chamber separated from preconditioned nanofibers (100 μL) in the lower chamber by a cell-impermeable membrane (Figure 4.5b).

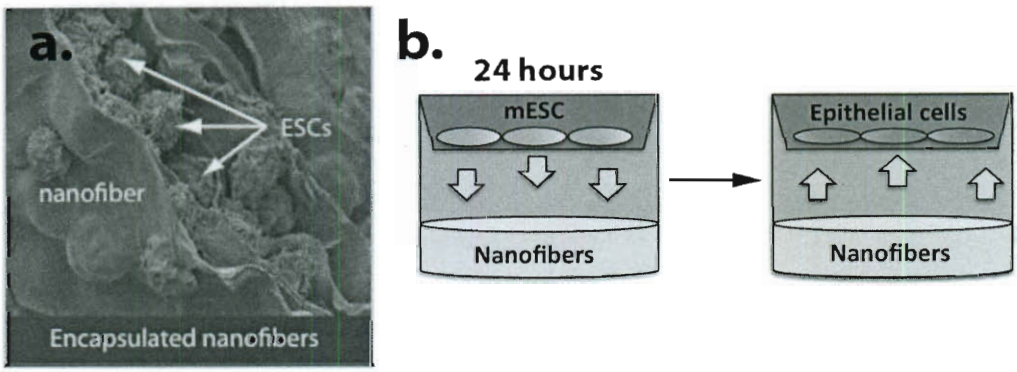

Figure 4.5. a) Scanning electron micrograph of mouse ESCs encapsulated in self-assembled peptide nanofibers. b) Schematic representation of the two-compartment transwell coculture system for preparation of preconditioned nanofibers.

Figure 4.6 depicts the effect of LPS on endothelial cell monolayer integrity. Upon addition of LPS (100 ng/ml) in the upper chamber, we detected a significant increase in endothelial cell permeability. In contrast, cocultures of endothelial cells with either ESCs alone, encapsulated nanofibers, or preconditioned nanofibers prevented LPS-induced

endothelial cell hyperpermeability. However, nonconditioned nanofibers had no effect on LPS-induced cell permeability.

To test whether the modulatory effect of preconditioned nanofibers on cell permeability is restricted to LPS, we assessed the effect of preconditioned nanofibers on vascular endothelial growth factor–induced (VEGF-induced) cell permeability. As shown in Figure 5.6b, preconditioned nanofibers, encapsulated nanofibers, and ESCs alone also prevented VEGF-induced (50 ng/ml VEGF) endothelial cell hyperpermeability. This shows that the modulatory effect of preconditioned nanofibers on endothelial cell permeability is not restricted to LPS, and potentially involves a critical downstream target of cell permeability pathway. Together, these results strongly suggest that preconditioning of nanofibers allows delivery of bioactive molecules from ESCs to targeted cells *in vitro*.

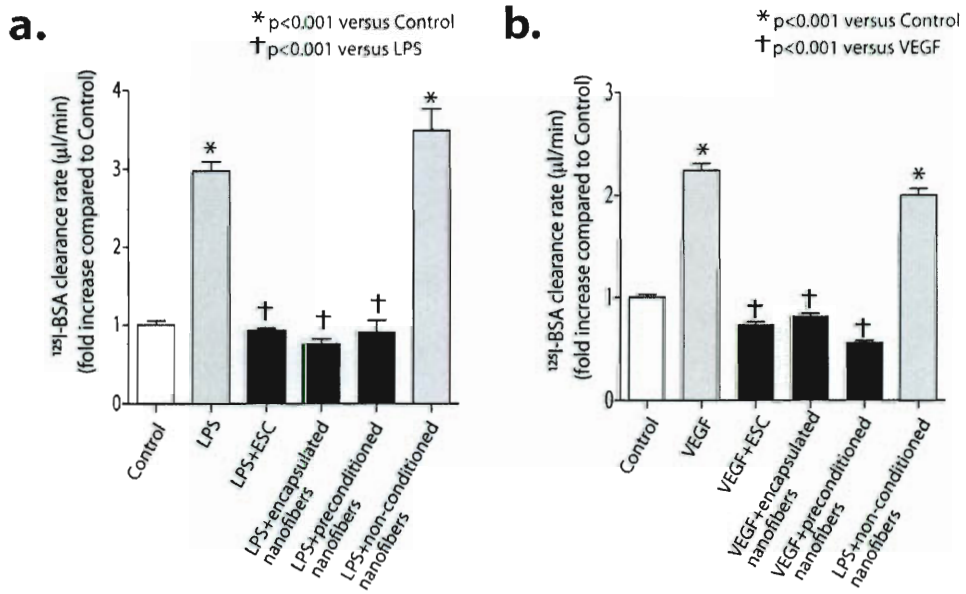

Figure 4.6. a) Quantification of kidney microvascular endothelial cell permeability exposed to LPS (100 ng/ml) for 4 hours. Bar graphs summarize results as mean ±SEM (n = 3 separate experiments in triplicate). b) Quantification of kidney microvascular endothelial cell permeability exposed to VEGF (50 ng/ml) for 6 hours (n = 3 separate experiments in triplicate). Figure by Yin Wang.

2. Preconditioned Nanofibers Decrease LPS-Induced Apoptosis

Having found that preconditioned nanofibers protect against LPS-induced cell permeability, we assessed their effect on LPS-induced cell apoptosis in cell culture. LPS is well known for its toxicity and is often used to simulate kidney injury. We found that LPS treatment (100 ng/mL) significantly increased cell apoptosis in tubular cells and podocytes. In contrast, effect of LPS on cell apoptosis was prevented in the presence of ESCs alone, encapsulated nanofibers, or preconditioned nanofibers.

3. Effect of Preconditioned Nanofibers on Glucose-Induced Cell Hyperpermeability

We also investgated the ability of preconditioned multidomain peptide nanofiber hydrogels to ameliorate a cell culture model for diabetes induced kidney damage. Glomerular Epithelial Cells (GECs) in the kidney form a selectively permeable membrane, which becomes increasingly leaky to proteins at high concentrations of glucose. High glucose conditions, while not typically experienced by healthy individuals, may occur as a result of diabetes. This is a primary mechanism by which diabetes impairs kidney function. It is possible to track the permeability of GECs to protein by measuring the throughput of the protein bovine serum albumin (BSA). After the preconditioning step, the peptide hydrogel is placed in a culture of Glomerular Epithelial Cells (GECs) and the permeability of I^{125} BSA is monitored over time under both low and high glucose conditions. As a control, hydrogels preconditioned by the ESC fibroblast feeder layer were used (pre-MEM-NF). In this control, only the fibroblast layer was used; no ESCs

were present. As expected, GECs were found to have increased permeability in the presence of high glucose levels, which is observed by the 50% increase in clearance rate of I^{125} BSA (Figure 4.7). It was found that in the presence of ESC secretome-loaded MDP hydrogels (pre-hES-NF), the permeability of GECs was reduced to approximately the level of cells treated with low glucose. In contrast, MDP hydrogels preconditioned with the mouse fibroblast feeder layer had no significant effect on BSA clearance.

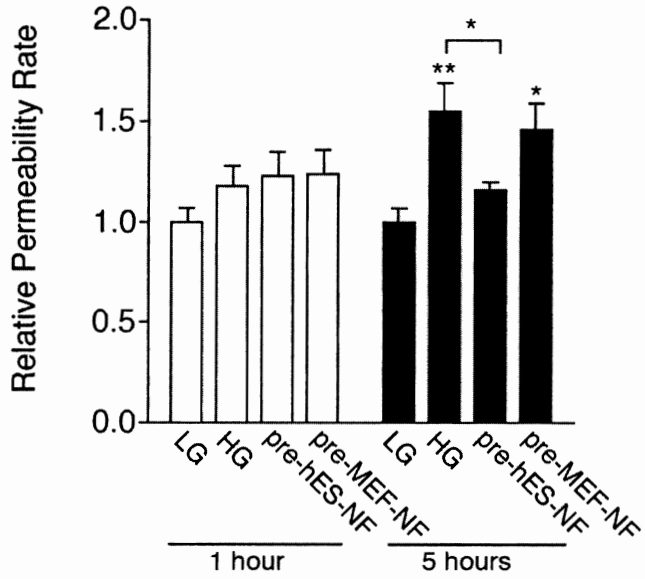

Figure 4.7. Relative permeability rate of albumin of glomerular epithelial cells incubated in low (LG) and high glucose (HG) conditions. Cells in high glucose conditions were also incubated with MDP hydrogel that had been preconditioned either with human embryonic stem cells (pre-hES-NF) or with the mouse fibrobloast feeder layer (pre-MEF-NF). Data are shown as mean ± SEM. Statistical significance was assessed by performing analysis of variance (ANOVA) followed by the Tukey-Kramer post-hoc analysis for multiple comparisons using an alpha value of 0.05. * $P<0.05$, ** $P<0.01$.

D. *In vivo* studies

1. Rheological Properties of $E_2(SL)_6E_2$GRGDS Hydrogels

Once the utility of $E_2(SL)_6E_2$GRGDS had been established *in vitro*, its suitability as an *in vivo* material was investigated. Materials designed for use in a clinical setting are subjected to very different conditions from those used in a laboratory setting. For example, a peptide hydrogel might undergo negligible stress or strain while in a cell culture well plate but may experience considerable deformation when injected through a syringe and needle. Thus it was necessary to examine the hydrogel's mechanical properties to determine its suitability for clinical use.

A peptide hydrogel designed for drug delivery in a clinical setting should have several useful mechanical properties: stability of the hydrogel over time, the ability to undergo shear thinning and subsequently recover, and the ability of the hydrogel to be loaded with therapeutics and subsequently release them in a targeted environment. The multidomain peptide $E_2(SL)_6E_2$GRGDS satisfies all of these conditions. The stability of this peptide was first tested on a controlled-stress rheometer by performing a time sweep, which showed that the peptide hydrogel was stable over the time frame necessary to complete rheological tests. The peptide hydrogel was also measured over the course of several weeks, and no significant changes were observed. Thus, incubation time does not affect the rheological properties of the hydrogel. The rigidity of this peptide was tested on a controlled-stress rheometer by performing a strain sweep (Figure 4.8a), which shows a storage modulus of approximately 480 Pa. One potential limitation of peptide hydrogels

is that their fragility may make delivery of the hydrogel in a biological setting impractical. On the other hand, excessive robustness without shear thinning may preclude injection of a hydrogel altogether. Peptide materials have been shown to avoid both of these issues, making them ideal drug delivery systems.[9] $E_2(SL)_6E_2$GRGDS specifically demonstrates an ability to both undergo shear thinning and recover rapidly after needle shear, thus allowing injection of the peptide hydrogel directly into the site of interest without permanent loss of hydrogel properties. Needle shear was simulated by applying 100% strain for 1 minute. This was immediately followed by monitoring the recovery of the elastic modulus, G', over time. It was found that this peptide recovers over 75% of its elastic modulus immediately (within 13 seconds, the smallest time interval measured during rheometry) and 100% of its elastic modulus within 10 minutes of removal of the shear (Figure 4.8b).

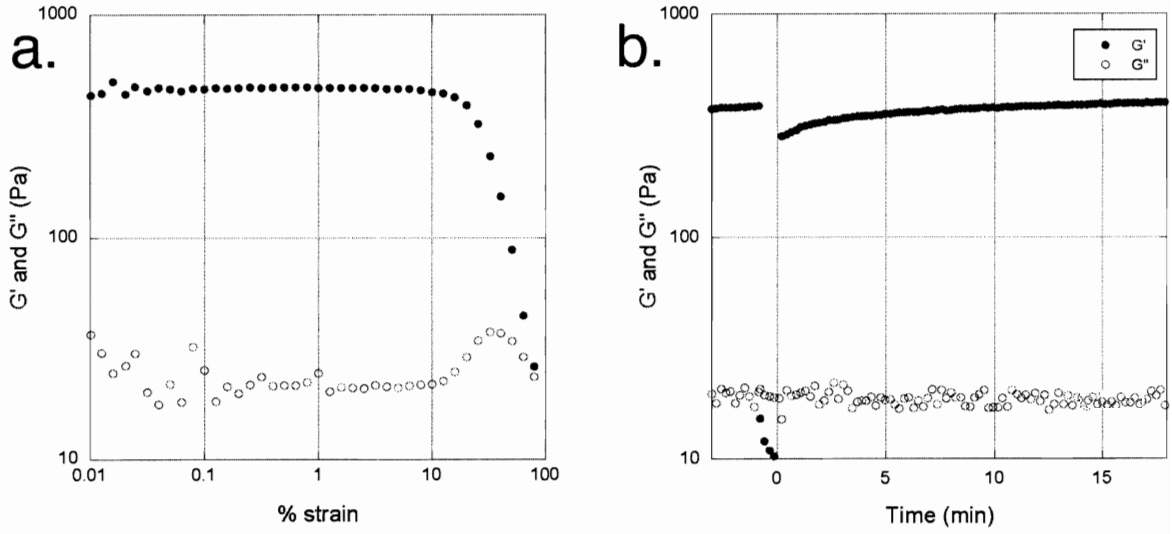

Figure 4.8. (a) Strain sweep performed after gelation with Mg^{2+}. (b) Time sweep performed on $E_2(SL)_6E_2$GRGDS gel, with shear being applied at T = -1 and removed at t=0.

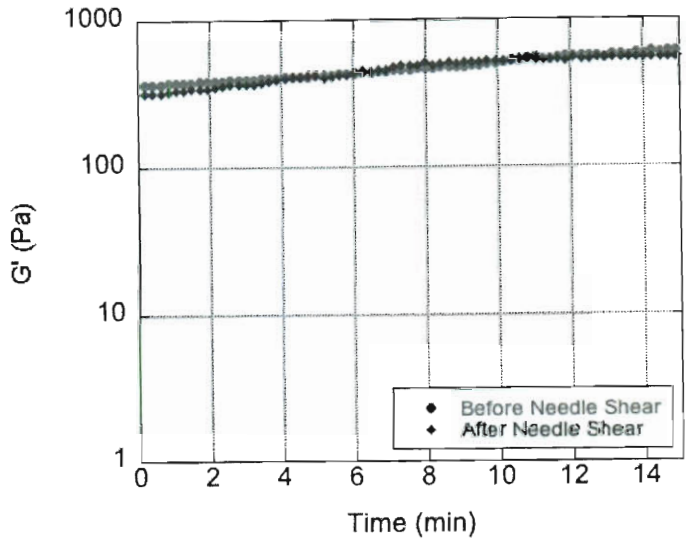

Figure 4.9. Time sweeps performed on the peptide hydrogel before needle shear (red) and after needle shear (blue) using a syringe fitted with a 21 G needle.

However, it is important to note that simulated needle shear may not be identical to actual needle shear due to differences in geometry between the rheometer and a syringe, so shear-thinning tests were then performed using a syringe and 21 G needle. In these experiments, the peptide was placed carefully on the rheometer plate (taking care to disturb the gel as little as possible) and a time sweep was performed to measure the elastic modulus of the gel over 15 minutes. Then the peptide was removed, loaded with a spatula into a syringe fitted with a 21 G needle, and the gel was squirted through the needle onto the rheometer plate, where the elastic modulus of the gel was monitored over another 15-minute interval (Figure 4.9). After shearing through the syringe and needle, it was evident that the G' of the gel was not affected. Thus, gels of this type are well-suited for delivery via injection.[14]

2. MRI Tracking Experiments

The peptide hydrogel's ability to be used as a drug delivery matrix was then examined. First, a tracking experiment was performed to ascertain the fate of the hydrogel upon injection. Gadolinium is frequently used to enhance contrast in magnetic resonance imaging (MRI), and it is estimated that at least 30% of MRIs performed today utilize chelated gadolinium for this purpose.[50] A Gd^{3+} labeled version (see Supporting Information) of the hydrogel was prepared and carefully injected into the abdominal cavity of a mouse, and the localization of the hydrogel was monitored by magnetic resonance imaging (MRI). After injection, scans were acquired at 30 minutes, 1.5 hours, 3 hours, 6 hours, 12 hours and 24 hours. All experiments were repeated at least in triplicate.[51-54] Figure 4.10 shows that the labeled hydrogel can be visualized at 24 hours post-injection, demonstrating that a peptide hydrogel could be delivered to a site of interest without immediate dissolution into the surrounding body tissues. This lack of dissolution is related to the ability of this hydrogel to recover after shearing through the syringe and needle. The rapid recovery of the elastic modulus after needle shear allows the gel to regain its nanostructure faster than the time that is required to flow into the surrounding body tissues. Thus, the $E_2(SL)_6E_2$GRGDS hydrogel is ideally suited for injection *in vivo*, as it maintains structural integrity immediately following injection.

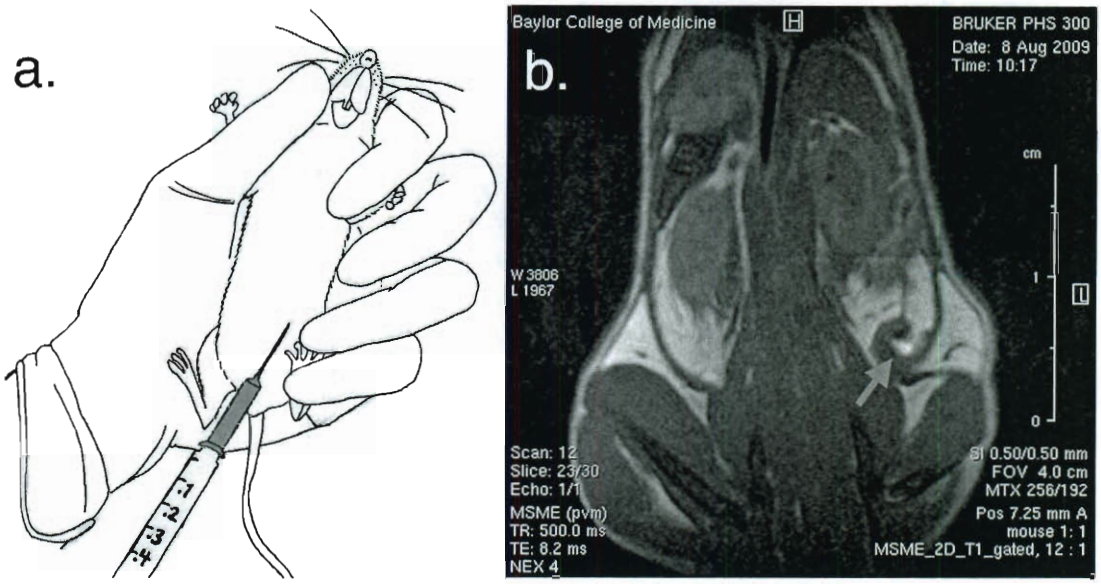

Figure 4.10. *Left*: Nanofibrous MDP hydrogel undergoes shear thinning and shear recovery allowing simple injection *in vivo*. *Right*: MRI tracking of gadolinium-labeled nanofibers 24 hours after injection into the abdominal cavity of mouse. The red arrow indicates the position of the localized hydrogel.

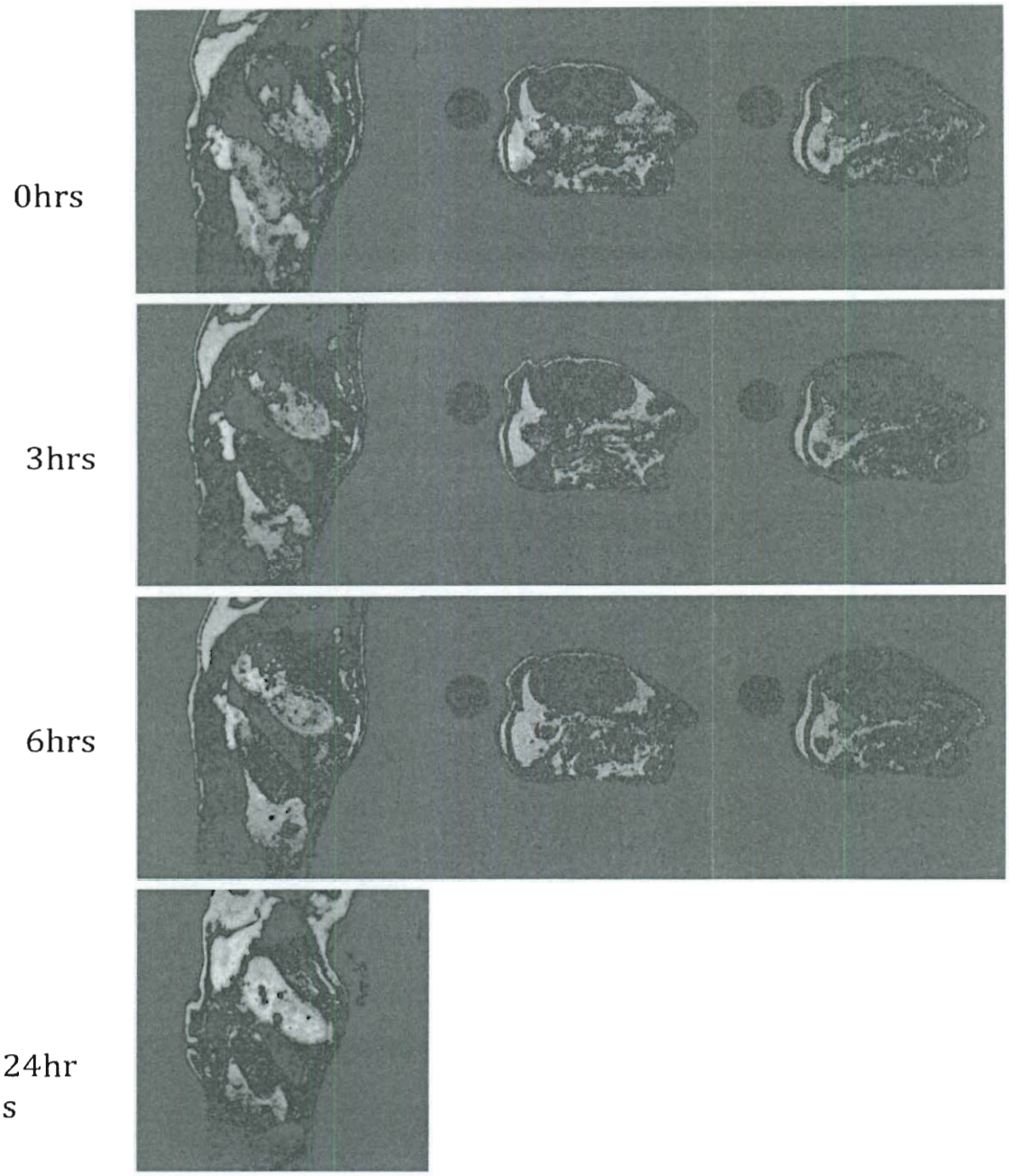

Figure 4.11. Magnetic resonance imaging (MRI) of localized hydrogel at 0, 3, 6, and 24 hours post-injection. At 24 hours concentrated areas of hydrogel can still be observed.

3. Effect of Preconditioned Nanofibers on the LPS Model of AKI in Mice·

The experiments described above provide strong evidence for a protective effect of preconditioned nanofibers *in vitro*. Furthermore, rheological studies indicated that the $E_2(SL)_6E_2$GRGDS hydrogel behaves ideally for use as an injectable material. However, it was unclear whether preconditioned nanofibers would actually exhibit the expected renoprotective effects *in vivo*. To address this question, we examined the effect of preconditioned nanofibers on the LPS model of AKI in mice.[42] A single intraperitoneal injection of LPS (10 μg/g body weight) produced a significant increase in albuminuria and caused an abrupt rise in serum BUN and creatinine (Figure 4.12, a-c). Serum BUN and creatinine are considered the gold standard for biomarkers of kidney function. Increased serum BUN and creatinine are indicative of a disease state. In contrast, intraperitoneal treatment with preconditioned nanofibers (200 μL) 1 hour after LPS injection markedly prevented LPS-induced proteinuria (Figure 4.12, a and b). Likewise, serum BUN and creatinine levels were significantly reduced in mice administered preconditioned nanofibers (Figure 4.12c). This indicates that preconditioned nanofibers improved kidney function in treated mice.

· Experiments on AKI in mice were performed by Yin Wang, Baylor College of Medicine.

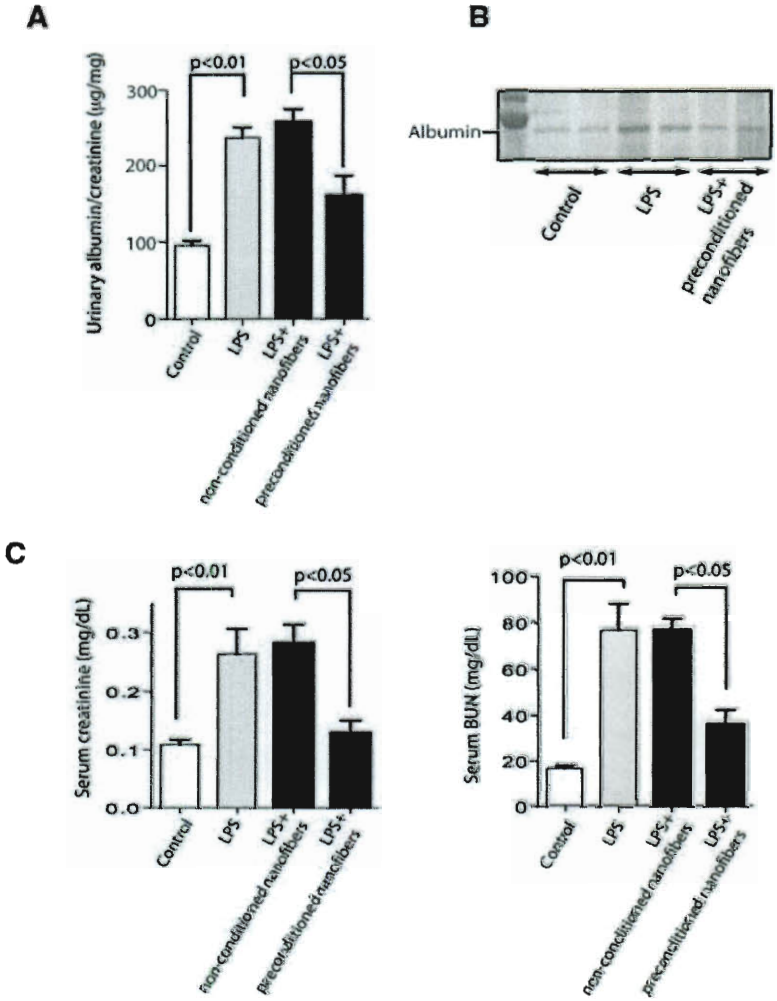

Figure 4.12. Mice treated with preconditioned nanofibers are protected from LPS-induced kidney injury. A) Quantitative analysis of albumin/ creatinine ratio (n = 6 to 11 per group). B) Representative SDS-PAGE analysis of the urine. C) Quantitative analysis of serum creatinine and BUN (n = 6 to 11 per group). Figure by Yin Wang.

Histologic analyses of kidneys obtained from animals allocated to preconditioned nanofibers with ESCs also showed a remarkable improvement (Figure 4.13a). Tubular epithelial cells were swollen and vacuolated 24 hours after LPS administration, but significantly improved in mice that received treatment with preconditioned nanofibers. We also assessed the effect of preconditioned nanofibers on podocyte injury based on two recent studies.[42, 43] As depicted in Figure 4.13b, preconditioned nanofibers ameliorated LPS-induced podocyte effacement observed in some glomerular areas.

Similarly, although administration of LPS caused a significant increase in cell apoptosis in peritubular, vascular, tubular, and podocytes, the use of preconditioned nanofibers markedly mitigated the number of apoptotic cells in the kidneys (Figure 4.13, c and d). Furthermore, we also performed caspase-3 activation assays. LPS caused a significant increase in caspase-3 activation (Figure 4.13e). This increase was prevented in mice treated with preconditioned nanofibers. Together, these results suggest that the preconditioned nanofibers protect against LPS-induced apoptosis in the kidney *in vivo*. Next, we examined the effect of preconditioned nanofibers on the ischemia-reperfusion (I-R) model of kidney injury. As shown in Figure 4.13, f and g, in comparison with sham animals, mice that were subjected to I-R injury and were allocated to nonpreconditioned nanofibers showed a significant elevation of serum creatinine and BUN at 24 hours. However, mice that received preconditioned nanofibers intraperitoneally exhibited a marked improvement in serum creatinine ($P < 0.05$) and BUN ($P < 0.05$). Taken together, these findings suggest that preconditioned nanofibers protect against kidney injury in different models of AKI.

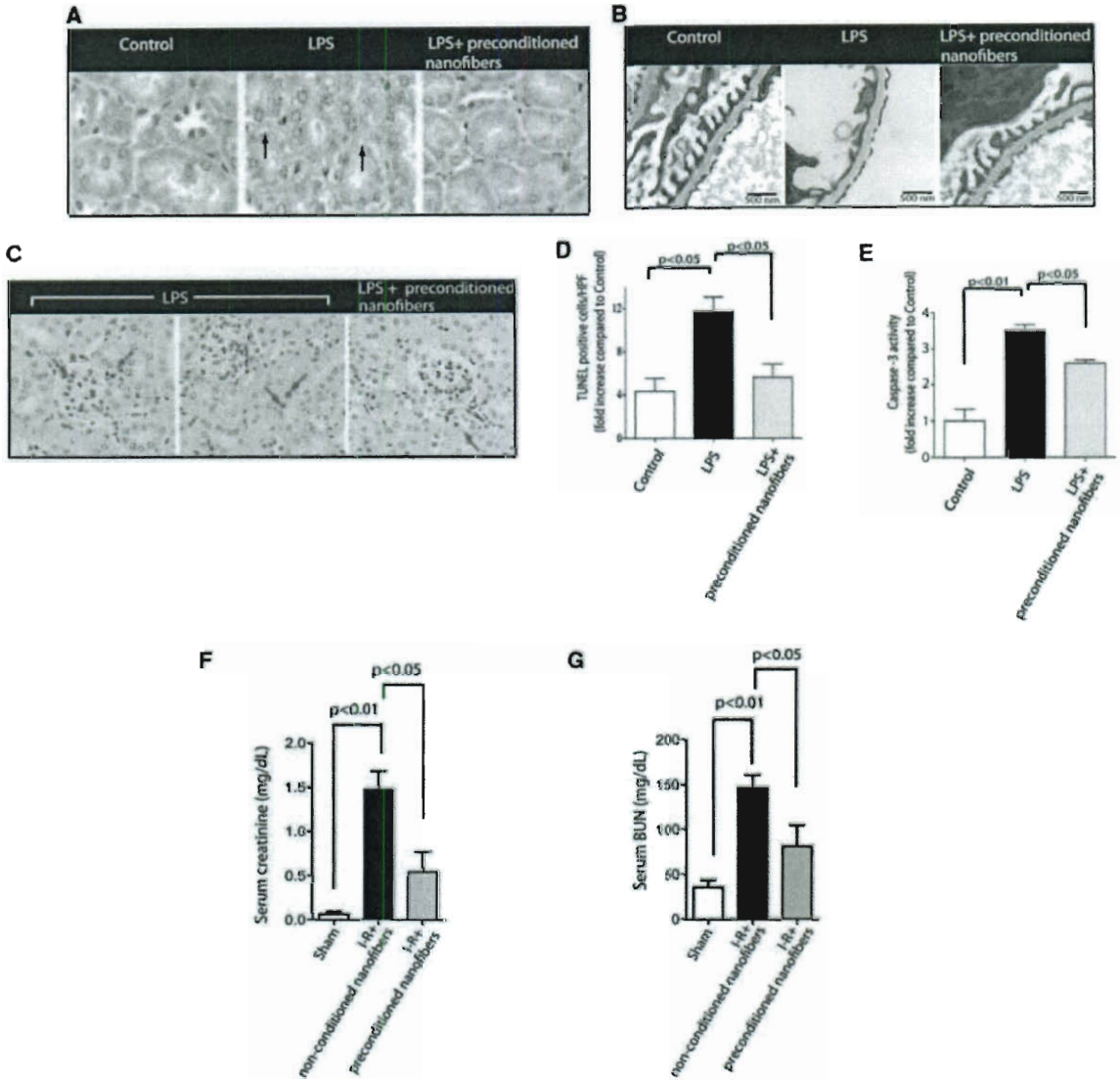

Figure 4.13. A) Renal histology was assessed by H&E staining 24 hours after LPS administration. Tubular injury is indicated by vacuolization of tubular epithelial cells (arrows) (original magnification: 400x). B) Representative TEM images of the glomerular capillary wall. LPS-treated mice exhibit effacement of foot processes, whereas mice treated with preconditioned nanofibers show a significant improvement in podocytes (original magnification: 15,000x). C) Apoptosis was quantified by TUNEL staining of formalin-fixed kidney tissue. After LPS administration, apoptotic nuclei were identified in glomeruli, tubules, and arterioles (arrows) (Magnification: 400x counterstained with hematoxylin). Apoptosis was quantified as described previously.[55] D) Results of apoptosis obtained from five different mice in each group. HPF, high power field. E) Results of caspase-3 activation obtained from kidney cortex lysates (n = 5 mice per group). F) Quantitative analysis of serum creatinine and BUN G) (n = 6 mice/group) in the I-R model of AKI. Data are shown as means ± SEM. Figure by Yin Wang.

E. Analysis of Secretory Proteome from Preconditioned Nanofibers

ESCs have been shown to secrete a broad spectrum of cytokines, chemokines, and growth factors.[56] We performed a semiqualitative cytokine antibody array analysis to assess the secretome from preconditioned nanofibers. To this end, preconditioned nanofibers were transferred to a solution of PBS, and the PBS solution was then removed and replaced periodically to assess the release of secreted proteins. As a control, nonconditioned nanofibers were also analyzed. Overall, a total of 36 secreted proteins were differentially increased in conditioned PBS (Figure 4.14a). This suggests that preconditioned nanofibers can retain and release paracrine/endocrine factors from ESCs.

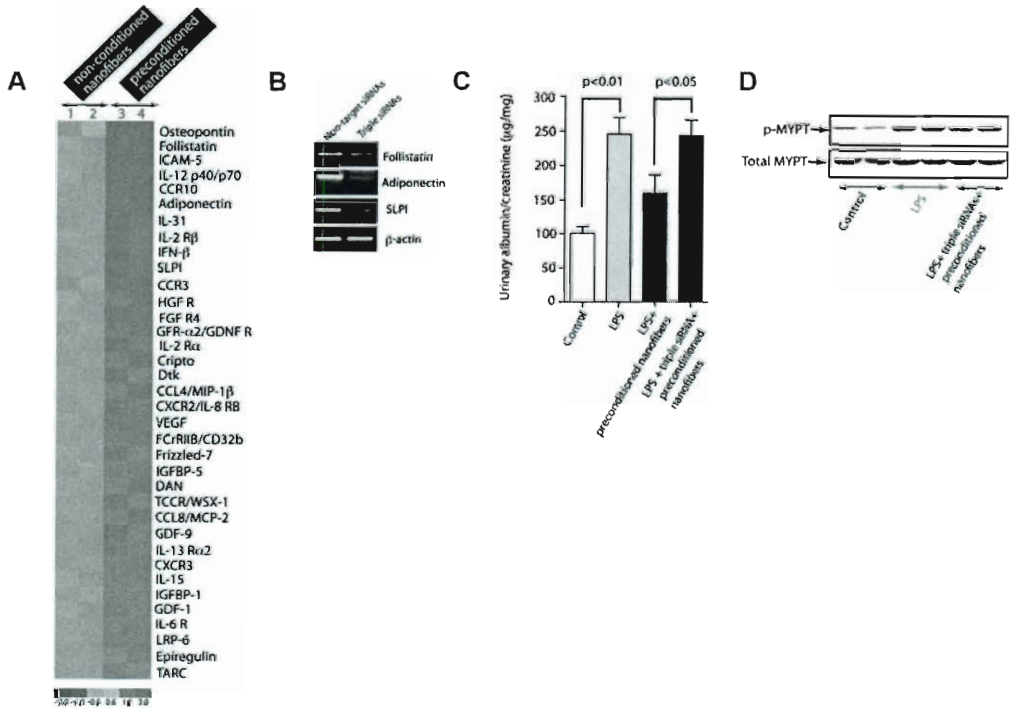

Figure 4.14. A) Cytokine array profiling was performed on nonconditioned and preconditioned nanofibers using a biotin-labeled cytokine protein array system. B) Knockdown of three secreted proteins (follistatin, adiponectin, and SLPI) showing the reduction at the mRNA levels. C) Quantification of albumin/creatinine ratio in mice treated with preconditioned nanofibers after simultaneous triple knockdown. D) Immunoblot of Rho kinase activation from kidney lysates. Figure by Yin Wang.

To dissect the contribution of differentially expressed secreted proteins in the renoprotective effects of preconditioned nanofibers, we targeted proteins that were previously reported to play critical roles in the LPS model of organ injury. A survey of the literature prompted us to target follistatin, adiponectin, and secretory leukoprotease inhibitor (SLPI) as our initial targets.[57-59] Because we expected that the effects of preconditioned nanofibers might stem from multiple secreted proteins, in addition to designing siRNA oligos directed against the individual genes, we also used a combinatorial siRNA strategy for their simultaneous knockdown. To this end, before preconditioning of nanofibers, ESCs were transfected with siRNAs for individual or multiple genes simultaneously. Nanofibers were then preconditioned as described previously. We found that triple simultaneous knockdown of follistatin, adiponectin, and SLPI in ESCs prevented the renoprotective effect of preconditioned nanofibers *in vivo* (Figure 4.14, b and c). With use of a combinatorial knockdown of these three genes, strong Rho kinase activation also remained unchanged in the kidneys of mice treated with LPS even in the presence of preconditioned nanofibers (Figure 4.14d). This suggests a critical role for follistatin, adiponectin, and SLPI as well as for Rho kinase activation as the underlying molecular mechanism by which preconditioned nanofibers exert their renoprotective effect. Interestingly, individual knockdown of these genes failed to prevent the effect of preconditioned nanofibers on Rho kinase activation. We also evaluated the effect of conditioned medium (ESC-CM) on our experimental model of AKI. Mice were injected intraperitoneally with conditioned medium (200 μL per mouse) 1 hour after injection of LPS. Interestingly, no significant benefit was observed with ESC-CM on albuminuria. This suggests that our designer nanofiber facilitates the uptake

of proteins from secretome, a feature not surprising considering that nanofibers exhibit extremely high surface area-to-volume ratio.[60]

Finally, we asked whether the use of preconditioned nanofibers would protect the secretome from proteolysis. We characterized the effect of preconditioned nanofiber on the degradation of osteopontin (OPN), a secreted glycoprotein, which was significantly upregulated in the secretome. We used purified recombinant OPN and active matrix metalloproteinase 3 (MMP3) to perform a cleavage assay. In the presence of MMP3, OPN was cleaved to generate two additional fragments (40 and 32 kD). However, in the presence of preconditioned nanofibers, the pattern of cleavage of OPN was very similar to the control sample with the absence of low molecular weight bands, supporting the notion that preconditioned nanofibers provide a protease resistant environment.

F. Conclusions

In conclusion, we have shown that the multidomain peptide hydrogel self-assembled from $E_2(SL)_6E_2$GRGDS is a suitable biomaterial for ESC secretome delivery. In the laboratory, drug loading and delivery has demonstrated by preconditioning the hydrogel in the presence of ESC and using these cell-free constructs to repair populations of cells that have been damaged either through LPS-induced injury or high glucose conditions. In both models of kidney disease, the peptide hydrogel was able to alleviate the increased permeability associated with the renal disease state. These results were echoed *in vivo*, as the preconditioned $E_2(SL)_6E_2$GRGDS hydrogel was able to ameliorate high protein throughput in the urine that was associated with LPS-induced kidney injury. These

peptide nanofiber hydrogels exhibit clear cytoprotective properties. Our results also identify follistatin, adiponectin, and SLPI as the key peptides in the therapeutic effects of preconditioned nanofibers.

In addition to encouraging *in vitro* results, $E_2(SL)_6E_2$GRGDS is an ideal injectable material. It forms a stable, nanofibrous hydrogel in the presence of Mg^{2+} and undergoes rapid shear thinning and recovery, allowing it to be easily delivered by syringe. Labeling with gadolinum via a covalently attached chelate illustrates the localization of the β-sheet nanofiber network after injection *in vivo*. This phenomenon allowed directed and localized therapy in mice being treated for acute kidney injury.

On the basis of these findings, we propose that preconditioned nanofibers serve as a novel acellular delivery platform for a broad spectrum of stem cells applications whereby beneficial effects of stem cells are preserved, whereas many limitations of stem cell therapy are circumvented. Coupling of peptide nanofibers with ESCs presents several advantages: (1) it provides an acellular platform for delivery of secretome from stem cells; (2) it offers an opportunity for a wider preclinical and clinical use of ESCs after organ injury because it circumvents the potential formation of teratomas; (3) by modifying the designer peptide motifs, it is possible to pursue a more targeted therapy; (4) it may extend the biologic activity of cytokines and chemokines secreted from ESCs; (5) it can be used to dissect the paracrine/endocrine effects of stem cells on gene expression or cell-signaling processes; and (6) peptide nanofibers can break down into natural amino acids, which are nontoxic. Thus, peptide nanofibers may be useful as a bio-reabsorbable source of delivery of secretome for kidney repair. A main advantage of using preconditioned nanofibers, which can potentially explain the lack of tissue pro-

tective effects with ESC-CM, is the extremely high surface area-to-volume ratio of nanofibers that could facilitate the uptake and release of proteins delivered by the nanofibers.[60] The combined topographical and biochemical signaling from peptide nanofibers may also play a role in enhancing biologic activities of paracrine/endocrine factors secreted from ESCs.

In summary, we describe the demonstration of peptide nanofiber hydrogel as a novel platform for delivery of secretome released from stem cells. Our findings illustrate the utility of preconditioned nanofibers in developing alternatives to conventional stem cell therapy for a diverse set of diseases, including those involving kidney injuries.

G. Experimental

Peptide synthesis. All peptides were prepared by traditional solid phase peptide synthesis as described previously. A Rink Amide MBHA low loading resin (0.34-0.38 mmol/g) was used to ensure higher peptide yields.

Peptide Gelation. A 1 wt% solution of $E_2(SL)_6E_2$GRGDS was prepared by dissolving the lyophilized powder in deionized water which was subsequently adjusted with NaOH to pH 7. While the peptide adopts a β-sheet structure in the absence of additional salts, the addition of $MgCl_2$ enhances nanofiber formation and results in the formation of a gel. Mg^{2+} to peptide ratios of 2:1 to 8:1 were investigated, and it was determined that the 4:1 ratio imparted the optimal rheological properties to the peptide hydrogel. $MgCl_2$ (1 M) at pH 7 was added so that the final ratio of Mg^{2+} to peptide was 4:1 (1% peptide by weight

= 4.45 mM, thus Mg^{2+} is 17.8 mM). The vial was capped, shaken briefly, and sonicated to obtain a uniform gel, which formed within seconds of mixing. Peptide preparations described as un-gelled are prepared as above but without addition of $MgCl_2$.

Circular Dichroism Spectroscopy. CD spectra were recorded using a Jasco-810 spectropolarimeter. For non-gelled peptides, samples at 1 wt% and pH 7 (adjusted with NaOH when necessary) were placed in a quartz cuvette with a path length of 0.001 cm. For samples gelled with Mg^{2+}, the resulting 1 wt% gel at pH 7 was carefully pipetted into a 0.001 cm path length quartz cuvette, making sure to avoid bubble formation. Spectra were recorded at room temperature from 250 to 180 nm, with a 0.2 nm data pitch and a scan rate of 50 nm/min. Milidegrees of rotation were converted to molar residual ellipticity (MRE).

Attenuated Total Reflectance Infrared Spectroscopy (ATR-IR). 5 μL of 1 wt% $E_2(SL)_6E_2$GRGDS gel (gelled by the addition of Mg^{2+}, as described above) at pH 7 were pipetted onto a "Golden Gate" diamond window and dried under nitrogen until a thin film of peptide was achieved. IR spectra (32 accumulations) were taken using a Jasco FT/IR-660 spectrometer.

Atomic Force Microscopy. 1 wt% peptide solutions at pH 7 (both gelled and un-gelled) were diluted to a concentration of 0.01-0.05 wt% with ultra pure water. Samples were prepared as described in previous chapters. AFM images were collected as described previously. Gelled and un-gelled samples were prepared and imaged

separately. Data were collected in height and amplitude channels. Height profiles were measured using Nanoscope software.

Vitreous Ice Cryo-Transmission Electron Microscopy (cryo-TEM) of Peptide Gels. Vitreous ice cryo-TEM samples were prepared using a controlled environment vitrification system (Vitrobot, FEI). 2.6 µl of 2 wt% peptide gel were pipetted onto a holey carbon grid (Quantifoil R1.2/1.3) and blotted with filter paper (Ted Pella, Inc.) for 1 second. The sample then was quickly plunged into liquid ethane. The sample was transferred from liquid ethane to liquid nitrogen for storage. The sample was imaged as described previously.

Scanning Electron Microscopy (SEM) of Nanofibers. 100 µL aliquots of each gel were prepared and placed in a 24 well plate. Gels were dehydrated in a series ethanol/water solutions progressing from 30% ethanol to 100% ethanol over the course of 24 hours. The dehydrated gels were critical point dried using an Electron Microscopy Sciences EMS 850 critical point drier. They were then affixed to SEM pucks using conductive carbon tape. The pucks were sputter coated with 10-15 nm gold using a CRC-150 sputter coater and imaged using an FEI Quanta 400 ESEM at 20.00 kV.

Scanning Electron Microscopy (SEM) of Embedded Cells. Cells were fixed with 3% glutaraldehyde plus 2% paraformaldehyde and 7.5% sucrose in 0.1 M cacodylate, postfixed with 1% cacodylate buffered osmium tetroxide plus 7.5% sucrose, dehydrated with graded series of hexamethyldisilazane-ethanol (HMDS-ethanol) series and air-dried

overnight. Samples were examined with a JSM-5910 scanning electron microscope (JEOL USA, Peabody, MA) at an accelerating voltage of 5 kV.

Cell Culture. Conditionally immortalized renal microvascular endothelial cells were kindly provided by Dr. Robert Langley (University of Texas, M.D. Anderson Cancer Center)[61]. Conditionally immortalized mouse renal podocytes were provided by Dr. Peter Mundel (University of Miami).[62, 63] Mouse embryonic stem cell line (ESC-D3) was obtained from the Center for Stem Cell and Regenerative Medicine (Baylor College of Medicine) and derived from 129/Sv+/+ mouse as described previously and according to previously reported methods.[64] HK2 cells (ATTC, Manassas, VA) were grown in complete keratinocyte serum-free media. Mouse embryonic fibroblasts (MEF) were obtained from 13-day-old CF-1 mouse embryos (Charles River) and according to previously reported methods.[65] Cells were released by trypsin/EDTA digestion for 30 minutes and harvested in 75-cm^2 culture flasks at a density of 3 x 10^5 per mL in MEM-α supplemented with 10% FBS (Life Technologies, USA). Subcultures were prepared after the cells reached a confluence of >90% in the same medium.

Preparation of Preconditioned Nanofibers and Conditioned Media. Preconditioning of nanofibers was performed by exposing nanofibers (100 μL) to ESCs (2 x 10^5 cells) for 24 hours in 24-well inserts (0.4-μm pore size) of a two-compartment transwell coculture system (BD Biocoat, MA) in which nanofibers were placed in the lower com- partment, whereas ESCs were seeded in the upper compartment in the presence of serum-free medium (knockout DMEM).[66, 67] After 24 hours of conditioning, ESCs were removed

and media replaced. To prepare for encapsulated nanofibers, 2 x 10^5 ESCs were mixed with 100 μL of nanofibers for 1 hour. Conditioned media from ESCs (ESC- CM) was prepared with 2 x 10^5 ESCs incubated in the presence of serum-free knockout DMEM for 24 hours in an incubator at 37°C with 5% CO_2 in 95% air. The ESC-CM was then collected and concentrated by ultrafiltration using centrifugal filters with a 3-kD molecular weight cut-off (Amicon Ultra-PL 3; Millipore, Bedford, MA).

LPS (Escherichia coli 0111:B4). LPS was obtained from List Laboratories (Campbell, CA). Antifibrin antibody was purchased from Nordic Immunological Laboratories (Tilburg, The Netherlands). Polyclonal anti-phospho myosin phosphatase targeting subunit 1 (MYPT-1) (T853) antibody, recombinant MYPT-1, and recombinant Rho kinase 2 protein were from Upstate Biotechnology (Lake Placid, NY). Goat polyclonal antiosteopontin (OPN) antibody was from Abcam (Cambridge, MA), and anti-OPN rabbit polyclonal antibodies were obtained from Alexis Biochemicals (San Diego) and Rockland Immunochemicals (Gilbertsville, PA). Recombinant rat VEGF-A164 and human recombinant osteopontin (huOPN) were acquired from R&D Systems (Minneapolis). The catalytic domain of the matrix metalloproteinase (MMP)-3 was obtained from Alexis Biochemicals (San Diego). Cell culture media and supplies were from Invitrogen (Carlsbad, CA).

Rheometry. Rheological measurements were taken using a TA Instruments AR-G2 rheometer. Approximately 20 μL of peptide solution were placed within a preset gap of 250 μm on an 8 mm steel parallel plate geometry. A frequency sweep was performed at

25 °C and a frequency of 1 rad/sec was found to be in the linear viscoelastic region (LVR). This value was used to perform a strain sweep at 25 °C and 1 rad/sec. Time sweep tests were performed at 25 °C to determine the initial stability of the hydrogel as well as the recovery ability after shear. No breakdown of the gel was detected during time sweep measurements. In shear and recovery tests, the sample was pre-sheared to 100% strain for 1 minute and then a time sweep was performed at a frequency of 1 radian/sec and 0.5% strain for 20 minutes. To ensure that the sample only underwent shear rather than slipping, the phase angle was kept below 90°.

Gadolinium Labeling of Peptides. The protocol for gadolinium labeling was obtained from BioPal (BioPAL, Inc. Worcester, MA) and followed as written. Dry peptide was dissolved in 0.2 M carbonate buffer at pH 8 and set aside. Separately, 393 μL of a solution of 1 M sodium acetate and 1 M NaOH were added to a 2 mL vial containing ~ 5 mg proprietary chelate. 7 μL of 1 M $GdCl_3$ were then added to this solution, which was then capped and vortexed until all solids were dissolved. This solution was allowed to sit for 5 minutes, and then 3 equivalents of the Gd-chelate solution were added to the peptide solution. This solution was allowed to mix for 2 hours and was then purified by dialysis and subsequently lyophilized. The powder was reconstituted in phosphate-buffered saline and gelled by addition of Mg^{2+}.

Animal Setup for MRI Tracking. Female C57BLKS/J mice weighing 20-30 g were purchased from Jackson Lab. Mice were intubated and inhalational isoflurane (1.5–2%) was administered through the endotracheal tube. Pulse and oxygenation, temperature,

end-tidal CO_2 and respiratory rate were monitored during the entire MRI scan period. The mice were kept warm using a water heater. 200-300 μL Gd-conjugated nanofibers were injected into the mice using a 1 mL syringe with a 23 gauge needle.

MRI Tracking Experiment. Experiments were performed using a vertical bore 11.7 T Bruker Avance imaging spectrometer with a microimaging gradient insert and 30 mm birdcage RF coil (Bruker Instruments, Billerica, MA). T1-weighted images were acquired using a 2D gradient echo sequence. The sequence parameters were: TR = 500ms and TE = 8.233ms, Field of View (FOV) 40 x 40mm, Matrix size 256 x 256, 30 consecutive coronal slice with slice thickness 0.5 mm. 4 averages were taken, with a scan time of 6 minutes, 24 seconds. To minimize motion artifacts, data acquisition was gated (i.e. synchronized to the respiratory signal). After injection, scans were acquired at 30 mins, 1.5 hrs, 3 hrs, 6 hrs, 12 hrs and 24 hrs. A control experiment was performed, in which PBS was injected with no peptide nanofibers. A total of 5 mice were used for this experiment.

Animal Models of AKI. All animals were cared for at Baylor College of Medicine and according to the AIACU and Principles of Laboratory Animal Care of the National Institute of Health. Generation of Rock1-/- mice was previously described.[68] Adult male C57BLKS mice (8 to 10 weeks old) were obtained commercially (Jackson Laboratory, Bar Harbor, ME). Mice received a single injection with 10 μg/g body wt of LPS (E. coli; List Laboratories, Campbell, CA) or sterile normal saline intraperitoneally.[42, 43, 45] For LPS-induced model of AKI, groups of 6 to 11 mice were randomly allocated to

individual groups. One group of mice was used as the control group. All other groups received a single intraperitoneal injection of LPS (10 μg/g body weight). In LPS-treated animals, mice were injected with 0.8 ml of isotonic saline intraperitoneally to prevent hypovolemia after 12 hours.[42] In experiments where the effect of preconditioned nanofibers was assessed, animals were given an injection of nanofibers (200 μL) intraperitoneally 1 hour after LPS injection. Mice were sacrificed 24 hours after LPS injection. Urine albumin and creatinine were determined using Albuwell M and Creatinine Assay (Exocell, Philadelphia). Kidney ischemia reperfusion (I-R) was performed in male C57BL/6 mice, aged 8 to 10 weeks, obtained from Jackson Laboratory.[61,62] Briefly, mice were anesthetized with intraperitoneal ketamine, had abdominal incisions, and then have both renal pedicles bluntly dissected. A microvascular clamp (Roboz) was placed on both renal pedicles for 30 minutes while the animal was kept at a constant temperature (37°C) and well hydrated. After ischemia, the clamps were removed, the wounds were sutured, and the animal was allowed to recover. Mice were randomly allocated into the following groups (n = 6): (1) sham; (2) I-R preconditioned nanofibers (100 μL) injected intraperitoneally 1 hour before induction of ischemia and at the time of reperfusion; and (3) I-R nonconditioned nanofibers (100 μL) injected intraperitoneally 1 hour before induction of ischemia and at the time of reperfusion. Mice were administered with 0.5 ml of isotonic saline intraperitoneally (preheated to 37°C) immediately after closure of abdomen, and sacrificed 24 hours after reperfusion. Serum creatinine and BUN were measured on obtained blood samples.

Detection of Apoptosis. Apoptotic cells were determined using an Apoptag

Fluorescein In Situ Apoptosis Detection Kit (TUNEL assay; Chemicon, Billerica, MA), and by quantifying cytoplasmic histone-associated DNA fragments detection (Cell Death Detection ELISA; Roche, Indianapolis), according to the manufacturers' instructions. Caspase-3 activation was assessed by caspase-3 activation assay (BD Biosciences, San Jose, CA).

In Situ Hybridization. In situ hybridization with an antisense PAI-1 riboprobe was performed as described previously.[69, 70] Total RNA from mouse lung was reverse-transcribed into cDNA using Superscript reverse transcriptase (Clontech) and random hexamers (Sigma). PCR amplification was performed using T7-tagged forward and SP6-tagged reverse primers to amplify a 848-bp fragment representing bases 663-1510 of the coding region of the murine PAI-1 gene. The PCR-amplified cDNA template was used for in vitro transcription of digoxygenin- labeled riboprobe using T7 RNA polymerase for the antisense probe and SP6 for the sense control probe.

Enzyme Cleavage Assays. Human recombinant osteopontin (1 μg, huOPN) mixed with 20 μL of nanofibers were cleaved by MMP3 (50 ng) in equal volume of cleavage buffer (200 mM NaCl, 50 mM Tris-HCl, pH 7.6, 5 mM CaCl2) for 10 minutes at 37°C as described previously[72]. The mixture of cleaved OPN fragments was separated on a 12.5% polyacrylamide gel under reducing conditions. The membrane was incubated in a combination of three primary anti-OPN antibodies, anti-OPN goat polyclonal antibody and two anti-OPN rabbit polyclonal antibodies, for 1 hour. Proteins were visualized with ECL Plus (GE Healthcare).

Statistical Analysis. All data are shown as mean ±SEM. Statistical significance was assessed by performing ANOVA followed by the Tukey-Kramer post hoc analysis for multiple comparisons using an α value of 0.05 in Graphpad Prism software (version 5.0; San Diego). Differences between paired means were assessed with the unpaired, two-tailed t-test.

Ethical Guidelines. All local and ethical guidelines of Rice University and Baylor College of Medicine were followed in the course of these experiments. Stem cells were transferred per agreement with Wisconsin Materials. Additionally, no materials involved in this study were used for commercial purposes.

References

(1) Hule, R. A.; Nagarkar, R. P.; Altunbas, A.; Ramay, H. R.; Branco, M. C.; Schneider, J. P.; Pochan, D. J. *Faraday Discuss.* **2008**, *139*, 251-264.

(2) Zhang, S. *Nat. Biotechnol.* **2003**, *21*, 1171-1178.

(3) Ellis-Behnke, R. G.; Liang, Y. X.; You, S. W.; Tay, D. K.; Zhang, S.; So, K. F.; Schneider, G. E. *Proc. Natl. Acad. Sci. U. S. A.* **2006**, *103*, 7530.

(4) Jung, J. P.; Jones, J. L.; Cronier, S. A.; Collier, J. H. *Biomaterials* **2008**, *29*, 2143-2151.

(5) Kisiday, J.; Jin, M.; Kurz, B.; Hung, H.; Semino, C.; Zhang, S.; Grodzinsky, A. J. *Proc. Natl. Acad. Sci. U. S. A.* **2002**, *99*, 9996-10001.

(6) Holmes, T. C.; de, L., S; Su, X.; Liu, G. S.; Rich, A.; Zhang, S. G. *Proc. Natl. Acad. Sci. U. S. A.* **2000**, *97*, 6728-6733.

(7) Branco, M. C.; Schneider, J. P. *Acta Biomater.* **2009**, *5*, 817-831.

(8) Branco, M. C.; Pochan, D. J.; Wagner, N. J.; Schneider, J. P. *Biomaterials* **2009**, *30*, 1339-1347.

(9) Naigai, Y.; Unsworth, L. D.; Koutsopoulos, S.; Zhang, S. *J. Controlled Release* **2006**, *115*, 18-25.

(10) Dong, H.; Paramonov, S. E.; Aulisa, L.; Bakota, E. L.; Hartgerink, J. D. *J. Am. Chem. Soc.* **2007**, *129*, 12468-12472.

(11) Rajagopal, K.; Lamm, M. S.; Haines-Butterick, L. A.; Pochan, D. J.; Schneider, J. P. *Biomacromolcules* **2009**, *10*, 2619-2625.

(12) Branco, M. C.; Nettesheim, F.; Pochan, D. J.; Schneider, J. P.; Wagner, N. J. *Biomacromolcules* **2009**, *10*, 1374-1380.

(13) Aulisa, L.; Dong, H.; Hartgerink, J. D. *Biomacromolecules* **2009**, *10*, 2694-2698.

(14) Ramachandran, S.; Tseng, Y.; Yu, Y. B. *Biomacromolcules* **2005**, *6*, 1316-1321.

(15) Gelain, F.; Bottai, D.; Vescovi, A.; Zhang, S. G. *PLoS One* **2006**, *1*, ARTN e119.

(16) Galler, K. M.; Aulisa, L.; Regan, K. R.; D'Souza, R. N.; Hartgerink, J. D. *J. Am. Chem. Soc.* **2010**, *132*, 3217-3223.

(17) Naskar, J.; Palui, G.; Banerjee, A. *J. Phys. Chem. B* **2009**, *113*, 11787-11792.

(18) Koutsopoulos, S.; Unsworth, L. D.; Naigai, Y.; Zhang, S. *Proc. Natl. Acad. Sci. U. S. A.* **2009**, *106*, 4623-4628.

(19) Webber, M. J.; Han, X.; Murthy, S. N.; Rajangam, K.; Stupp, S. I.; Lomasney, J. W. *J. Tissue Eng. Reg. M.* **2010**, *4*, 600-610.

(20) Emerich, D. F.; Mooney, D. J.; Storrie, H.; Babu, R. S.; Kordower, J. H. *Neurotox. Res.* **2010**, *17*, 66-74.

(21) Hsieh, P. C. H.; Davis, M. E.; Gannon, J.; MacGillivray, C.; Lee, R. T. *J. Clin. Invest.* **2006**, *116*, 237-248.

(22) Davis, M. E.; Hsieh, P. C. H.; Takahashi, T.; Song, Q.; Zhang, S. G.; Kamm, R. D.; Grodzinsky, A. J.; Anversa, P.; Lee, R. T. *Proc. Natl. Acad. Sci. U. S. A.* **2006**, *103*, 8155-8160.

(23) Haines-Butterick, L.; Rajagopal, K.; Branco, M.; Salick, D.; Rughani, R.; Pilarz, M.; Lamm, M. S.; Pochan, D. J.; Schneider, J. P. *Proc. Natl. Acad. Sci. U. S. A.* **2007**, *104*, 7791-7796.

(24) Guo, J. K.; Cantley, L. G. *Annu. Rev. Physiol.* **2010**, *72*, 357-376.

(25) Herrera, M. B.; Bussolati, B.; Bruno, S.; Morando, L.; Mauriello-Romanazzi, G.; Sanavio, F.; Stamenkovic, I.; Biancone, L.; Camussi, G. *Kidney. Int.* **2007**, *72*, 430-441.

(26) Humphreys, B. D.; Valerius, M. T.; Kobayashi, A.; Mugford, J. W.; Soeung, S.; Duffield, J. S.; McMahon, A. P.; Bonventre, J. V. *Cell Stem Cell* **2008**, *2*, 284-291.

(27) Ikarashi, K.; Li, B.; Suwa, M.; Kawamura, K.; Morioka, T.; Yao, J.; Khan, F.; Uchiyama, M.; Oite, T. *Kidney. Int.* **2005**, *67*, 1925-1933.

(28) Kale, S.; Karihaloo, A.; Clark, P. R.; Kashgarian, M.; Krause, D. S.; Cantley, L. G. *J. Clin. Invest.* **2003**, *112*, 42-49.

(29) Lin, F. M.; Moran, A.; Igarashi, P. *J. Clin. Invest.* **2005**, *115*, 1756-1764.

(30) Lin, F. M.; Cordes, K.; Li, L. H.; Hood, L.; Couser, W. G.; Shankland, S. J.; Igarashi, P. *J. Am. Soc. Nephrol.* **2003**, *14*, 1188-1199.

(31) Maeshima, A.; Yamashita, S.; Nojima, Y. *J. Am. Soc. Nephrol.* **2003**, *14*, 3138-3146.

(32) Morigi, M.; Imberti, B.; Zoja, C.; Corna, D.; Tomasoni, S.; Abbate, M.; Rottoli, D.; Angioletti, S.; Benigni, A.; Perico, N.; Alison, M.; Remuzzi, G. *J. Am. Soc. Nephrol.* **2004**, *15*, 1794-1804.

(33) Poulsom, R.; Forbes, S. J.; Hodivala-Dilke, K.; Ryan, E.; Wyles, S.; Navaratnarasah, S.; Jeffery, R.; Hunt, T.; Alison, M.; Cook, T.; Pusey, C.; Wright, N. A. *J. Pathol.* **2001**, *195*, 229-235.

(34) Sugimoto, H.; Mundel, T. M.; Sund, M.; Xie, L.; Cosgrove, D.; Kalluri, R. *Proc. Natl. Acad. Sci. U. S. A.* **2006**, *103*, 7321-7326.

(35) Bi, B.; Schmitt, R.; Israilova, M.; Nishio, H.; Cantley, L. G. *J. Am. Soc. Nephrol.* **2007**, *18*, 2486-2496.

(36) Imberti, B.; Morigi, M.; Tomasoni, S.; Rota, C.; Corna, D.; Longaretti, L.; Rottoli, D.; Valsecchi, F.; Benigni, A.; Wang, J.; Abbate, M.; Zoja, C.; Remuzzi, G. *J. Am. Soc. Nephrol.* **2007**, *18*, 2921-2928.

(37) Togel, F.; Weiss, K.; Yang, Y.; Hu, Z. M.; Zhang, P.; Westenfelder, C. *Am. J. Physiol. Renal* **2007**, *292*, F1626-F1635.

(38) Togel, F.; Isaac, J.; Hu, Z. M.; Weiss, K.; Westenfelder, C. *Kidney Int.* **2005**, *67*, 1772-1784.

(39) Ruoslahti, E.; Pierschbacher, M. D. *Science* **1987**, *238*, 491-497.

(40) Burdick, J. A.; Anseth, K. S. *Biomaterials* **2002**, *23*, 4315-4323.

(41) Zou, D. W.; Tie, Z. X.; Lu, C. M.; Qin, M.; Lu, X. M.; Wang, M.; Wang, W.; Chen, P. *Biopolymers* **2010**, *93*, 318-329.

(42) Faul, C.; Donnelly, M.; Merscher-Gomez, S.; Chang, Y. H.; Franz, S.; Delfgaauw, J.; Chang, J. M.; Choi, H. Y.; Campbell, K. N.; Kim, K.; Reiser, J.; Mundel, P. *Nat. Med.* **2008**, *14*, 931-938.

(43) Wei, C.; Moeller, C. C.; Altintas, M. M.; Li, J.; Schwarz, K.; Zacchigna, S.; Xie, L.; Henger, A.; Schmid, H.; Rastaldi, M. P.; Cowan, P.; Kretzler, M.; Parrilla, R.; Bendayan, S.; Gupta, V.; Nikolic, B.; Kalluri, R.; Carmeliet, P.; Mundel, P.; Reiser, J. *Nat. Med.* **2008**, *14*, 55-63.

(44) Zahedi, K.; Barone, S.; Kramer, D. L.; Amlal, H.; Alhonen, L.; Janne, J.; Porter, C. W.; Soleimani, M. *Am. J. Physiol. Cell Physiol.* **2010**, *299*, C164-C174.

(45) Wu, L. P.; Tiwari, M. M.; Messer, K. J.; Holthoff, J. H.; Gokden, N.; Brock, R. W.; Mayeux, P. R. *Am. J. Physiol. Renal* **2007**, *292*, F261-F268.

(46) Bannerman, D. D.; Goldblum, S. E. *Am. J. Physiol. Lung Cell. Mol. Physiol.* **2003**, *284*, L899-L914.

(47) Bannerman, D. D.; Sathyamoorthy, M.; Goldblum, S. E. *J. Biol. Chem.* **1998**, *273*, 35371-35380.

(48) Cunningham, P. N.; Dyanov, H. M.; Park, P.; Wang, J.; Newell, K. A.; Quigg, R. J. *J. Immunol.* **2002**, *168*, 5817-5823.

(49) Jho, D.; Mehta, D.; Ahmmed, G.; Gao, X. P.; Tiruppathi, C.; Broman, M.; Malik, A. B. *Circul. Res.* **2005**, *96*, 1282-1290.

(50) Caravan, P.; Ellison, J. J.; McMurry, T. J.; Lauffer, R. B. *Chem. Rev.* **1999**, *99*, 2293-2352.

(51) Pautler, R. G. *Physiology* **2004**, *19*, 168-175.

(52) Pautler, R. G.; Mongeau, R.; Jacobs, R. E. *Magn. Reson. Med.* **2003**, *50*, 33-39.

(53) Kim, S. H.; Csaky, K. G.; Wang, N. S.; Lutz, R. J. *Pharm. Res.* **2008**, *25*, 512-520.

(54) Chen, X. M.; Astary, G. W.; Sepulveda, H.; Mareci, T. H.; Sarntinoranont, M. *Magn. Reson. Imaging* **2008**, *26*, 1433-1441.

(55) Guo, R. Q.; Wang, Y.; Minto, A. W.; Quigg, R. J.; Cunningham, P. N. *J. Am. Soc. Nephrol.* **2004**, *15*, 3093-3102.

(56) Van, H., D; Passier, R.; Ward-Van, O., D; Pinkse, M. W. H.; Heck, A. J. R.; Mummery, C. L.; Krijgsveld, J. *Mol. Cell. Proteomics* **2006**, *5*, 1261-1273.

(57) Maeshima, A.; Zhang, Y. Q.; Nojima, Y.; Naruse, T.; Kojima, I. *J. Am. Soc. Nephrol.* **2001**, *12*, 1685-1695.

(58) Nakamura, A.; Mori, Y.; Hagiwara, K.; Suzuki, T.; Sakakibara, T.; Kikuchi, T.; Igarashi, T.; Ebina, M.; Miyazaki, J.; Takai, T.; Nukiwa, T.; Nukiwa, T. *J. Exp. Med.* **2003**, *197*, 669-674.

(59) Ohashi, K.; Iwatani, H.; Kihara, S.; Nakagawa, Y.; Komura, N.; Fujita, K.; Maeda, N.; Nishida, M.; Katsube, F.; Shimomura, I.; Ito, T.; Funahashi, T. *Arterio. Thromb. Vasc. Biol.* **2007**, *27*, 1910-1917.

(60) Cao, H. Q.; Liu, T.; Chew, S. Y. *Adv. Drug Del. Rev.* **2009**, *61*, 1055-1064.

(61) Langley, R. R.; Ramirez, K. M.; Tsan, R. Z.; Van, A., M; Nilsson, M. B.; Fidler, I. J. *Cancer Res.* **2003**, *63*, 2971-2976.

(62) Saleem, M. A.; O'Hare, M. J.; Reiser, J.; Coward, R. J.; Inward, C. D.; Farren, T.; Xing, C. Y.; Ni, L.; Mathieson, P. W.; Mundel, P. *J. Am. Soc. Nephrol.* **2002**, *13*, UNSP 1046-6673/1303-0630.

(63) Mundel, P.; Reiser, J.; Borja, A. Z. M.; Pavenstadt, H.; Davidson, G. R.; Kriz, W.; Zeller, R. *Exp. Cell. Res.* **1997**, *236*, 248-258.

(64) Williams, R. L.; Hilton, D. J.; Pease, S.; Willson, T. A.; Stewart, C. L.; Gearing, D. P.; Wagner, E. F.; Metcalf, D.; Nicola, N. A.; Gough, N. M. *Nature* **1988**, *336*, 684-687.

(65) Ozolek, J. A.; Jane, E. P.; Krowsoski, L.; Sammak, P. J. *Stem Cells Dev.* **2007**, *16*, 403-412.

(66) Cheng, J.; Dutra, A.; Takesono, A.; Garrett-Beal, L.; Schwartzberg, P. L. *Genesis* **2004**, *39*, 100-104.

(67) Hancock, C. R.; Wetherington, J. P.; Lambert, N. A.; Condie, B. G. *Biochem. Biophys. Res. Commun.* **2000**, *271*, 418-421.

(68) Zhang, Y. M.; Bo, J.; Taffet, G. E.; Chang, J.; Shi, J.; Reddy, A. K.; Michael, L. H.; Schneider, M. D.; Entman, M. L.; Schwartz, R. J.; Wei, L. *FASEB J.* **2006**, *20*, 916-925.

(69) Wang, X. L.; Sutton, V. R.; Peraza-Llanes, J. O.; Yu, Z. Y.; Rosetta, R.; Kou, Y. C.; Eble, T. N.; Patel, A.; Thaller, C.; Fang, P.; Van, d. V., IB. *Nat. Genet.* **2007**, *39*, 836-838.

(70) Jenkins, Z. A.; van, K., M; Morgan, T.; Jeffs, A.; Fukuzawa, R.; Pearl, E.; Thaller, C.; Hing, A. V.; Porteous, M. E.; Garcia-Minaur, S.; Bohring, A.; Lacombe, D.; Stewart, F.; Fiskerstrand, T.; Bindoff, L.; Berland, S.; Ades, L. C.; Tchan, M.; David, A.; Wilson, L. C.; Hennekam, R. C. M.; Donnai, D.; Mansour, S.; Cormier-Daire, V.; Robertson, S. P. *Nat. Genet.* **2009**, *41*, 95-100.

(71) Long, J. Y.; Wang, Y.; Wang, W. J.; Chang, B. H. J.; Danesh, F. R. *J. Biol. Chem.* **2010**, *285*, 23455-23463.

(72) Agnihotri, R.; Crawford, H. C.; Haro, H.; Matrisian, L. M.; Havrda, M. C.; Liaw, L. *J. Biol. Chem.* **2001**, *276*, 28261-28267.

Chapter 5: Multidomain Peptides as Biocompatible Single-Walled Carbon Nanotube Surfactants·

Single-walled carbon nanotubes (SWCNTs) are an allotrope of carbon, similar to graphene in that their structure is composed entirely of sp^2 carbon-carbon bonds. They are excellent thermal conductors and stronger than steel, making them attractive for use in construction of electronic devices[1] and conductive polymers.[2] Their high aspect ratio and inert nature also make them well-suited for use in biological environments.[3]

Single-walled carbon nanotubes have also been recognized as exceptional near-IR fluorophores. They display unexcelled photostability,[4, 5] high optical anisotropy,[6] large Stokes shifts,[7] and an absence of fluorescence intermittency.[4, 8] This unique combination of optical properties is not found in other emissive labels such as quantum dots or fluorescent dyes, making SWCNTs uniquely promising for applications as fluorescent markers and biosensors.[9, 10] Although the maximum near-IR fluorescence quantum yields of SWCNTs are apparently only of order 10%,[11-13] their large absorption cross-sections and unusual emission wavelengths allow highly sensitive optical detection in biological environments.[9, 14-17] However, certain challenges related to the nanotube surface coating need to be addressed before SWCNTs can realize their potential as biomarkers and sensors.

· This chapter is based on two publications:
Dmitri A. Tsyboulski, Erica L. Bakota, Leah S. Witus, John-David R. Rocha, Jeffrey D. Hartgerink and R. Bruce Weisman. Self-Assembling Peptide Coatings Designed for Highly Luminescent Suspension of Single-Walled Carbon Nanotubes. *J. Am. Chem. Soc.*, **2008**, 130 (50), pp 17134–17140.

Erica L. Bakota, Lorenzo Aulisa, Dmitri A. Tsyboulski, R. Bruce Weisman and Jeffrey D. Hartgerink. Multidomain Peptides as Single-Walled Carbon Nanotube Surfactants in Cell Culture. *Biomacromolecules*, **2009**, 10 (8), pp 2201–2206.

A. The Case for Biocompatible SWCNT Surfactants

The most obvious of these challenges is nanotube solubility. SWCNTs are highly hydrophobic and readily aggregate into nonemissive bundles, so they must be dispersed as individuals in order to provide the water compatibility needed for biological applications. Although covalent derivatization of SWCNTs has produced stable aqueous SWCNT solutions,[18] chemical modification of the SWCNT sidewall locally perturbs the sp^2 structure of the tube, compromising the electronic and optical properties that make SWCNTs unique. Therefore, for many applications, noncovalent functionalization of SWCNTs is preferable. This usually involves processing the aggregated raw SWCNTs through sonication in surfactant solution followed by centrifugation.[19, 20] This process yields stable dispersions of individualized, fluorescent SWCNTs noncovalently coated by surfactant. However, the choice of surfactant coating greatly affects the suitability of these dispersions for biological fluorescence applications.

An appropriate noncovalent SWCNT surfactant should accomplish four objectives: First, the coating must confer low toxicity and high biocompatibility. Second, it should permit the SWCNTs to fluoresce with efficiencies comparable to those of pristine SWCNTs suspended in air or isolated in selected anionic surfactants.[11, 12] Third, the coating should be stable against displacement or disruption in biological environments, possibly through covalent cross-linking to form a shell around the nanotube.[17, 21] Finally, the SWCNT coating molecules should provide sites allowing chemical linkage of agents designed for biological targeting or specialized sensing.[22] It is clearly challenging to meet all of these requirements at once.

The first class of surfactants used to solubilize SWCNTs was the class of traditional anionic surfactants, such as sodium dodecylsulfate (SDS) and sodium dodecylbenzenesulfonate (SDBS). While these detergents suspend nanotubes well, they are highly toxic to mammalian cells due to surfactant-assisted dissolution of the lipid bilayer of the cell membrane.[23, 24] This violates the first goal of the desired SWCNT surfactant.

This apparent toxicity sparked the development of many biocompatible agents for the noncovalent suspension of SWCNTs. Until recently, the choice of biocompatible surfactants was limited to only a few materials, including Pluronics (synthetic nonionic surfactants),[9, 15] single-stranded DNA (ssDNA),[25] and bovine serum albumin (BSA).[26] However, the Pluronics do not easily permit selective chemical modifications that would allow the surfactant to perform other duties *in vivo*, such as cell-specific targeting. Furthermore, Pluronics, ssDNA, and BSA dampen fluorescence emission from carbon nanotubes. Therefore, to effectively and safely introduce disaggregated pristine SWCNTs into biological systems, new biocompatible surfactants are needed.

Peptides are another class of materials that have shown promise as SWCNT surfactants.[27-33] Peptides are particularly promising because they are relatively simple to synthesize, and their versatility allows them to form a variety of engineered structures with tailored functionalities. They are also generally less cytotoxic than detergents such as SDBS and are potentially able to be degraded by cellular enzymes.

However, except in one case involving limited studies of bulk fluorescence,[33] the emissive properties of SWCNTs in these peptide coatings have not been reported. To date, the rational design of peptide SWCNT coatings has focused on maximizing the

coating's affinity for the nanotube surface in order to achieve the greatest capacity for suspending SWCNTs in aqueous media.[28-35] This approach is not necessarily, however, directed at maximizing the emission efficiency of the suspended nanotubes. In this work, the fluorescence properties of SWCNTs suspended in different environments were examined, and it was shown that the surfactant exerts a profound influence on SWCNT emission efficiency. Furthermore, multidomain peptides appear to be a promising avenue for suspending single-walled carbon nanotubes.

The influence of coating material on intrinsic SWCNT fluorescence efficiency is difficult to assess, because the brightness of a bulk sample will depend on the total nanotube concentration in suspension and the degree to which the suspended nanotubes are individualized (bundling quenches their emission),[36, 37] in addition to the intrinsic coating-dependent fluorescence efficiency. We therefore applied near-IR fluorescence microscopy to make comparative brightness measurements on individual SWCNTs in dilute samples that differ only in their coating material. Figure 5.1 shows near-IR fluorescence images of dilute SWCNT suspensions in SDBS, Pluronic F127, ss-DNA, and BSA, obtained using fixed wavelength, circularly polarized excitation. Individual nanotubes in these images differ in apparent brightness because of the distribution of lengths, the distribution of (n,m) structures (governing absorptivity at the excitation wavelength), and the distribution of elevation angles relative to the observation direction.[38, 39]

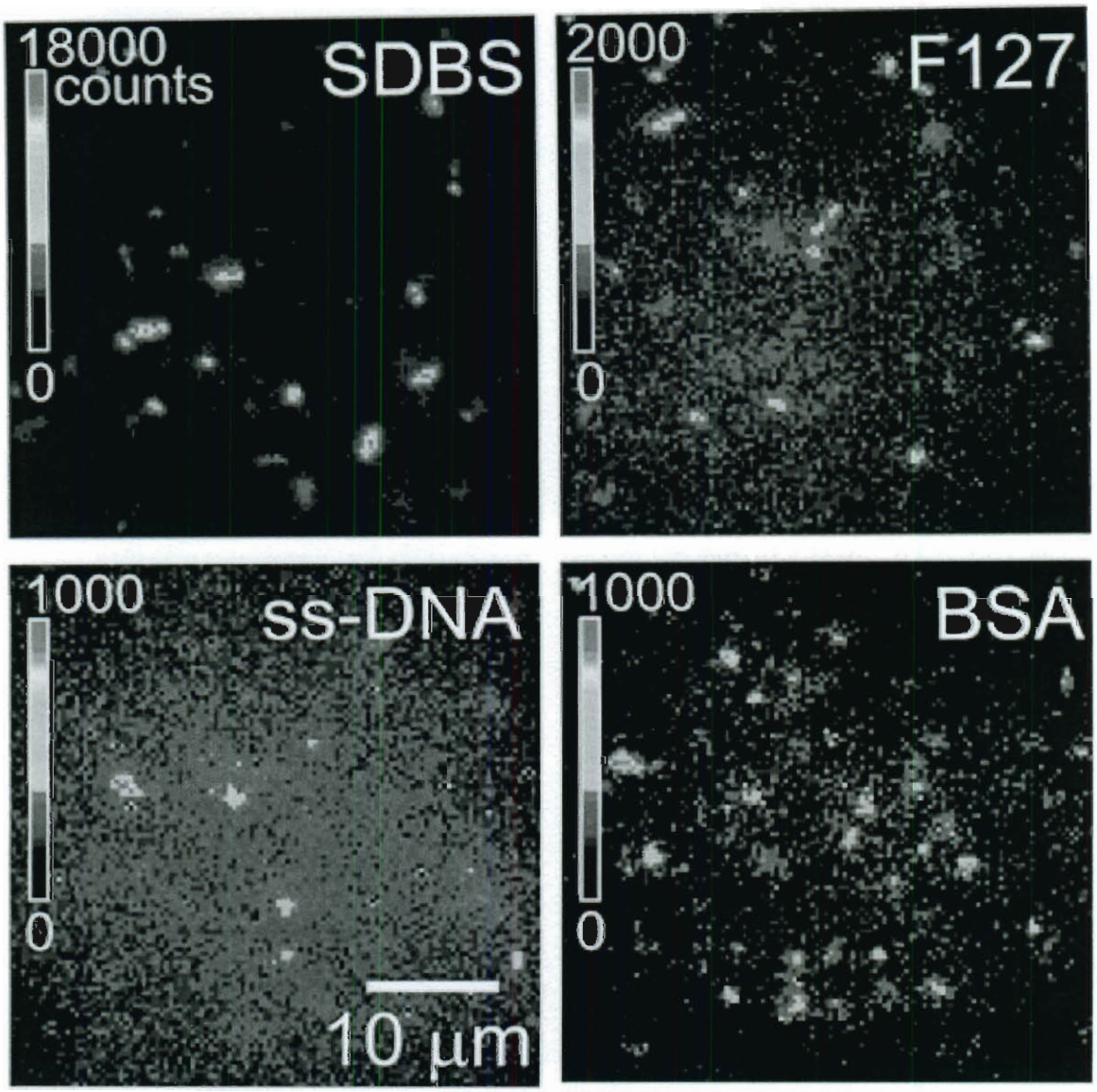

Figure 5.1. Near-IR fluorescence images of SWCNTs suspensions in aqueous SDBS, Pluronic F127, ss-DNA, and BSA. All images were recorded under identical conditions (excitation wavelength 658 nm, excitation intensity ~800 W/cm^2, circular polarization, frame acquisition time 50 ms). Figure by Dmitri Tsyboulski.

Nevertheless, it is clear from the differences in intensity scales that the ionic surfactant SDBS (which is not biocompatible) allows by far the strongest near-IR emission within this group. Individual SWCNTs in Pluronic suspension are at least a factor of 10 less bright than those suspended in SDBS, while SWCNTs in ss-DNA or BSA show even

weaker emission. Pluronic and BSA coatings have the additional drawback of being vulnerable to displacement or coadsorption by proteins.[14]

B. $K_m(QL)_nK_m$ Series

Here we have examined a series of multidomain peptides as SWCNT surfactants. Multidomain peptides form nanofibers in aqueous solution, and these nanofibers have dimensions on the same size scale as SWCNTs, making them a promising lead in the search for suitable biocompatible surfactants. Initially, nine peptide sequences were used in this study to suspend SWCNTs. These are listed in Table 5.1 along with their simple designations: A – $K_7(QL)_6K_7$, B – $K_6(QL)_6K_6$, C – $K_5(QL)_6K_5$, D – $K_4(QL)_6K_4$, E – $K_3(QL)_6K_3$, F – $K_2(QL)_6K_2$, G – $K_2(QL)_5K_2$, H – $K_2(QL)_4K_2$, and I – $K_2(QL)_3K_2$. Nanotubes were suspended in peptide solutions by placing ~1 mg SWCNTs in an Eppendorf vial. A 1 wt% solution of peptide was prepared and pipetted directly on top of the dry SWCNTs. The vial was capped, shaken briefly, and tip-sonicated, followed by 3 rounds of centrifugation. After discarding the pellets, their absorption and fluorescence spectra of the resulting peptide-SWCNT solutions were recorded. We consider the total suspended nanotube concentration to be proportional to the area under the measured absorbance spectrum, integrated between 500 and 1350 nm. The spectrally integrated fluorescence emission instead measures the relative concentrations of individually suspended nanotubes multiplied by their intrinsic fluorescence efficiencies in those suspending peptides. We found that SWCNT samples suspended in peptides E, F, and G yielded the highest concentrations of suspended nanotubes and also the highest total

emission intensities. The top frame of Figure 5.2 displays these three strongest emission spectra, while the bottom frame compares magnitudes of the spectrally integrated emission and absorption signals for all nine peptide coatings. We note that many of these magnitudes varied substantially from run to run, probably because of irreproducibility in the sonication of small volumes and in sampling the SWCNT raw material. Nevertheless, within the series of peptides, E, F, and G consistently gave the most concentrated SWCNT suspensions, with typical peak absorbance values exceeding 1 per cm. These samples appeared stable over periods of a few months, whereas the other peptide suspensions tended to form visible aggregates within days or weeks.

Peptide	Sequence	Secondary Structure	Forms Nanofibers	Solubilizes SWCNTs
A	$K_7(QL)_6K_7$	Random coil	No	No
B	$K_6(QL)_6K_6$	Random coil	No	No
C	$K_5(QL)_6K_5$	Random coil	No	No
D	$K_4(QL)_6K_4$	Weak helix	No	Weakly
E	$K_3(QL)_6K_3$	β -sheet	Yes	Yes
F	$K_2(QL)_6K_2$	β -sheet	Yes	Yes
G	$K_2(QL)_5K_2$	β - sheet	Yes	Yes
H	$K_2(QL)_4K_2$	Random coil	No	No
I	$K_2(QL)_3K_2$	Random coil	No	No
J	$K_2(QF)_5K_2$	β – sheet	?	Yes

Table 5.1. Multidomain peptides used as SWCNT surfactants.

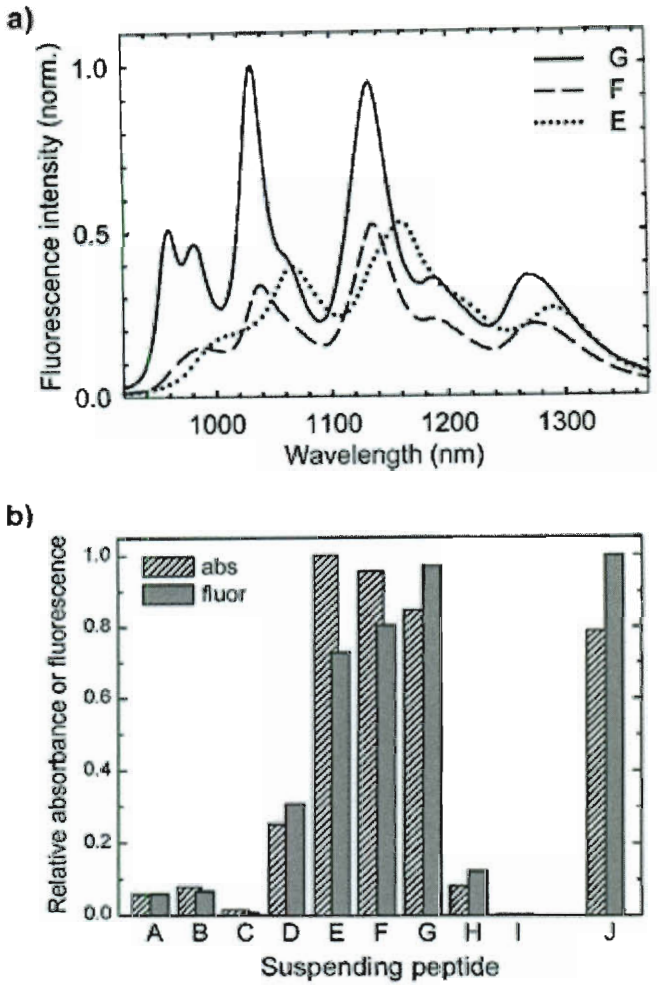

Figure 5.2. a) Fluorescence emission spectra from bulk SWCNT samples suspended in peptide coatings E, F, and G. The spectra have been normalized to the most intense peak in peptide G. b) Average spectrally integrated fluorescence emission and absorbance for bulk SWCNT samples suspended in the family of peptide coatings A–I, and in peptide J (normalized to the maximum values). Figure by Dmitri Tsyboulski.

Figure 5.3 a,b,c,d shows 2D excitation–emission matrices of SWCNTs suspended in SDBS and in peptides E, F, and G. These data were recorded by scanning the excitation wavelength from 520 to 850 nm and the emission wavelength from 900 to 1300 nm. The excitation–emission maps reveal distinct peaks that can readily be assigned to particular (*n*,*m*) species by reference to established spectral studies of SWCNTs in aqueous sodium dodecylsulfate (SDS) suspension.[7, 40] SDS is another anionic surfactant that is used

frequently to solubilize SWCNTs. However, SDS is also highly toxic to cells, causing dissolution of the lipid bilayer of the cell membrane. We note that the SWCNT spectral peak positions and widths depend significantly on suspending agent. Excitation and fluorescence peaks corresponding to the second (E_{22}) and first (E_{11}) van Hove transitions of disaggregated SWCNTs are progressively shifted to longer wavelengths in peptides G, F, and E as compared to the peak positions in aqueous SDBS. It is often considered that such red shifts arise from more polarizable nanotube environments.[20, 41-43] The E_{11} fluorescence bands also broaden progressively for SWCNTs suspended in peptides G, F, and E. This broadening is illustrated in Figure 5.3 f, which shows bulk emission spectra near the (6,5) peak. Using standard peak-fitting procedures, we deconvoluted the overlapping emission features and deduced (6,5) spectral line widths of ~200, 240, 320, and 480 cm^{-1}, respectively, in SDBS and peptides G, F, and E. As expected, the corresponding E_{22} excitation profiles shown in Figure 5.3 e have much smaller variations because those spectral widths arise from relaxation processes that are internal to the nanotubes and relatively insensitive to environment.

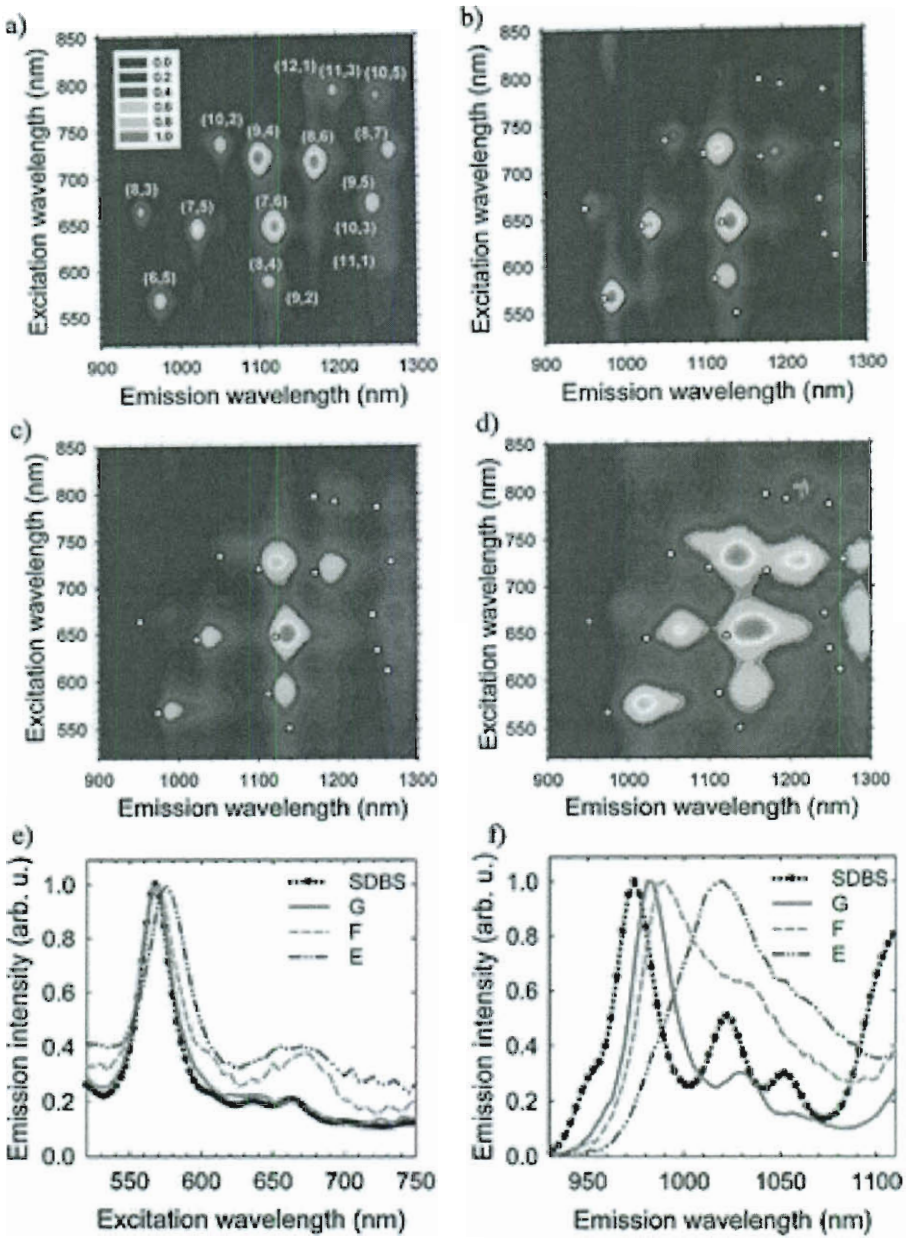

Figure 5.3. 2D excitation−emission photoluminescence maps of SWCNTs suspended in a) SDBS; b) Peptide G; c) Peptide F; d) Peptide E. White spots in (b, c, d) mark peak positions of SWCNTs in aqueous SDBS. e,f) Excitation and emission spectral profiles near (6,5) SWCNT peaks in various surfactants. Figure by Dmitri Tsyboulski.

It has been suggested that SWCNT emissive quantum yields also depend on coating.[20] However, the influence of SWCNT/surfactant interactions on fluorescence efficiency is not yet well documented or understood. Bulk spectrofluorimetric techniques

do not provide a reliable tool for such quantitative comparisons, because even when the fluorescence signals of bulk SWCNT suspensions are normalized to the mass of suspended carbon in the sample, the results can be substantially influenced by small nanotube bundles that may remain after ultracentrifugation. As was recently demonstrated by Crochet et al.,[36] further purification of SWCNT suspensions by a density gradient fractionation technique can give a ~20-fold increase in the fluorescence signal per unit of SWCNT mass.

An incisive method for comparing emission efficiencies of SWCNTs is to measure the fluorescence of individual nanotubes.[12] Because energy transfer to metallic SWCNTs tends to make nanotube bundles nonemissive,[19] their presence is unlikely to interfere with such measurements. A near-IR fluorescence microscope/spectrometer was used to capture emission images of dilute, freshly prepared suspensions of SWCNTs in peptides E, F, and G (Figure 5.4). These were recorded under the same experimental conditions as the data of Figure 5.1. It was found qualitatively that SWCNTs coated with peptide G displayed significantly brighter emission than those suspended in peptide E, peptide F, Pluronic, ss-DNA, or BSA.

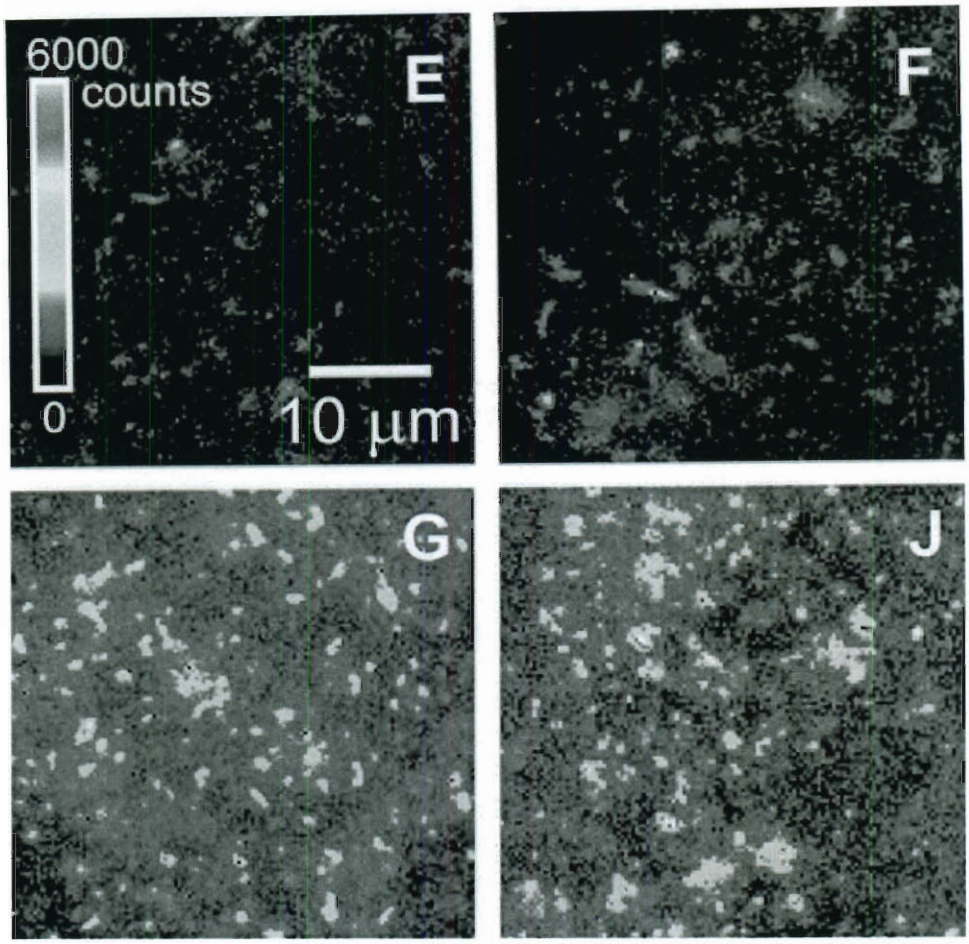

Figure 5.4. Near-IR fluorescence images of SWCNTs suspended in peptides E, F, G, and J. Images were recorded under identical conditions (658 nm excitation, ~800 W/cm^2 excitation intensity, 50 ms image acquisition time) and plotted with the same false-color intensity scale. Figure by Dmitri Tsyboulski.

To quantify these differences in emission efficiencies, it was necessary to avoid the complicating effects of sample heterogeneity in length, (*n*,*m*) structure, orientation, and defect density. This was achieved through measurements on individual SWCNTs in aqueous suspension that were selected to meet several criteria: length greater than 2 μm (to allow optical resolution); low defect density (estimated from uniform emission along the nanotube length); E_{11} peak spectral position matching the value found in bulk fluorescence spectroscopy for a known (*n*,*m*) species; and free motion indicating that the SWCNT was not attached to a glass surface.

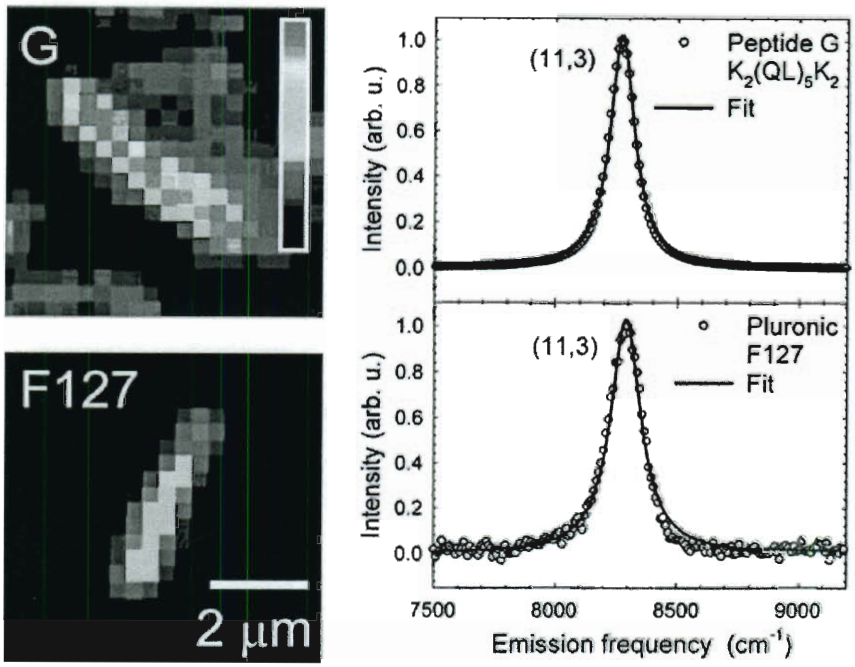

Figure 5.5. Comparison of emission intensities and spectra of SWCNTs in different surfactants. Near-IR fluorescence images of individual (11,3) nanotubes suspended in peptide G (top) and Pluronic F127 (bottom) recorded under the same experimental conditions and plotted using the same false-color intensity scale. Figure by Dmitri Tsyboulski.

Figure 5.5 shows images and emission spectra of such selected nanotubes coated by peptide G and Pluronic F127. Using the method and apparatus described previously,[12, 44] we measured the spatially and spectrally integrated emission signal from each nanotube with calibrated excitation intensity and calibrated detection sensitivity to find the absolute product of SWCNT absorption cross section σ and fluorescence quantum yield Φ_{Fl}. This product, $\sigma\,\Phi_{Fl}$, is the fluorescence action cross section. For each SWCNT coating studied here, we analyzed at least 10 nanotubes of various structural (*n*,*m*)-types to obtain the results given in Table 2 and Figure 5.6. Table 5.2 shows that the intrinsic brightness of individual SWCNTs is significantly affected by the surfactant coating. Using the available data, we computed the intrinsic brightness of each coating relative to that in SDBS by averaging the measured ratios of $\sigma(\lambda_{22})\Phi_{Fl}$ for corresponding (*n*,*m*) species. (λ_{22}

denotes the E_{22} peak wavelength.) The resulting relative fluorimetric brightness values, which are listed in the last row of Table 5.2, range from 0.05 to 0.46. Notably, these values are strongly correlated with the spectral line widths of the near-IR emission bands, as will be discussed below.

	$\sigma(\lambda_{22}) \times \Phi_{Fl}$ (10^4 cm^2/mol C); (number of SWCNTs measured)					
SWCNT species	**SDBS**	**$K_3(QL)_6K_3$ (E)**	**$K_2(QL)_6K_2$ (F)**	**$K_2(QL)_5K_2$ (G)**	**$K_2(QF)_5K_2$ (J)**	**Pluronic F127**
(8,3)	21	1.2 (1)			8.9 (2)	
(7,5)	19	0.76 (3)		5.1 (2)	5.8 (1)	3.1 (1)
(7,6)	14	0.63 (4)			4.5 (2)	2.0 (2)
(10,2)	27			9.8 (3)	21 (7)	
(12,1)	17	0.98 (3)	1.8 (1)			1.5 (1)
(11,3)	18		1.7 (4)	3.3 (5)		1.5 (4)
(10,5)	12		1.5 (4)			0.80 (3)
(9,7)	10		1.1 (1)			0.83 (1)
Relative fluorimetric brightness	1	0.050 ± 0.009	0.11 ± 0.01	0.32 ± 0.09	0.46 ± 0.22	0.13 ± 0.04

Table 5.2. Fluorescence action cross-sections of selected SWCNT species in various surfactants.

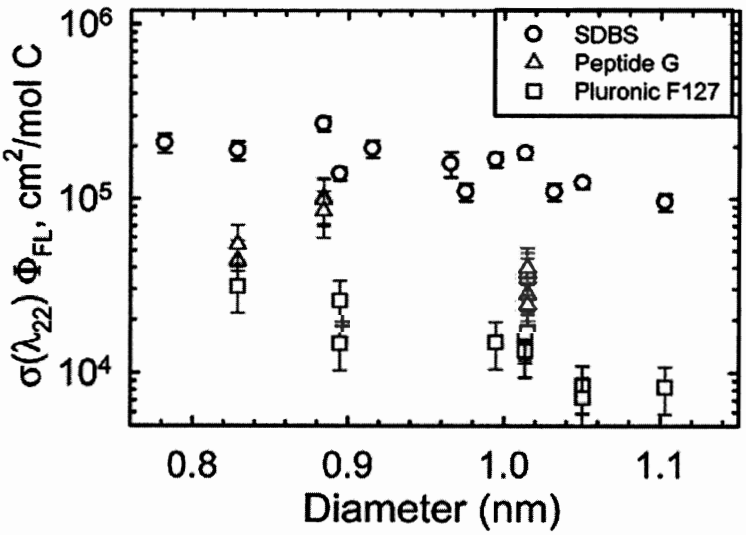

Figure 5.6. Measured fluorescence action cross sections of selected SWCNT structures suspended in aqueous SDBS (○), peptide $K_2(QL)_5K_2$ (G) (△), and Pluronic F127 (□). Data for SWCNTs in SDBS are taken from reference 12. Figure by Dmitri Tsyboulski.

It is interesting to examine the relationship between the ability of a peptide to self-assemble into nanofibers and its ability to individually suspend and allow emission from SWCNTs. Figure 5.2 illustrates that peptides E, F, and G are the ones within the $K_n(QL)_mK_n$ series most effective in suspending SWCNTs. Interestingly, these peptides are also the only ones that can assemble into nanofibers. $K_2(QL)_6K_2$ (peptide F) forms exclusively β-sheet nanofibers ~100−150 nm in length, while $K_3(QL)_6K_3$ (peptide E) and $K_2(QL)_5K_2$ (peptide G) self-assemble into mixtures of nanofibers and micelles of various lengths and sizes. This behavior is illustrated by the cryo-TEM images of Figure 5.7 a,b,c, which were acquired from solutions of peptides E, F and G without nanotubes. Figure 5.7 d,e,f shows corresponding cryo-TEM images for these peptides in the presence of SWCNTs. It can be deduced that the added SWCNTs act as templates for peptide self-assembly. Frame 5.7e clearly shows a number of nanotubes visible as extended structures with lengths of ~300 nm or more, along with shorter fibrils composed of self-assembled β-sheets of peptide F as formed in the absence of SWCNTs. Figure 5.7 d and f show that the peptides E and G adsorb onto and suspend SWCNTs in preference to forming fibrils and empty micelles. The peptides most effective at SWCNT suspension seem to be those that have some tendency to self-assemble in the absence of nanotubes. Although the geometry of peptide F is ideal for forming independently self-assembling nanofibers, the geometrical requirements for wrapping a SWCNT are apparently somewhat different and favor peptide G, which has a slightly shorter amphiphilic region. This selectivity between closely related peptide sequences also demonstrates that these peptides are not solubilizing the nanotubes as a simple amphiphilic surfactant. Instead, the peptides

interact with the nanotubes in a more specific fashion in which their tendency to anisotropically self-assemble is reinforced by the presence of the SWCNT.

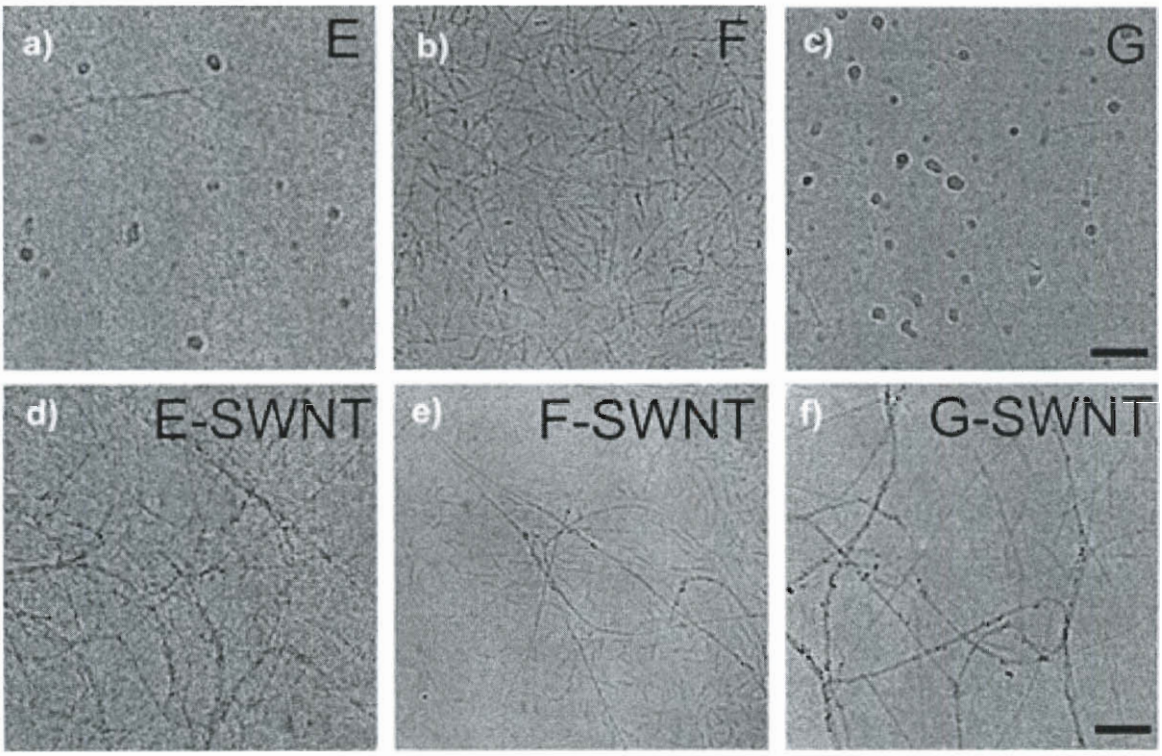

Figure 5.7. Cryo-TEM images of peptide solution samples. a, b, c) Peptides E, F, and G peptides without SWCNTs. d, e, f) Peptides E, F, and G with added SWCNTs. Scale bars are 100 nm.

Further insights into the nanotube-peptide interface can be obtained from optical measurements, because nanotube spectral peak positions reflect the local dielectric environment.[41-43] The broadened near-IR emission features found for SWCNTs coated by peptides E and F suggest a nanotube environment that is non-uniform and imperfect. By contrast, the sharper spectral features observed using peptide G indicate a more uniform coating morphology.

Our findings suggest a general principle useful for developing high-performance SWCNT-based fluorescent labels and sensors. Biopolymers with tendencies to self-

assemble into extended supramolecular structures are promising candidates for noncovalently suspending SWCNTs and preserving their optical properties. However, the best results are found using peptides (such as G) that are imperfect assemblers in the absence of an external template such as a SWCNT. Peptide-based SWCNT coatings have historically been designed to provide the highest water solubility of carbon nanotubes. This approach should optimize the peptide's ability to suspend individual nanotubes in aqueous environments but will not necessarily achieve the goal of maximizing SWCNT fluorescence intensity, nor will it necessarily incorporate bio-targeting ability via cell-signaling sequences in the peptide.

C. Effects of Peptides on Fluorescence Emission Efficiency

Within the $K_m(QL)_nK_m$ series, peptide G gave the most intense SWCNT near-IR fluorescence. In an attempt to further raise the emission efficiency, we studied a related structure, $K_2(QF)_5K_2$ (peptide J), in which the leucine residues (L) were replaced by aromatic-containing phenylalanine residues (F). The importance of aromatic groups in surfactants used to suspend SWCNTs has been discussed previously.[45] We used the methods described above to characterize SWCNTs coated with the new peptide J and found a fluorescence efficiency ~40% higher than that with peptide G (see Figures 5.2 b and 5.4). The measured values are listed in Table 5.2.

Examination of our single-nanotube measurements of line widths and emission efficiencies reveals a striking correlation. As shown in Figure 5.8, coatings that give sharper emission peaks also give the highest emission efficiencies. We presume that the

variations in emission efficiencies reflect coating-related differences in nonradiative decay rate of the emitting excitonic state. One possible mechanism is that less uniform coatings lead to accelerated exciton decay as portions of the nanotube surface are exposed to perturbation by the surrounding solution. The data for relative emission efficiency vs spectral line width $\delta\nu$ can be fit by the decaying exponential function plotted as a solid curve in Figure 5.8:

$$\text{Relative emission} = 160 \bullet \exp(-\delta\nu/22\ \text{cm}^{-1}) + 0.05 \qquad (1)$$

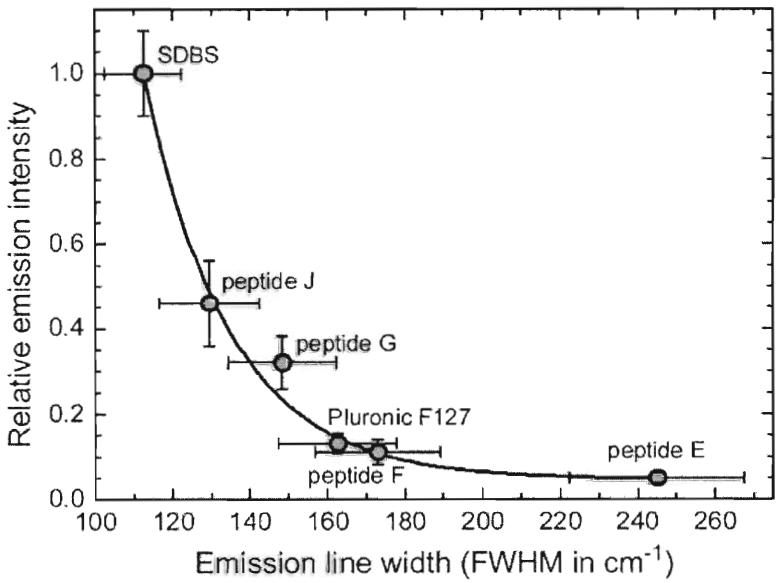

Figure 5.8. Relative emission intensities measured for individual aqueous SWCNTs in six coatings (taken from the last row of Table 5.2) as a function of emission line widths. Line width values in this plot were taken from measurements only on (10,2) nanotubes to avoid structure-dependent line width effects. Error bars on the *x*-axis represent the full range of measured values, not standard deviations. The solid curve is an exponential best fit to the data. Figure by Dmitri Tsyboulski.

When extrapolated to air-suspended SWCNTs, for which the reported (10,2) line width is ~100 cm^{-1},[46] the equation predicts an emission efficiency nearly twice that of nanotubes in aqueous SDBS suspension. The physical basis for this exponential relation remains to

be explored through further study. We note that spectral line widths measured in bulk samples contain additional inhomogenous broadening,[12, 37, 44] and so will not obey the relation of equation 1. Nevertheless, properly prepared bulk samples seem to show a coating-dependent spectral width variation parallel to that found for individual nanotubes. Our findings therefore suggest that one can estimate the relative brightness of individual SWNCTs in different coating environments through simple bulk spectroscopy rather than through demanding measurements involving single-nanotube fluorescence microscopy.

Single-nanotube photometric measurements under controlled conditions have shown that the intensity of near-IR emission from SWCNTs in aqueous suspension depends strongly on the coating material. Emission in common biocompatible surfactants such as Pluronic F127, ss-DNA, and BSA is weak relative to that in SDBS. This work has identified that multidomain peptides should allow biocompatibility with improved SWCNT emission. The self-assembling properties of these multidomain peptides were found to correlate strongly with their ability to suspend nanotubes and preserve their emission efficiency. The peptides that allowed the brightest SWCNT emission were not those that displayed the strongest tendency to self-assemble, but rather those with similar but slightly modified structures and weaker self-assembly tendencies.

D. Biocompatibility of Peptide SWCNT Surfactants

1. Sequence Modifications Confer Biocompatibility

After the initial series of multidomain peptides had shown to suspend carbon nanotubes while allowing satisfactory fluorescence emission, the biocompatibility of these peptides was investigated. When multidomain peptides from the series $K_n(QL)_mK_n$ were added to cell culture medium to assess their compatibility with biological systems, it was found that peptides bearing the positively charged residue lysine in the charged domain had a tendency to aggregate in the culture medium. Aggregation occurred regardless of whether single-walled carbon nanotubes were present. It is likely that negatively charged phosphate ions in the cell culture medium interacted with positively charged lysine residues, effectively screening the charge on these terminal residues. As the charge on the terminal residues was reduced, the individual peptides no longer repelled one another and self-assembled into gel-like aggregates. When a suspension of SWCNTs in aqueous $K_2(QL)_5K_2$ was added to a culture of NIH 3T3 cells, the aggregates formed were large enough to be easily visible with a standard light microscope (Figure 5.9). To avoid this problem, we prepared analogous peptides in which the positively charged lysine was replaced by the negatively charged glutamic acid. When such peptides displaying glutamic acid as the terminal residues were added to cell culture medium, no visible aggregates were detectable via light microscopy. This observation lends evidence for the lysine-phosphate interaction that is suspected to take place in the

cell culture medium. Therefore, for cytotoxicity studies, the multidomain peptides $E(QL)_6E$ and $E(QL)_6EGRGDS$ were used instead (Figure 5.10).

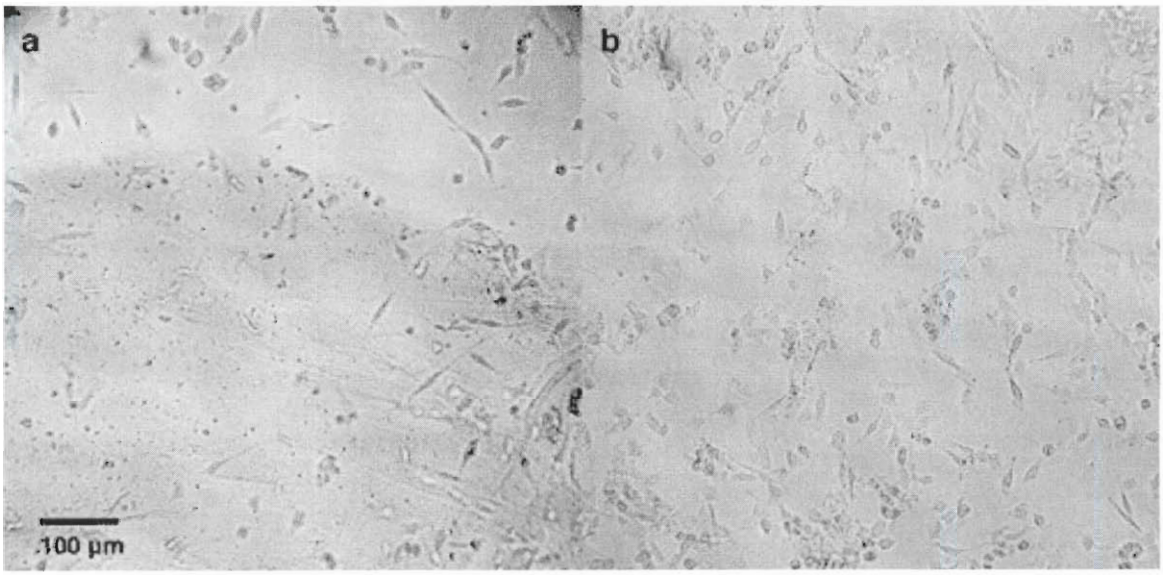

Figure 5.9. Light microscope images of NIH 3T3 fibroblasts incubated with SWCNT suspensions in a) $K_2(QL)_5K_2$ and b) $E(QL)_6E$. The brown area in the lower portion of panel a) is a gel-like aggregation of peptide-coated SWCNTs.

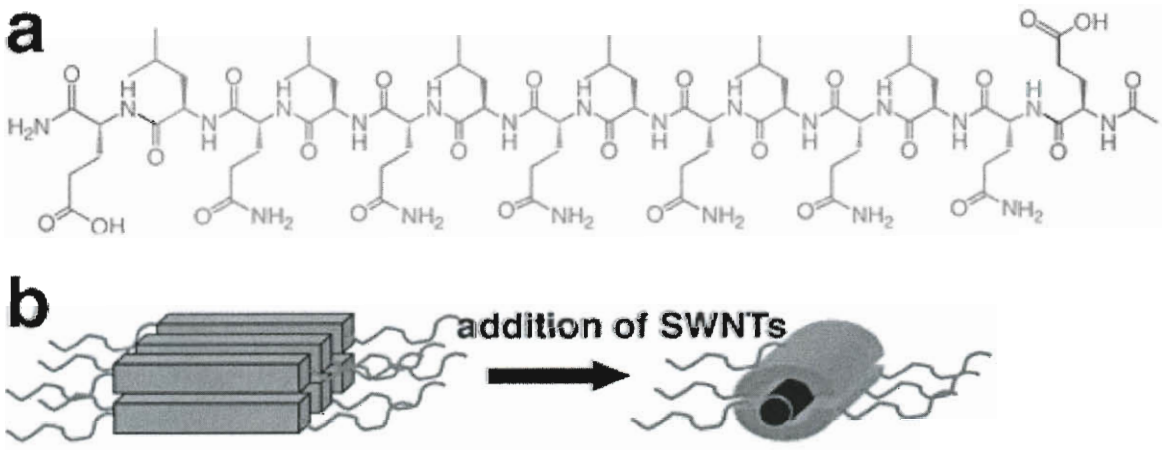

Figure 5.10. Structure of multidomain peptide a) $E(QL)_6E$ and b) associated nanofibers.

2. Characterization of Peptide-SWCNT Suspensions

To ensure that the SWCNT suspensions being added to cell cultures contained individual SWCNTs and not aggregates, AFM of the SWCNT solutions was performed (Figure 5.11). This also allowed visualization of the peptide nanofibers to confirm that the predicted self-assembly of the peptides was taking place. The absence of large bundles of either peptide or SWCNTs in the AFM images indicated that the SWCNTs were well-dispersed by the peptide. Furthermore, height profiles measured from AFM images were consistent with the dimensions of individual SWCNTs coated by peptides. It was noticed that peptide-suspended SWCNTs visible by AFM appear to be approximately 100 nm in length, shorter than would be predicted by the length distribution of HiPCO-produced SWCNTs. AFM of SWCNTs suspended in SDBS (but prepared under identical suspension conditions to those of peptide-SWCNT samples) show some longer SWCNTs, although these nanotubes appear somewhat aggregated.

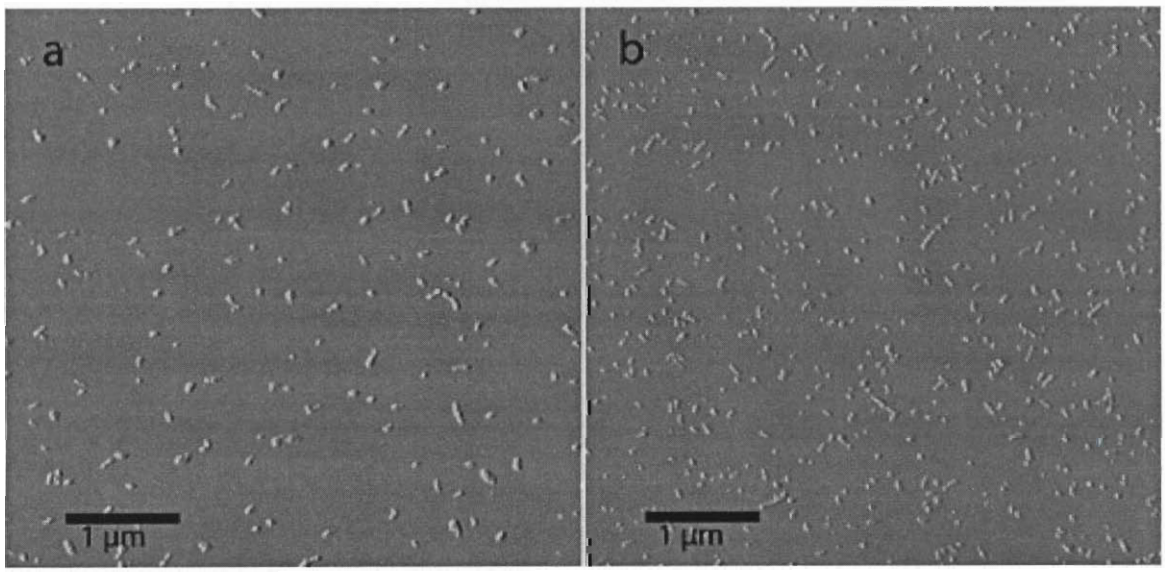

Figure 5.11. AFM images of SWCNTs suspended in a) $E(QL)_6E$ and b) $E(QL)_6EGRGDS$.

This suggests that these multidomain peptides are selectively suspending shorter SWCNTs. We also measured near-IR fluorescence spectra of each freshly prepared SWCNT suspension, using laser excitation at 659 and 784 nm (Figure 5.12). These measurements provide additional information about the aggregation state of the suspended nanotubes, since SWCNT bundling quenches fluorescence. Fluorescence spectra normalized to sample absorbance values reveal that of the biocompatible surfactants, $E(QL)_6E$ allows better fluorescence efficiency than either of the Pluronic surfactants, while $E(QL)_6EGRGDS$ is intermediate to the two Pluronics.

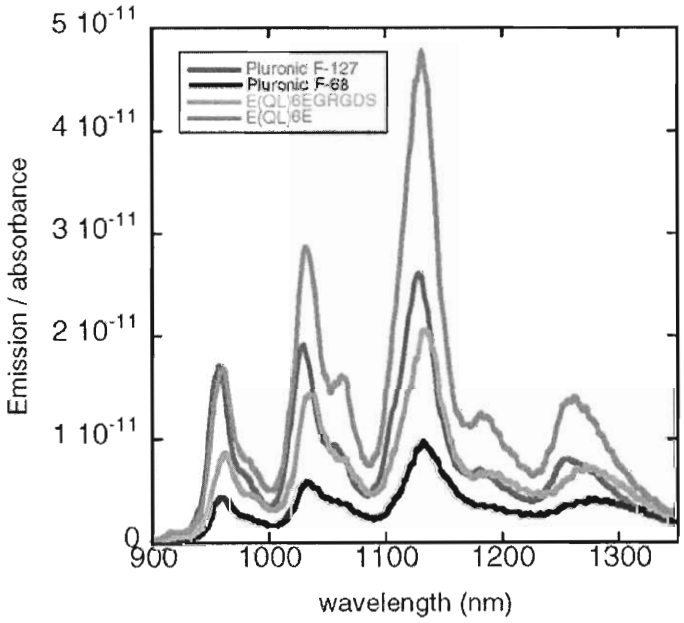

Figure 5.12. Fluorescence emission spectra of SWCNT suspensions in different surfactants, with 659 nm excitation. Curves have been normalized according to the sample absorbance to show relative fluorescence efficiencies.

3. Peptide Cytotoxicity

In our cytotoxicity studies, NIH 3T3 fibroblasts were seeded in each well of a 24 well plate and allowed to incubate overnight. The following day, the peptide or peptide-SWCNT solutions were added directly to the cell wells. Cells were detached from the cell

culture plate with trypsin at 48 h, stained with Trypan blue, and then counted using a hemocytometer. For every concentration of surfactant or surfactant-SWCNT suspension tested, there was a negative control, which consisted of NIH 3T3 cells with no solutions added. Cell viabilities were normalized against these negative controls for each condition. The data were analyzed by two-way ANOVA, and the more subtle differences between specific surfactants were analyzed by one-way ANOVA (Figure 5.13). The one-way ANOVA results indicated that at the lowest concentration (150 μM) SDBS did not show statistically significant toxicity. At 300 μM and 1 mM concentrations, however, cell viability for SDBS-incubated cultures dropped to zero, a toxicity that was statistically significant compared with every other surfactant. This confirmed that SDBS is highly cytotoxic and unsuitable for use in mammalian cell culture. Although the multidomain peptides $E(QL)_6E$ and $E(QL)_6$EGRGDS did appear to show some dose-dependent cytotoxicity, this cytotoxicity was not significantly different from the Pluronic series at 150 and 300 μM concentrations. That is, *t* tests comparing cell viability between different surfactants at 150 and 300 μM yielded *P* values above 0.05 for every possible comparison of two surfactants, except for the comparison of SDBS-incubated cultures with all other cultures at 300 μM (as SDBS shows substantial toxicity at this concentration). As Pluronic and peptide toxicities are not significantly different from one another at or below 300 μM, the peptides explored here provide viable options for delivering nanotubes in vitro at low concentrations. At 1 mM surfactant concentration, however, the toxicity of the multidomain peptides becomes more apparent, with both peptides showing toxicities significantly higher than the Pluronics ($P < 0.05$).

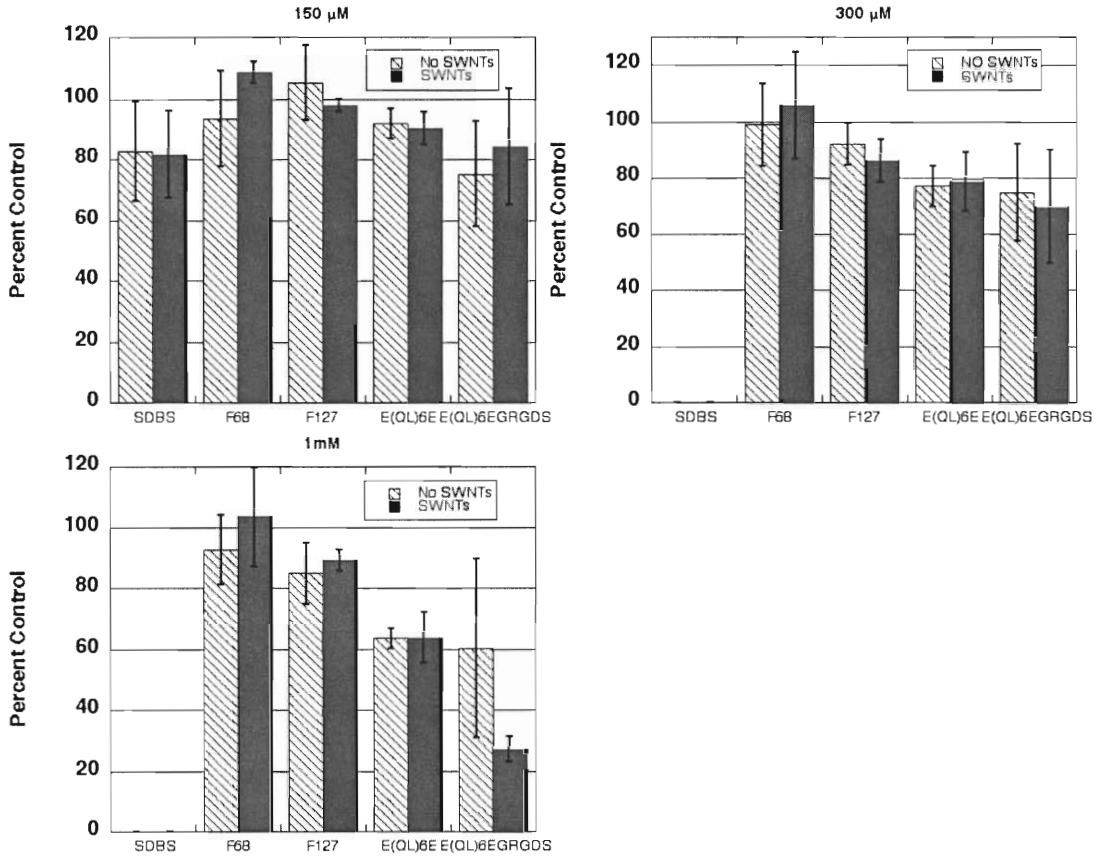

Figure 5.13. Cell viability of NIH 3T3 cells incubated for 48 h with 150 µM, 300 µM, and 1 mM surfactants. Half of the groups were incubated with single-walled nanotubes (shown in solid blue) and half of the groups were incubated in the absence of nanotubes (shown in black and white).

This toxicity may be due to the peptides themselves or may be due to impurities in the peptide preparations. The latter scenario is likely, as peptides capped by glutamic acid residues cannot be purified by HPLC and therefore retain many of the impurities introduced during peptide synthesis.

4. Single-Walled Carbon Nanotube Cytotoxicity

Analysis by two-way ANOVA makes it possible to distinguish which set of variable factors (surfactants or the presence of SWCNTs) is responsible for deviations from the

control, or whether the observed toxicity is caused by a combination of these two sets of factors. Because half of the experiments contained surfactants without SWCNTs and the other half contained surfactant-suspended SWCNTs, this provided an opportunity to assess the cytotoxicity of carbon nanotubes *in vitro*. This analysis revealed that single-walled carbon nanotubes showed no significant cytotoxicity, regardless of the identity or concentration of the surfactant. We found that the two-way ANOVA yielded a *P*-value above 0.05 for all comparisons collectively of SWCNT and non-SWCNT incubated cells ($P = 0.5342$, 0.9501, and 0.4345 for 150 μM, 300 μM, and 1 mM, respectively). The two-way ANOVA analyses also suggest that the combination of peptide with SWCNT is not responsible for any toxicity observed at surfactant concentrations of 150 or 300 μM ($P > 0.05$). A *P*-value of 0.0438 was obtained for the interaction of peptide surfactants with SWCNTs at the 1 mM concentration. However, SWCNTs themselves showed no toxicity at this concentration, casting doubt on the practical significance of this result. Thus, we conclude that there is no evidence for synergistic toxicity effects involving single-walled carbon nanotubes and peptide surfactants, at least at 150 μM and 300 μM concentrations.

Examination of cell morphology by light microscopy revealed that cells incubated in solutions of SDBS, with or without nanotubes, showed a rounded morphology indicative of a lack of cellular anchoring to the cell well plate (Figure 5.14 a). A rounded morphology precedes cell death, and indeed, cultures incubated at SDBS concentrations of 300 μM or higher experienced total cell death. By contrast, cell morphology in the presence of Pluronic F68, F127, $E(QL)_6E$, and $E(QL)_6EGRGDS$ appeared normal. Figure 5.14 b-d shows healthy cells in each of these conditions. These cells are spread out and anchored to the cell culture wells, morphology that is typical for fibroblasts.

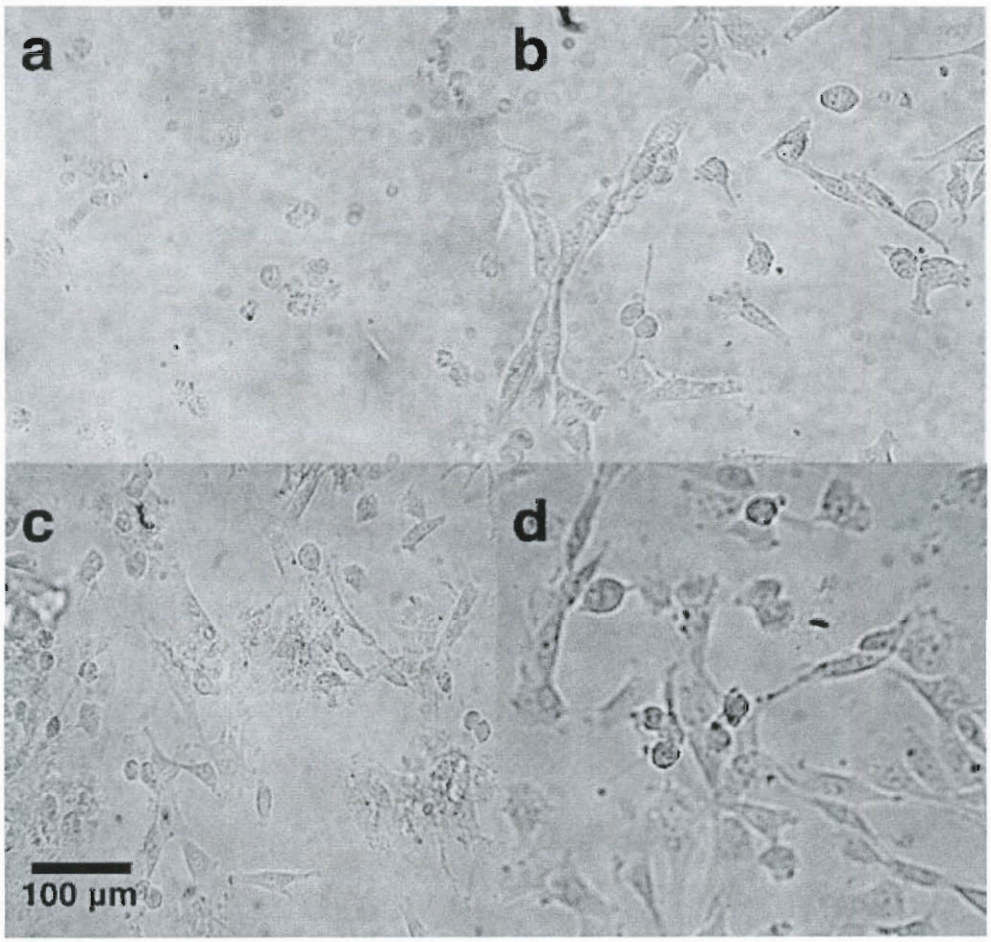

Figure 5.14. Cell morphology of NIH 3T3 cells after 24 h of incubation with a) SDBS, b) Pluronic F68, c) $E(QL)_6E$, and d) $E(QL)_6EGRGDS$.

After 48 h, cells were imaged with a near-IR fluorescence microscope. Imaging was performed through the cell culture plates so as not to disturb cell morphology. This allowed us to assess the interaction of SWCNTs with the cells as well as the amount of soluble peptide-wrapped SWCNTs remaining in solution. It was found that at 48 h, significant amounts of nanotubes still remained in solution. Interactions between SWCNTs and 3T3 cells were also observed (Figure 5.15).

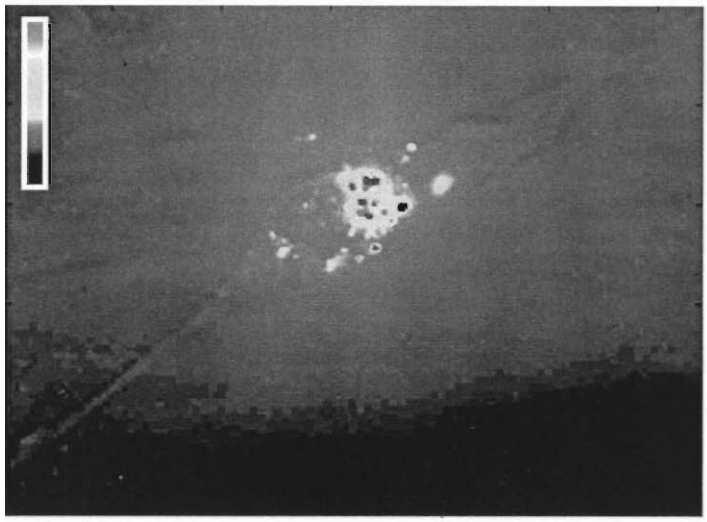

Figure 5.15. NIH 3T3 cell in the presence of single-walled carbon nanotubes suspended in $E(QL)_6EGRGDS$. The image shows near-IR fluorescence from the nanotubes, false-colored according to intensity. Bright spots indicate carbon nanotube clusters inside the cell body. Image from Dmitri Tsyboulski.

E. Conclusions

For single-walled carbon nanotubes to be used in many biological applications, suitable biocompatible surfactant coatings that noncovalently functionalize the SWCNTs are needed. Noncovalent surfactants wrap and solubilize carbon nanotubes while preserving their unusual electronic structure and optical properties. Standard ionic surfactants are highly cytotoxic, whereas traditional "biocompatible" surfactants such as Pluronic do not readily allow chemical modification. The alternatives presented here are customizable multidomain peptides that noncovalently modify SWCNTs by wrapping the nanotubes inside β-sheet nanofibers. The cytotoxicity of carbon nanotubes remains controversial. Some reports show a lack of toxicity,[9, 47, 48] while others find the opposite effect.[49, 50] In comparative studies, we find statistically significant differences between the viabilities of cultured cells incubated with SWCNTs suspended by different

surfactants. However, analysis indicates that the cytotoxicity arises from the surfactants rather from the SWCNTs or from synergistic effects between nanotubes and surfactants. We therefore suggest that it is not necessarily the SWCNTs that may be cytotoxic, but rather the agents in which they are suspended and their aggregation state. Our two-way ANOVA analysis shows that, within the concentration range used here, disaggregated SWCNTs do not influence the viability of the 3T3 cells in culture. Thus, single-walled carbon nanotubes seem to be acceptably nontoxic for in vitro biological applications as long as the surfactants used to suspend them are effective and nontoxic. We find that the new multidomain peptides are approximately as nontoxic as the Pluronic surfactants, and that they allow comparable SWCNT fluorescence efficiency while offering options for simple chemical customization. Our qualitative findings are summarized in Table 5.3. Because peptides allow for a wide range of chemical functionalities, one can design surfactants that are both nontoxic and provide biological specificity, such as enhanced integrin binding through the RGD sequence on the C-terminus of $E(QL)_6EGRGDS$. We have shown that such cell-adhesion sequences may be incorporated without compromising the ability of the peptide to self-assemble. This suggests that other cell-adhesion sequences and targeting moieties can also be incorporated into the multidomain peptides, enabling important new biological applications of carbon nanotubes. Furthermore, peptides may undergo hydrolysis in vivo through the action of various peptidases naturally found in the body, providing a starting point for metabolism of peptide-based surfactants. This biodegradation is essential if a potentially toxic buildup of surfactant is to be avoided. These qualities extend the general range of applications of peptide surfactants far beyond that of traditional Pluronic surfactants.

	Covalent Modification	SDBS	Pluronics	Lys-capped peptides	Glu-capped peptides
Suspension Stability	good	good	fair	good*	good
Fluorescence/ Absorbance	poor	good	fair	good	fair
Cytotoxicity	varies	poor	good	N/A	good

Table 5.3. Summary of properties of different single-walled carbon nanotube surfactants *Suspensions of SWCNTs are stable at room temperature for weeks or months outside of cell culture conditions. However, when added to cell culture, although the SWCNTs remain stably suspended, the entire suspension forms a hydrogel.

F. Experimental

Peptide Synthesis and Purification. Peptides were synthesized on a 0.15 mmol scale with an Advanced Chemtech Apex 396 peptide synthesizer using standard Fmoc chemistry, as described in Chapter 3.

Preparation of SWCNT/Peptide Suspensions. Peptides were first dissolved in ultrapure water at a concentration of 10 mg/mL. Single-walled carbon nanotubes grown in the Rice University HiPco reactor (batch HPR 161.1) were used without further purification. SWCNT samples of ~1 mg were weighed out and placed in 1.5 mL Eppendorf tubes. To these were added 1 mL of the peptide solution with pH adjusted to 7. The mixtures were then sonicated for 11 s using a Microson XL 2000 tip sonicator at a power level of 5 W. The sonicator probe was immersed to approximately one-half the solution depth. Each sample was then centrifuged for 5 min in a Sorvall Biofuge Pico centrifuge at 10,000 × g. The supernatant was decanted and centrifuged for an additional 10 min, followed by another round of decanting and centrifugation. The parameters in

this protocol were chosen to maximize sample fluorescence intensities. Although centrifugation helps to separate aggregated from individually suspended nanotubes, even extensive ultracentriguation does not entirely remove small bundles.[19, 36] We note that the presence of bundles does not affect our single-nanotube measurements.

Vis-NIR Absorbance and Fluorescence. Bulk absorbance and fluorescence measurements were collected on an NS1 NanoSpectralyzer (Applied NanoFluorescence, LLC). Excitation−emission fluorescence maps were measured on bulk SWCNT samples using a Fluorolog 3−211 spectrofluorometer (Horiba J-Y) equipped with a single-channel liquid nitrogen cooled InGaAs detector.

Near-IR Imaging of SWCNT Suspensions. Near-IR fluorescence imaging and spectroscopy of individual SWCNTs were performed using a custom-built apparatus described previously.[44] It is based on an inverted Nikon TE-2000U microscope with a Nikon PlanApo VC 60 × /1.4 NA oil-immersion objective. A combination of a dichroic beamsplitter and a dielectric 946 nm long-pass filter was used to select emission wavelengths greater than 950 nm. A liquid nitrogen cooled InGaAs camera (Roper Scientific OMA-V 2D) sensitive between 900 and 1600 nm was installed on one microscope output port. Another output port was coupled via optical fiber to the input slit of a C140 spectrograph (Horiba J-Y) equipped with a 512-element InGaAs array (OMA-V, Roper Scientific). In this way near-IR emission spectra could be acquired from a selected spatial region of ~1.5 × 1.5 μm at the sample. We excited samples with

circularly polarized beams from diode lasers emitting at 658 and 785 nm. The circular polarization ellipticity was ≥0.95.

Cryo-TEM Measurements. 10 μL of peptide-SWCNT suspension was placed on a holey carbon-coated copper grid (Quantifoil, 1.2/1.3 400 mesh) and gently blotted with filter paper using an FEI Vitrobot, forming a thin film on the grid. The grid was dropped into liquid ethane and then transferred into liquid nitrogen. Images were acquired using a JEOL 2010 transmission electron microscope at an accelerating voltage of 200 kV.

Atomic Force Microscopy (AFM). SWCNT-peptide solutions were diluted 20-fold with ultrapure water and were dropped onto freshly cleaved mica while spinning on a Headway Research, Inc. photoresist spinner. Samples were rinsed with deionized water for 1−2 s and then spun for an additional 10 min. AFM images were collected as previously described.

Cell Culture. NIH 3T3 mouse fibroblasts were obtained from the American type Culture Collection and were cultured in Corning 75 cm^2 cell culture flasks. Dulbecco's modified Eagle medium (Gibco) was supplemented with 10% FBS and 1% penicillin-streptomycin v/v. Cells were cultured in an incubator at 37 °C at 5% CO_2 and the medium was changed approximately every 2 days. Propagation of this cell line required cells to be passaged every 6−7 days. For the toxicity experiments, 5×10^4 cells were placed in wells in a 24-well plate and allowed to incubate overnight. A 15 mM stock solution of peptide or peptide-SWCNT suspension was added to reach the desired

concentrations of 150, 300, and 1000 μM. The cells were then incubated for an additional 48 h. At 48 h, cells were detached from the wells with trypsin and stained with Trypan Blue. Viable cells exclude Trypan blue from the cell, while the dye leaks into dead or injured cells. Cells were then counted using a hemocytometer (Hausser Scientific) and Nikon Eclipse E400 optical microscope.

Near-IR Imaging of 3T3 Cells Exposed to SWCNT Suspensions. Near-IR fluorescence imaging of 3T3 cells was performed using a custom-built apparatus based on an inverted Nikon TE-2000U microscope with a Nikon PlanApo VC 60× /1.4 NA oil-immersion objective[25]. A combination of a dichroic beamsplitter and a dielectric 946 nm long-pass filter was used to select emission wavelengths greater than 950 nm. A liquid nitrogen cooled InGaAs camera (Roper Scientific OMA-V 2D) sensitive between 900 and 1600 nm was installed on one microscope output port. Another output port was coupled via fiberoptic cable to the input slit of a J-Y C140 spectrograph equipped with a 512-element InGaAs array (OMA-V, Roper Scientific). In this way, near-IR emission spectra could be acquired from a spatial region of ~1.5 × 1.5 μm at the sample. We excited samples with circularly polarized beams from diode lasers emitting at 658 and 785 nm. The circular polarization ellipticity was ≥0.95.

One and Two-Way ANOVA. Analysis of variance (ANOVA) was performed using Prism software. Two-way ANOVA was performed to determine whether the interaction of SWCNTs with the surfactant affected the solution toxicity, while one-way ANOVA and Tukey tests were used to compare each condition with every other.

References

(1) Baughman, R. H.; Zakhidov, A. A.; de, H., WA. *Science* **2002**, *297*, 787-792.

(2) Peng, H. S. *J. Am. Chem. Soc.* **2008**, *130*, 42-43.

(3) Martin, C. R.; Kohli, P. *Nat. Rev. Drug Discovery* **2003**, *2*, 29-37.

(4) Hartschuh, A.; Pedrosa, H. N.; Novotny, L.; Krauss, T. D. *Science* **2003**, *301*, 1354-1356.

(5) Matsuda, K.; Kanemitsu, Y.; Irie, K.; Saiki, T.; Someya, T.; Miyauchi, Y.; Maruyama, S. *Appl. Phys. Lett.* **2005**, *86*, ARTN 123116.

(6) Lefebvre, J.; Fraser, J. M.; Finnie, P.; Homma, Y. *Phys. Rev. B* **2004**, *69*, ARTN 075403.

(7) Bachilo, S. M.; Strano, M. S.; Kittrell, C.; Hauge, R. H.; Smalley, R. E.; Weisman, R. B. *Science* **2002**, *298*, 2361-2366.

(8) Cognet, L.; Tsyboulski, D.; Rocha, J.-D. R.; Doyle, C. D.; Tour, J. M.; Weisman, R. B. *Science* **2007**, *316*, 1465-1468.

(9) Cherukuri, P.; Bachilo, S. M.; Litovsky, S. H.; Weisman, R. B. *J. Am. Chem. Soc.* **2004**, *126*, 15638-15639.

(10) Barone, P. W.; Baik, S.; Heller, D. A.; Strano, M. S. *Nat. Mater.* **2005**, *4*, 86-U16.

(11) Lefebvre, J.; Austing, D. G.; Bond, J.; Finnie, P. *Nano Lett.* **2006**, *6*, 1603-1608.

(12) Tsyboulski, D. A.; Rocha, J. D. R.; Bachilo, S. M.; Cognet, L.; Weisman, R. B. *Nano Lett.* **2007**, *7*, 3080-3085.

(13) Carlson, L. J.; Maccagnano, S. E.; Zheng, M.; Silcox, J.; Krauss, T. D. *Nano Lett.* **2007**, *7*, 3698-3703.

(14) Cherukuri, P.; Gannon, C. J.; Leeuw, T. K.; Schmidt, H. K.; Smalley, R. E.; Curley, S. A.; Weisman, R. B. *Proc. Natl. Acad. Sci. U. S. A.* **2006**, *103*, 18882-18886.

(15) Leeuw, T. K.; Reith, M.; Simonette, R. A.; Harden, M. E.; Cherukuri, P.; Tsyboulski, D. A.; Beckingham, K. M.; Weisman, R. B. *Nano Lett.* **2007**, *7*, 2650-2654.

(16) Jin, H.; Heller, D. A.; Strano, M. S. *Nano Lett.* **2008**, *8*, 1577-1585.

(17) Duque, J. G.; Cognet, L.; Parra-Vasquez, A. N. G.; Nicholas, N.; Schmidt, H. K.; Pasquali, M. *J. Am. Chem. Soc.* **2008**, *130*, 2626-2633.

(18) Bahr, J. L.; Tour, J. M. *J. Mater. Chem.* **2002**, *12*, 1952-1958.

(19) O'Connell, M. J.; Bachilo, S. M.; Huffman, C. B.; Moore, V. C.; Strano, M. S.; Haroz, E. H.; Rialon, K. L.; Boul, P. J.; Noon, W. H.; Kittrell, C.; Ma, J. P.; Hauge, R. H.; Weisman, R. B.; Smalley, R. E. *Science* **2002**, *297*, 593-596.

(20) Moore, V. C.; Strano, M. S.; Haroz, E. H.; Hauge, R. H.; Smalley, R. E. *Nano Lett.* **2003**, *3*, 1379-1382.

(21) Wang, R.; Cherukuri, P.; Duque, J. G.; Leeuw, T. K.; Lackey, M. K.; Moran, C. H.; Moore, V. C.; Conyers, J. L.; Smalley, R. E.; Schmidt, H. K.; Weisman, R. B.; Engel, P. S. *Carbon* **2007**, *45*, 2388-2393.

(22) Welsher, K.; Liu, Z.; Daranciang, D.; Dai, H. *Nano Lett.* **2008**, *8*, 586-590.

(23) Dong, L.; Joseph, K. L.; Witkowski, C. M.; Craig, M. M. *Nanotechnology* **2008**, *19*, 255702.

(24) Hellung-Larsen, P.; Assaad, F.; Pankratova, S.; Saietz, B. L.; Skovgaard, L. T. *J. Biotechnol.* **2000**, *76*, 185-195.

(25) Zheng, M.; Jagota, A.; Semke, E. D.; Diner, B. A.; Mclean, R. S.; Lustig, S. R.; Richardson, R. E.; Tassi, N. G. *Nat. Mater.* **2003**, *2*, 338-342.

(26) Matsuura, K.; Saito, T.; Okazaki, T.; Ohshima, S.; Yumura, M.; Iijima, S. *Chem. Phys. Lett.* **2006**, *429*, 497-502.

(27) Ortiz-Acevedo, A.; Xie, H.; Zorbas, V.; Sampson, W. M.; Dalton, A. B.; Baughman, R. H.; Draper, R. K.; Musselman, I. H.; Dieckmann, G. R. *J. Am. Chem. Soc.* **2005**, *127*, 9512-9517.

(28) Wang, S. Q.; Humphreys, E. S.; Chung, S. Y.; Delduco, D. F.; Lustig, S. R.; Wang, H.; Parker, K. N.; Rizzo, N. W.; Subramoney, S.; Chiang, Y. M.; Jagota, A. *Nat. Mater.* **2003**, *2*, 196-200.

(29) Zorbas, V.; Ortiz-Acevedo, A.; Dalton, A. B.; Yoshida, M. M.; Dieckmann, G. R.; Draper, R. K.; Baughman, R. H.; Jose-Yacaman, M.; Musselman, I. H. *J. Am. Chem. Soc.* **2004**, *126*, 7222-7227.

(30) Xie, H.; Ortiz-Acevedo, A.; Zorbas, V.; Baughman, R. H.; Draper, R. K.; Musselman, I. H.; Dalton, A. B.; Dieckmann, G. R. *J. Mater. Chem.* **2005**, *15*, 1734-1741.

(31) Arnold, M. S.; Guler, M. O.; Hersam, M. C.; Stupp, S. I. *Langmuir* **2005**, *21*, 4705-4709.

(32) Pender, M. J.; Sowards, L. A.; Hartgerink, J. D.; Stone, M. O.; Naik, R. R. *Nano Lett.* **2006**, *6*, 40-44.

(33) Witus, L. S.; Rocha, J. D. R.; Yuwono, V. M.; Paramonov, S. E.; Weisman, R. B.; Hartgerink, J. D. *J. Mater. Chem.* **2007**, *17*, 1909-1915.

(34) Dieckmann, G. R.; Dalton, A. B.; Johnson, P. A.; Razal, J.; Chen, J.; Giordano, G. M.; Munoz, E.; Musselman, I. H.; Baughman, R. H.; Draper, R. K. *J. Am. Chem. Soc.* **2003**, *125*, 1770-1777.

(35) Su, Z.; Mui, K.; Daub, E.; Leung, T.; Honek, J. *J. Phys. Chem. B* **2007**, *111*, 14411-14417.

(36) Crochet, J.; Clemens, M.; Hertel, T. *J. Am. Chem. Soc.* **2007**, *129*, 8058-8059.

(37) Weisman, R. B.; Saito, S.; Zettl, A. **2008**, *Chapter 5*, 109-133.

(38) Tsyboulski, D. A.; Bachilo, S. M.; Kolomeisky, A. B.; Weisman, R. B. *ACS Nano* **2008**, *2*, 1770-1776.

(39) Casey, J. P.; Bachilo, S. M.; Moran, C. H.; Weisman, R. B. *ACS Nano* **2008**, *2*, 1738-1746.

(40) Weisman, R. B.; Bachilo, S. M. *Nano Lett.* **2003**, *3*, 1235-1238.

(41) Wang, F.; Sfeir, M. Y.; Huang, L. M.; Huang, X. M. H.; Wu, Y.; Kim, J. H.; Hone, J.; O'Brien, S.; Brus, L. E.; Heinz, T. F. *Phys. Rev. Lett.* **2006**, *96*, ARTN 167401.

(42) Ohno, Y.; Iwasaki, S.; Murakami, Y.; Kishimoto, S.; Maruyama, S.; Mizutani, T. *Phys. Status Solidi B* **2007**, *244*, 4002-4005.

(43) Choi, J. H.; Strano, M. S. *Appl. Phys. Lett.* **2007**, *90*, ARTN 223114.

(44) Tsyboulski, D. A.; Bachilo, S. M.; Weisman, R. B. *Nano Lett.* **2005**, *5*, 975-979.

(45) Zorbas, V.; Smith, A. L.; Xie, H.; Ortiz-Acevedo, A.; Dalton, A. B.; Dieckmann, G. R.; Draper, R. K.; Baughman, R. H.; Musselman, I. H. *J. Am. Chem. Soc.* **2005**, *127*, 12323-12328.

(46) Inoue, T.; Matsuda, K.; Murakami, Y.; Maruyama, S.; Kanemitsu, Y. *Phys. Rev. B* **2006**, *73*, ARTN 233401.

(47) Correa-Duarte, M. A.; Wagner, N.; Rojas-Chapana, J.; Morsczeck, C.; Thie, M.; Giersig, M. *Nano Lett.* **2004**, *4*, 2233-2236.

(48) Kolosnjaj-Tabi, J.; Hartman, K. B.; Boudjemaa, S.; Ananta, J. S.; Morgant, G.; Szwarc, H.; Wilson, L. J.; Moussa, F. *ACS Nano* **2010**, *4*, 1481-1492.

(49) Magrez, A.; Kasas, S.; Salicio, V.; Pasquier, N.; Seo, J. W.; Celio, M.; Catsicas, S.; Schwaller, B.; Forro, L. *Nano Lett.* **2006**, *6*, 1121-1125.

(50) Tian, F.; Cui, D.; Schwarz, H.; Estrada, G. G.; Kobayashi, H. *Toxicol. in Vitro* **2006**, *20*, 1202-1212.

Chapter 6: Conclusions

Self-assembly is a powerful process that utilizes various noncovalent interactions to direct the construction of more complex nanostructures. While self-assembly is widespread in biology, peptides and proteins are particularly stunning examples of what structures and functions are possible as a result of this assembly. Over the past four years, I have attempted to harness the potential of supramolecular chemistry to construct a library of multidomain peptides that self-assemble into discrete nanofibers. These peptides assemble under the influence of charge screening, forming a dense fibrous network that is often accompanied by the transition from liquid to gel. Within the realm of multidomain peptides, I have shown that variation of particular amino acids in the primary structure can lead to changes in the secondary structure, as well as changes in the mechanical properties of the resulting hydrogels. Variation of the charged amino acids in the peripheral block has resulted in peptides that are compatible with cell culture. Substitution of the hydrophilic amino acids in the central block leads to changes in the hydrogen bonding network on the hydrophilic exterior of the fiber, which in turn leads to changes in the rigidity of the gel. Substitution of the hydrophobic amino acids in the central block of the peptide introduces new interactions into our self-assembly scheme: the introduction of π-π stacking interactions. This π-π stacking exerts some influence over the self-assembly process, leading to changes in the secondary and tertiary structure of the peptides. Each subtle change can be used to tailor the multidomain peptide for unique applications.

Although multidomain peptides hold a world of promise in many fields, two specific applications were discussed here. The first of these is to use a multidomain peptide

hydrogel, specifically $E_2(SL)_6E_2$GRGDS, as a controlled-release medium for the delivery of compounds secreted by embryonic stem cells. Stem cells are known to secrete a variety of therapeutic compounds, some of which we were able to identify. These include osteopontin, follistatin, ICAM-5, CCR10, and adiponectin. Many of these compounds can be absorbed and released by multidomain peptide gels, and collectively this secretome was shown to alleviate the increased cell permeability that is associated with kidney injury *in vitro*. After encouraging *in vitro* results, the rheological properties of the $E_2(SL)_6E_2$GRGDS hydrogel were investigated. It was found that $E_2(SL)_6E_2$GRGDS is ideally suited to injection via syringe and needle: the hydrogel is not only stable over time, but shows the ability to recover immediately after needle shear. The ability to recover within just seconds of the shearing event allows the gel reform after flowing through the needle rather than remaining in a liquefied state. This allows the gel to remain localized in the area of injection rather than flowing away from the target area. Finally, with this knowledge, $E_2(SL)_6E_2$GRGDS hydrogels were tested *in vivo* and shown to improve kidney function in mice with induced kidney damage. Reduction in the urinary albumin/creatinine ratio, coupled with significant decreases in serum BUN and creatinine levels, indicates an improvement in overall kidney function in these animals. Together, these promising results indicate that peptide hydrogels are good candidates for drug delivery materials, and that this system provides a cell-free alternative to current stem cell therapies.

A second application of multidomain peptides discussed was the use of peptides as surfactants for single-walled carbon nanotubes. One of the primary obstacles for carbon nanotube-based therapies is the insolubility of nanotubes in virtually every solvent.

Although research into appropriate surfactants for nanotubes has been extensive, few surfactants exist that actually preserve the properties that make SWCNTs attractive (namely, fluorescence) while remaining biocompatible. Several multidomain peptides solve this problem: $K_3(QL)_6K_3$, $K_2(QL)_6K_2$, and $K_2(QL)_5K_2$. Each of these peptides forms β-sheet peptide nanofibers that are capable of encapsulating the carbon nanotube. $K_2(QL)_5K_2$ seems to show less of a propensity for nanofiber formation than $K_3(QL)_6K_3$ or $K_2(QL)_6K_2$, yet it solubilizes SWCNTs extremely well, indicating that the peptide may actually use the SWCNT as a template for fiber formation. These multidomain peptides also preserve the fluorescence properties of the SWCNT, a property that is destroyed or suppressed by other solubilization methods. Substitution of leucine with phenylalanine to attain $K_2(QF)_5K_2$ results in even better SWCNT fluorescence. However, multidomain peptides bearing lysine residues on the termini aggregate in the presence of cell culture medium, making them unsuitable for biological applications. The substitution of positively-charged lysine with negatively-charged glutamic acid results in two peptides that suspend SWCNTs and are compatible with cell culture. These peptides, $E(QL)_6E$ and $E(QL)_6$EGRGDS, were examined to determine their toxicity. It was found that at low concentrations, peptide surfactants were nontoxic to cells, while at higher concentrations, some toxicity was observed. When these peptide surfactants were used to deliver SWCNTs to fibroblast cultures, no significant difference was found between cultures treated with peptide-SWCNT suspensions and those treated with peptide solutions alone. Thus, during this study, we were also able to determine that single-walled carbon nanotubes are nontoxic to fibroblasts.

These applications demonstrate that multidomain peptides make up a highly versatile platform that is customizable to accomplish different objectives. Whether we are seeking sustained drug release from a robust hydrogel or the next new surfactant, multidomain peptides can take advantage of the wide range of functional groups available to make this happen. Their strong tendency to reside in the β-sheet conformation means that these modifications can be tolerated without sacrificing the novel self-assembled nanostructures formed by these peptides. This resilient system is yet another testament to the power of molecular self-assembly.

The work discussed in this manuscript has been highlighted in several publications:

1. He Dong, Sergey E. Paramonov, Lorenzo Aulisa, Erica L. Bakota, and Jeffrey D. Hartgerink. Self-Assembly of Multidomain Peptides: Balancing Molecular Frustration Controls Conformation and Nanostructure. *J. Am. Chem. Soc.*, **2007,** 129, 12468-12472.

2. Dmitri A. Tsyboulski, Erica L. Bakota, Leah S. Witus, John-David R. Rocha, Jeffrey D. Hartgerink and R. Bruce Weisman. Self-Assembling Peptide Coatings Designed for Highly Luminescent Suspension of Single-Walled Carbon Nanotubes. *J. Am. Chem. Soc.*, **2008**, 130 (50), pp 17134–17140.

3. Erica L. Bakota, Lorenzo Aulisa, Dmitri A. Tsyboulski, R. Bruce Weisman and Jeffrey D. Hartgerink. Multidomain Peptides as Single-Walled Carbon Nanotube Surfactants in Cell Culture. *Biomacromolecules*, **2009**, 10 (8), pp 2201–2206.

4. Erica L. Bakota, Lorenzo Aulisa, Kerstin M. Galler, and Jeffrey D. Hartgerink. Enzymatic Cross-Linking of a Nanofibrous Peptide Hydrogel. *Biomacromolecules*, **2011**, 12(1), 82–87.

5. Yin Wang, Erica Bakota, Benny H. J. Chang, Mark Entman, Jeffrey D. Hartgerink, and Farhad R. Danesh. Peptide Nanofibers Preconditioned with Stem Cell Secretome Are Renoprotective. *Journal of the American Society of Nephrology*, **2011**, DOI:10.1681/ASN.2010040403

6. Erica L. Bakota, Yin Wang, Farhad Danesh, and Jeffrey D. Hartgerink. Injectable Multidomain Peptide Nanofiber Hydrogel as a Delivery Agent for Stem Cell Secretome. *Biomacromolecules*, **2011**, in accepted for publication.

Appendix 1: Peptide Library (alphabetical order)

Peptide	Relevant Chapter(s)
$C_4K_2(QL)_5K_2$	Chapter 5
$E(QL)_6E$	Chapter 5
$E(QL)_6EGRGDS$	Chapter 5
$E(SL)_6E$	Chapter 2
$E_2(QF)_5E_2$	Chapter 5
$E_2(QF)_6E_2$	Chapter 5
$E_2(QL)_6E_2$	Chapter 5
$E_2(SL)_3RG(SL)_3E_2GRGDS$	Chapter 2
$E_2(SL)_6E_2$	Chapters 2, 3
$E_2(SL)_6E_2GRGDS$	Chapters 2, 4
$K(SL)_3RG(SL)_3KGRGDS$	Chapter 2
$K_2(CLQL)_3K_2$	Chapter 2
$K_2(QF)_5K_2$	Chapter 5
$K_2(QF)_6K_2$	Chapters 2, 5
$K_2(QFQL)_3K_2$	Chapter 2
$K_2(QL)_5K_2$	Chapters 2, 5
$K_2(QL)_6K_2$	Chapters 2, 5
$K_2(QW)_5K_2$	Chapter 2
$K_2(QW)_6K_2$	Chapter 2
$K_2(QY)_5K_2$	Chapter 2
$K_2(QY)_6K_2$	Chapter 2

$K_2(SF)_5K_2$	Chapter 2
$K_2(SF)_6K_2$	Chapter 2
$K_2(SL)_6K_2$	Chapters 2, 3
$K_2(SL)_6K_2GRGDS$	Chapter 2
$K_2(SW)_5K_2$	Chapter 2
$K_2(SW)_6K_2$	Chapter 2
$K_2(TL)_6K_2$	Chapter 2
$K_2C(QL)_6CK_2$	Chapter 5
$K_3(QF)_6K_3$	Chapter 2
$K_3(QL)_6K_3$	Chapters 2, 5
$QK_2(SL)_6K_2Q$	Chapter 2

Appendix 2: Mass Spectrometry of Peptides

Mass spectra of peptides were achieved using standard MALDI techniques on a Bruker Autoflex mass spectrometer as discussed in previous chapters. Spectra were processed using FlexAnalysis software.

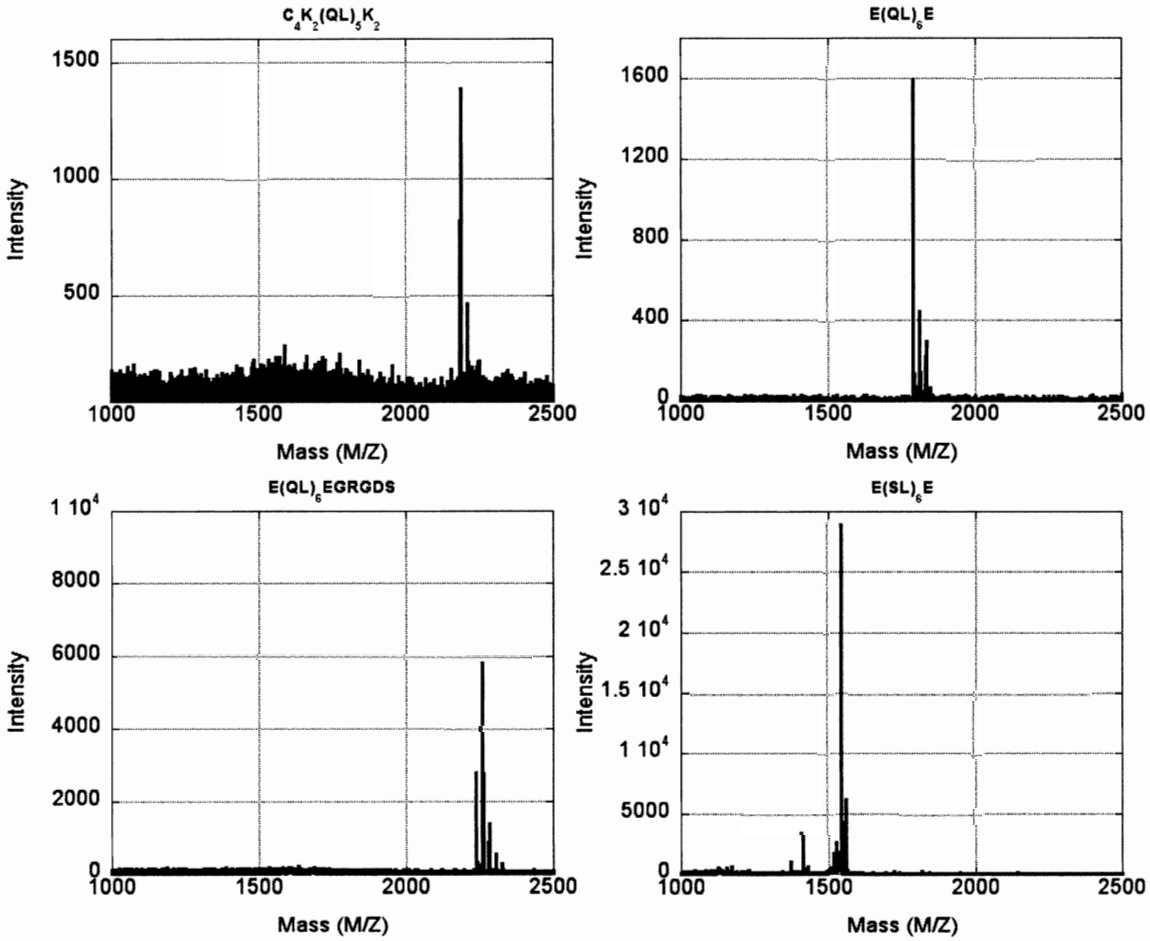

$C_4K_2(QL)_5K_2$	Expected Mass: 2189.2	Observed Mass: 2186.4
$E(QL)_6E$	Expected Mass: 1764.0	Observed Mass: 1784.9
$E(QL)_6EGRGDS$	Expected Mass: 2237.5	Observed Mass: 2239.0
$E(SL)_6E$	Expected Mass: 1517.8	Observed Mass: 1516.0

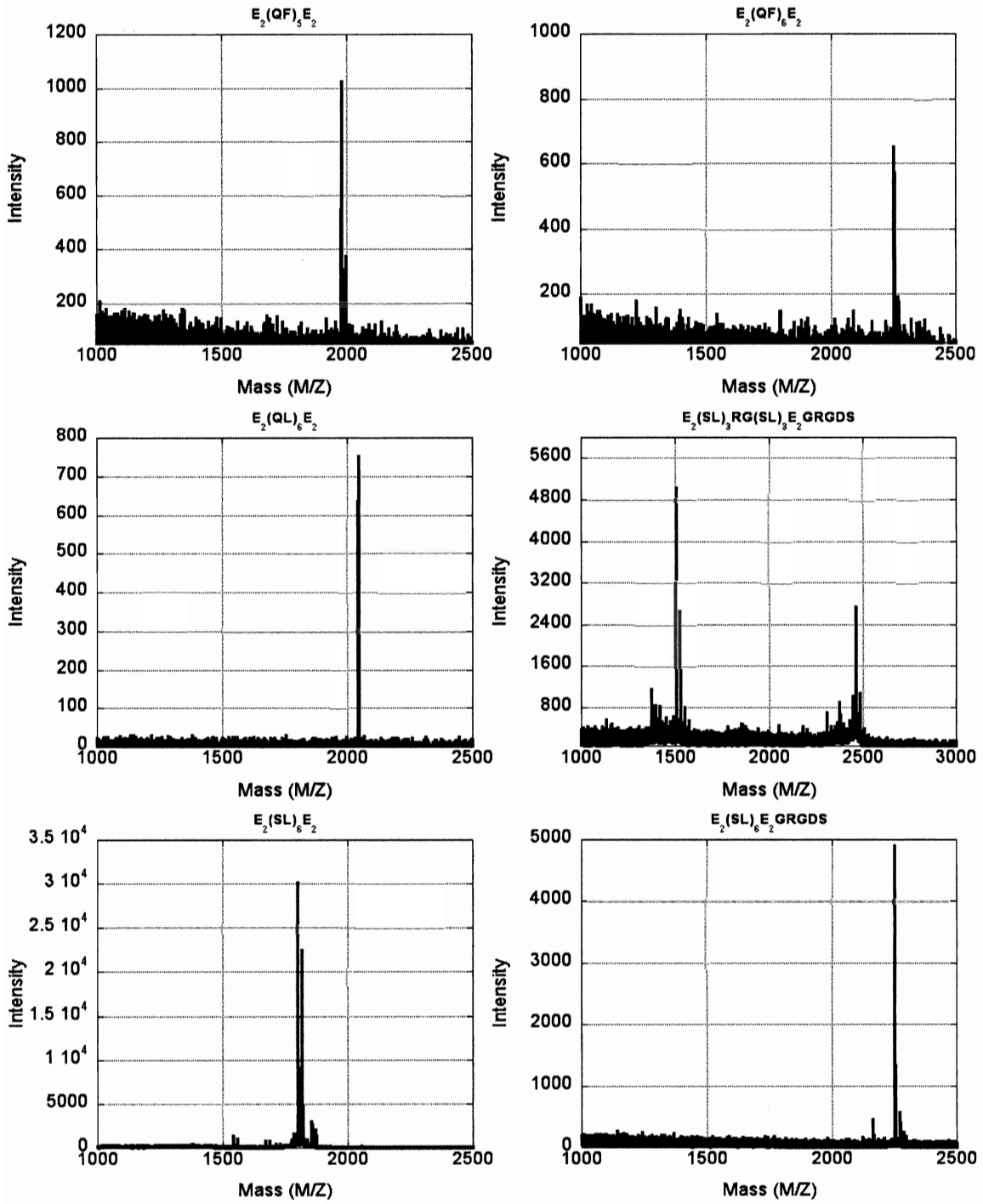

$E_2(QF)_5E_2$	Expected Mass: 1952.0	Observed Mass: 1951.8
$E_2(QF)_6E_2$	Expected Mass: 2227.4	Observed Mass: 2249.8
$E_2(QL)_6E_2$	Expected Mass: 2022.1	Observed Mass: 2044.7
$E_2(SL)_3RG(SL)_3E_2GRGDS$	Expected Mass: 2461.2	
Observed Mass: 1504.1, 2483.6		
$E_2(SL)_6E_2$	Expected Mass: 1776.9	Observed Mass: 1776.4
$E_2(SL)_6E_2GRGDS$	Expected Mass: 2249.4	Observed Mass: 2249.7

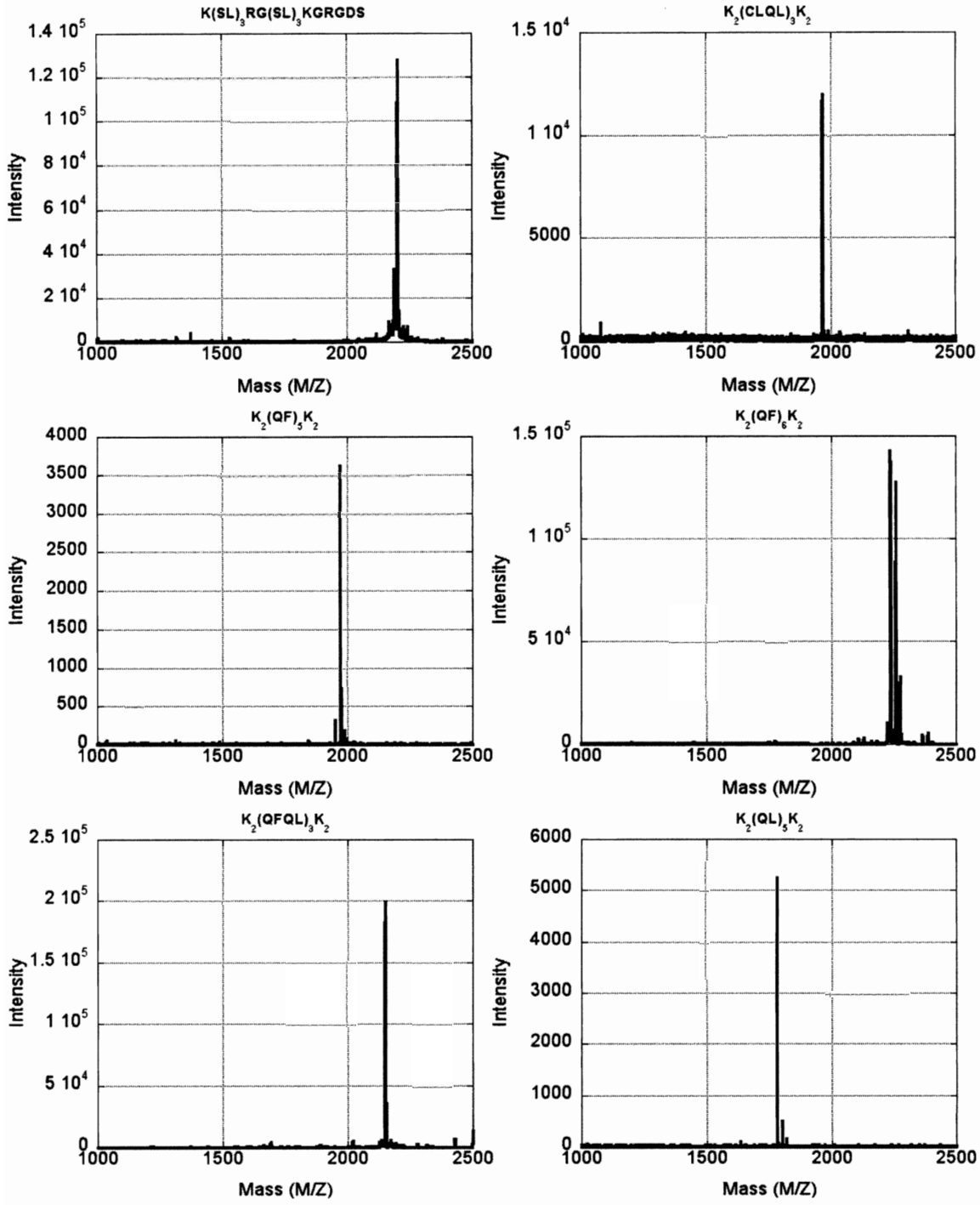

$K(SL)_3RG(SL)_3KGRGDS$	Expected Mass: 2202.5	Observed Mass: 2202.6
$K_2(CLQL)_3K_2$	Expected Mass: 1943.1	Observed Mass: 1966.4
$K_2(QF)_5K_2$	Expected Mass: 1948.3	Observed Mass: 1948.3
$K_2(QF)_6K_2$	Expected Mass: 2222.2	Observed Mass: 2221.2
$K_2(QFQL)_3K_2$	Expected Mass: 2121.5	Observed Mass: 2126.0
$K_2(QL)_5K_2$	Expected Mass: 1777.1	Observed Mass: 1777.4

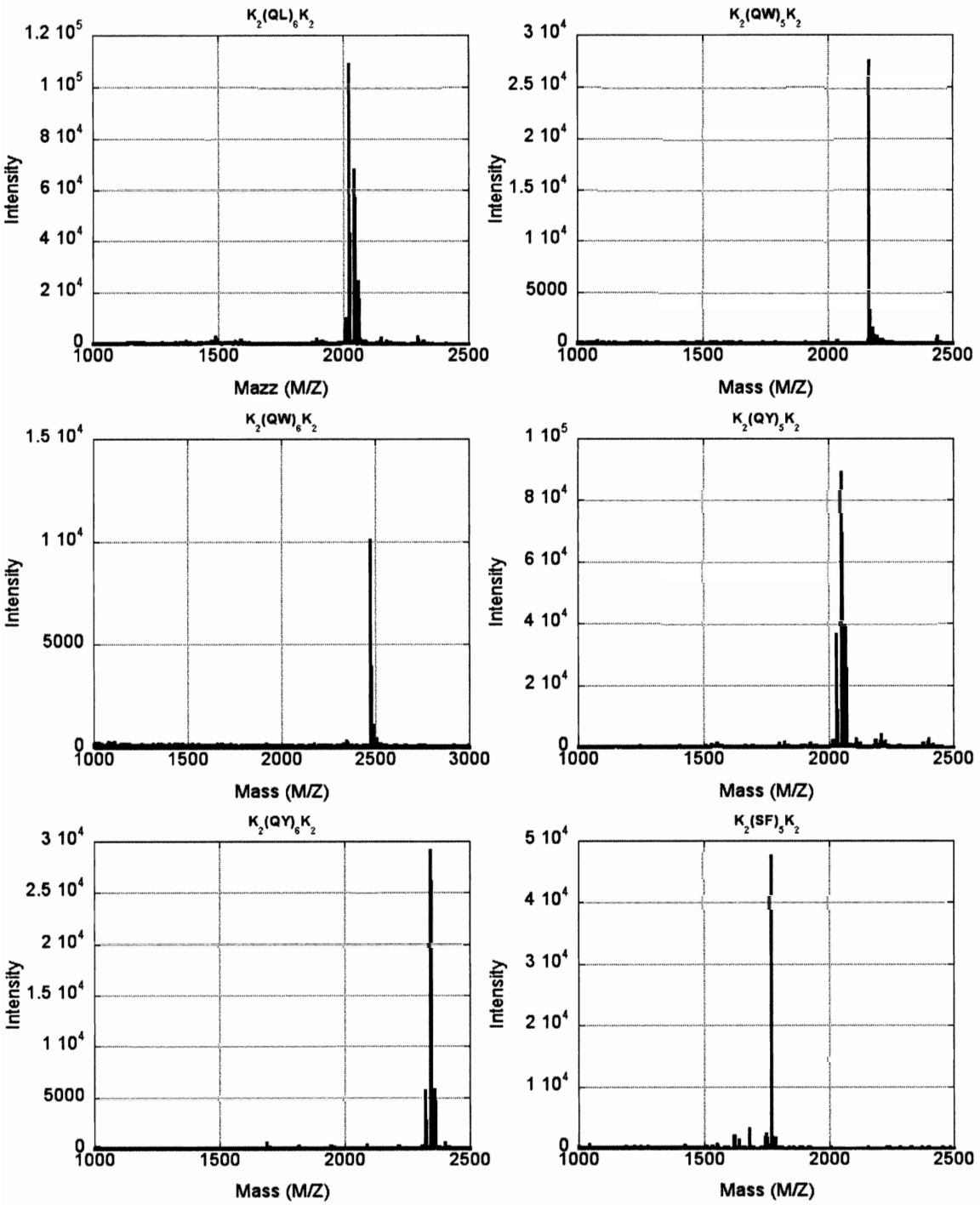

$K_2(QL)_6K_2$	Expected Mass: 2019.5	Observed Mass: 2019.8
$K_2(QW)_5K_2$	Expected Mass: 2143.5	Observed Mass: 2143.7
$K_2(QW)_6K_2$	Expected Mass: 2457.8	Observed Mass: 2458.7
$K_2(QY)_5K_2$	Expected Mass: 2028.3	Observed Mass: 2029.4
$K_2(QY)_6K_2$	Expected Mass: 2319.6	Observed Mass: 2343.5
$K_2(SF)_5K_2$	Expected Mass:1743.0	Observed Mass: 1765.5

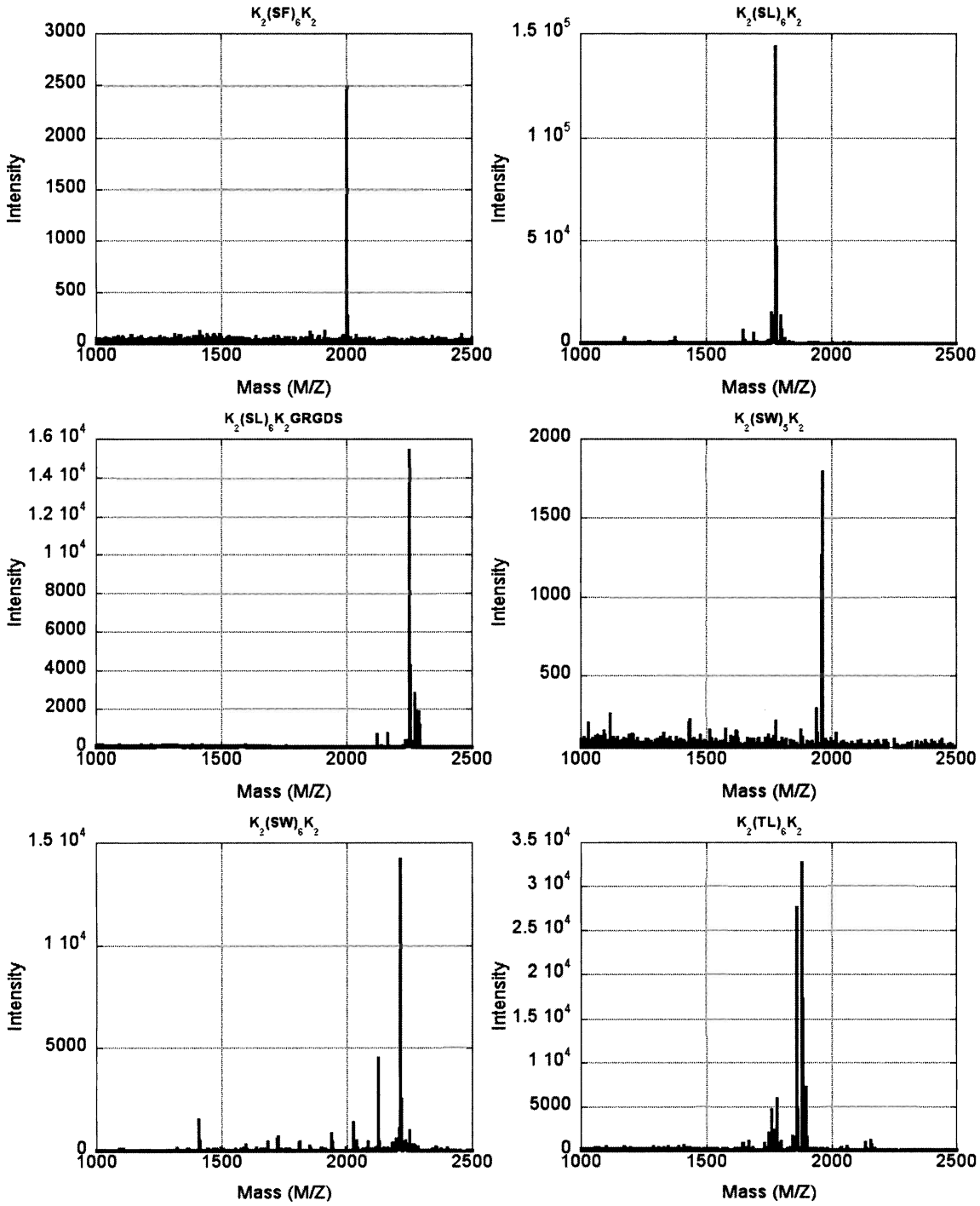

$K_2(SF)_6K_2$	Expected Mass: 1977.3	Observed Mass: 2000.2
$K_2(SL)_6K_2$	Expected Mass: 1773.2	Observed Mass: 1775.0
$K_2(SL)_6K_2GRGDS$	Expected Mass: 2245.6	Observed Mass: 2249.5
$K_2(SW)_5K_2$	Expected Mass: 1938.2	Observed Mass: 1961.3
$K_2(SW)_6K_2$	Expected Mass: 2211.5	Observed Mass: 2212.1
$K_2(TL)_6K_2$	Expected Mass:1857.3	Observed Mass: 1857.5

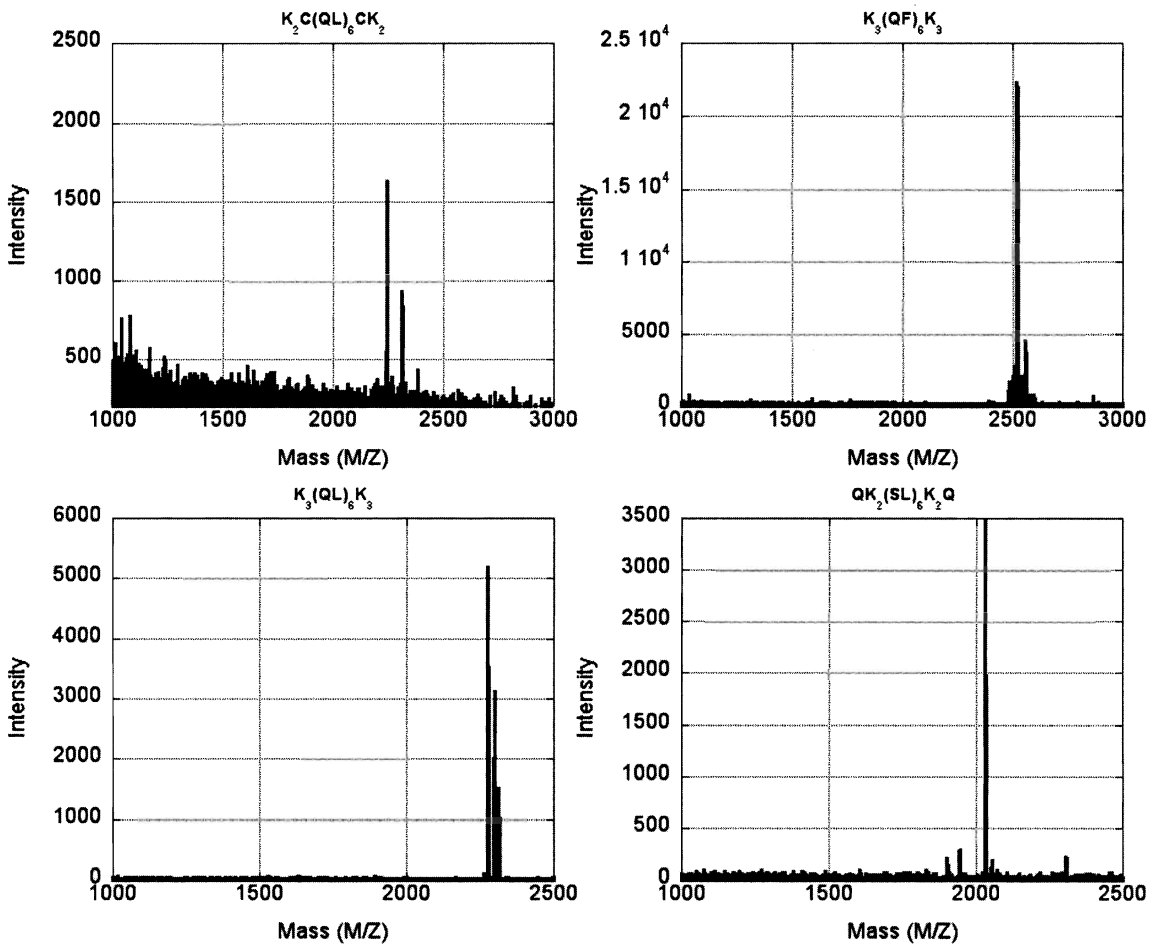

$K_2C(QL)6CK_2$	Expected Mass: 2224.3	Observed Mass: 2243.2
$K_3(QF)_6K_3$	Expected Mass: 2478.4	Observed Mass: 2519.4
$K_3(QL)_6K_3$	Expected Mass: 2275.8	Observed Mass: 2298.3
$QK_2(SL)_6K_2Q$	Expected Mass: 2029.4	Observed Mass: 2030.9